9-26-2016 12:00 AM

Numerical and Experimental Study of the Trichel Pulses in Needle-plane Geometry

x

Abstract

One of the unique aspects of the negative corona discharges in the air is the regular train of pulses that form the discharge current, called Trichel pulses. These pulses are the result of the combination of several phenomena such as the avalanche ionization of the neutral molecules by the impact of the energized electrons, formation of the cloud of positive ions close to the cathode, and formation of the cloud of negative ions at a farther distance from the corona electrode compared to their positive counterparts. In this thesis, the results of a detailed numerical investigation of the formation of Trichel pulses in a needle-plane negative corona discharge, as well as a simulation of the transition of the discharge from Trichel pulse regime to the glow discharge regime, is presented. All presented numerical models in this thesis were three-species models including the motion, generation, and dissipation of three charged species: electrons, positive ions, and negative ions. Also, all models were built using COMSOL multiphysics.

Photoionization as the main mechanism for sustaining the positive corona discharge was included in the numerical analysis for both the positive and negative corona discharges using the three exponential approximation.

A parametric study of the impact of different model coefficients on the characteristic of the Trichel pulses including the repetition frequency, average DC current and pulse rise time was investigated. The studied parameters include coefficients of the two ionization, and attachment reactions, the mobilities of the three charged species considered, electrons, positive ions, and negative ions, and the coefficient of the secondary electrons emitted from the needle. It was shown that two reactions, the recombination of positive and negative ions, and the recombination of electrons and positive ions play a minor role in the calculated characteristics of the Trichel pulses.

Finally, an experimental study of the characteristics of the Trichel pulses in air at room temperature, pressure, and relative humidity has been conducted. The impact of different parameters: the needle voltage, needle-plane distance and the radius of curvature of the needle's tip on the frequency, DC current, and the temporal characteristics of the pulses

(rise time, fall time, and the pulse width) was studied. Four different needles with radii of curvature ranging from 19 to 55 microns were used. Applied voltage on the needle was varied from the onset voltage (-4 kV to -6 kV) to -10 kV. It was observed that the temporal characteristics of the pulses such as rise time, was not a function of needle tip radius of curvature, voltage level, or needle-plane distance. The experimental data were compared with the results of a numerical simulation. The experimental findings were in a good agreement with the results of the numerical model.

Keywords

Corona discharge, Trichel pulse, Photoionization, Non-thermal plasma, Drift-diffusion equation, Poisson's equation

Co-Authorship Statement

This thesis has been written by Peyman Dordizadeh under the supervision of Prof. Kazimierz Adamiak and Prof. G.S. Peter Castle. Parts of the materials presented in this thesis have been published in several peer-reviewed journals and refereed conference proceedings as listed below. The research in each publication has been conducted by the principal author and guided/supported by or in collaboration with the underlined authors, who are the research supervisors or members of the advisory committee.

The material in Chapter 3 has been published as:

Peyman Dordizadeh, Kazimierz Adamiak, and GS Peter Castle "Numerical investigation of the formation of Trichel pulses in a needle-plane geometry" Journal of Physics D: Applied Physics 48.41 (2015): 415203

The material in Chapter 4 has been accepted for publishing in the Plasma Sources Science and Technology, Institute of Physics. The title of the accepted paper is: "Study of the impact of photoionization on negative and positive needle-plane corona discharge in atmospheric air". The authors are: Peyman Dordizadeh, Kazimierz Adamiak, and GS Peter Castle

The material in Chapter 5 has been accepted for publishing in the Journal of Electrostatics, Elsevier. The title of the accepted paper is: "Parametric study of the characteristics of Trichel pulses in the needle-plane negative corona discharge in atmospheric air". The authors are: Peyman Dordizadeh, Kazimierz Adamiak, and GS Peter Castle

The material in Chapter 6 will be submitted to the Electrostatics 2017 conference.

Dedication and Acknowledgments

I wish to dedicate this thesis to my brilliant and beautiful wife, Atefeh, who has supported and loved me endlessly since the first day we met. Thank you, Atefeh, for your love, wisdom, and support.

I would like to express my deepest gratitude to my supervisors, Dr. Adamiak and Dr. Castle. Thank you, for your consistent help, support, and valuable comments during the course of my Ph.D. studies. I will always remember you for your immense knowledge, kindness, and patience.

It is hard for me to imagine myself here without the unconditional love, support, and help of my parents. My hard-working dad and ever faithful mom, you were always the ones who I looked up to. Thank you.

Table of Contents

List of Tables

List of Figures

Nomenclature

r	r-coordinate
z	z-coordinate
n_e	electron number density $(1/m^3)$
n_p	positive ion number density $(1/m^3)$
n_n	negative ion number density $(1/m^3)$
μ_e	electron mobility (m^2/Vs)
μ_p	positive ion mobility (m^2/Vs)
μ_n	negative ion mobility (m^2/Vs)
D_e	electron diffusion coefficient (m^2/s)
D_p	positive ion diffusion coefficient (m^2/s)
D_n	negative ion diffusion coefficient (m^2/s)
S_e	electron source term $(1/m^3 s)$
S_p	positive ion source term $(1/m^3 s)$
S_n	negative ion source term $(1/m^3 s)$
V	electric voltage (V)
ε_0	vacuum permittivity (F/m)
e	electron charge (C)
$\vec{E}$	electric field (V/m)

α ionization reaction coefficient $(1/m)$

η attachment reaction coefficient $(1/m)$

k_{ep} recombination of electrons with positive ions reaction coefficient (m^3/s)

k_{np} recombination of positive and negative ions reaction coefficient (m^3/s)

γ coefficient of the secondary emission of the electrons

Γ_e flux of secondary electrons on the needle surface $(1/m^2 s)$

$S_{ph}(\vec{r})$ rate of photoionization at the point of observation $(1/m^3 s)$

R distance between source and observation points (m)

χ_{max} maximum of the absorption coefficients of ionization radiation by oxygen in the wavelength domain 98-102.5 nm

χ_{min} minimum of the absorption coefficients of ionization radiation by oxygen in the wavelength domain 98-102.5 nm

p_{O_2} partial pressure of molecular oxygen in atmospheric pressure air (Torr)

p_q quenching pressure (Torr)

$S_i(\vec{r'})$ rate of production of new electrons due to the impact ionization $(1/m^3 s)$

m_e electrons mass (kg)

v magnitude of the velocity (m/s)

θ angle between the velocity and the field direction (rad)

n_ε electron energy density (V/m^3)

Γ_ε electron energy flux $(V/m^2 s)$

$\bar{\varepsilon}$	mean electron energy (V)
μ_ε	energy mobility coefficient (m^2/Vs)
D_ε	energy diffusion coefficient (m^2/s)
k_k	rate coefficient of the kth reaction (m^3/s)
$\sigma_k(\varepsilon)$	cross section of the kth reaction (m^2)

<div style="text-align:center">

Chapter 1

</div>

1 « Introduction »

A comprehensive introduction to the nature and the mechanism of the Corona Discharge (CD), its different types, and its applications are presented in this Chapter.

1.1 What is corona discharge?

Corona discharge is a stable electrical discharge between two (or more) electrodes with substantially different radii of curvatures: one electrode should have a very small radius of curvature and the other one should have a much larger radius of curvature. The electrode with the sharper tip (usually a needle or a wire) is connected to a positive or negative high voltage source and the other electrode (usually a plane or cylinder) is connected to the ground potential. Based on the electrode geometries, different configurations of corona discharge exist. Needle-plane (or point to plane) [1], wire-cylinder [2], blade-plate [3], and cylinder-wire-plane [4, 5] are the most common ones. Generally, the configurations which consist of wire and cylinder are mostly used in the applications involving treatment of a gas. Schematic of these configurations are shown in Figure 1-1. Multi-electrode configurations are also used in the industry, e.g., a periodic set of needles or wires could be placed near the ground plane in the applications which involve passing of air flow through the corona discharge volume. It should be noted that the range of the applied voltage in the corona discharge must be higher than the corona onset level (which depends on the sharpness of the tip of the corona electrode and air gap length) and lower than the breakdown voltage. The range of the voltage and different regimes of positive and negative corona discharge will be discussed in more detail in the next parts of the Chapter.

The corona discharge phenomenon is a result of the collision of accelerated electrons with neutral gas molecules and hence triggering the avalanche ionization in the area with the strong electric field (near the corona electrode). The electrons which are in a lower field region farther from the corona electrode don't have enough energy to ionize molecules, will attach to the neutral molecules. In other words, the gap between the electrodes can be divided into two regions: ionization region, which the electrons trigger the ionization of
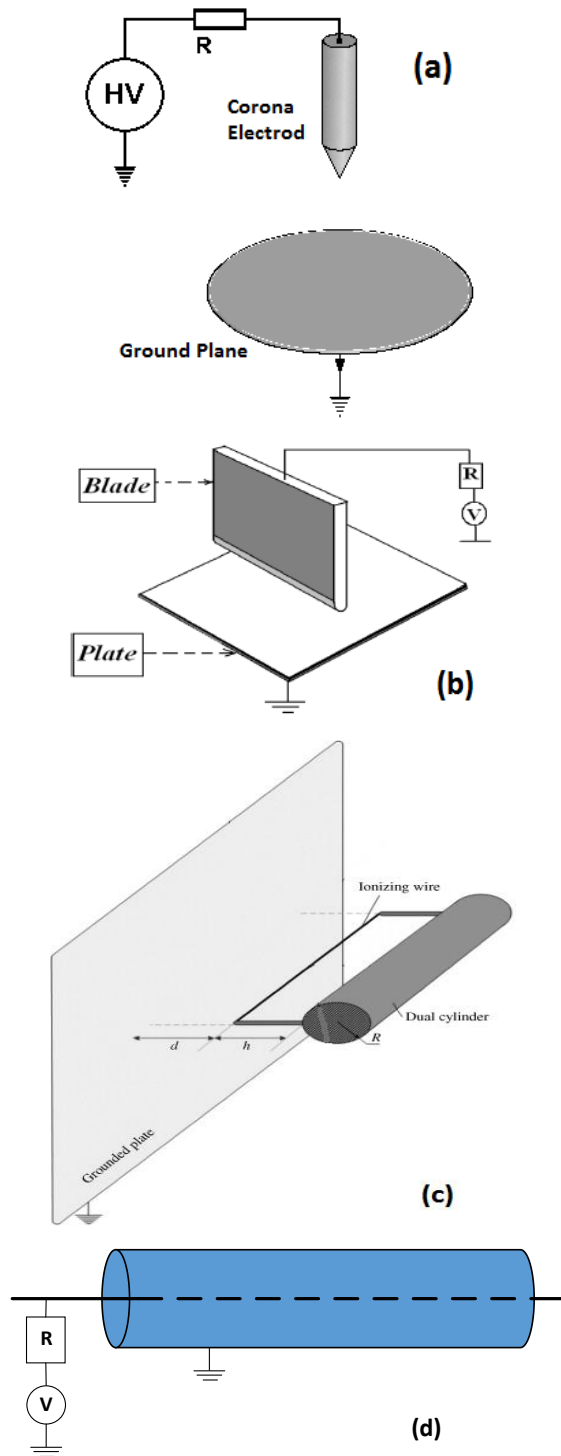
Figure 1-1: Different geometries of corona discharge, (a) needle-plane, (b) blade-plate [3], (c) cylinder-wire-plate [4, 5], and (d) wire-cylinder.

neutral molecules and new electron-positive ion pairs are created; and drift region in which the electrons have lower energy and may attach to the neutral molecules and form negative ions.

1.2 Positive corona discharge

If the corona electrode (the electrode with the sharper tip) is connected to a positive DC voltage, the discharge is called positive corona discharge. The different regimes of the positive discharge in the needle-plane geometry as the voltage level is increased are shown in Figure 1-2. The regimes, as shown from left to right, are burst pulse corona, glow corona, streamer corona, and spark. The glow corona regime, which is a pulseless regime, is usually what referred to as "positive corona discharge".
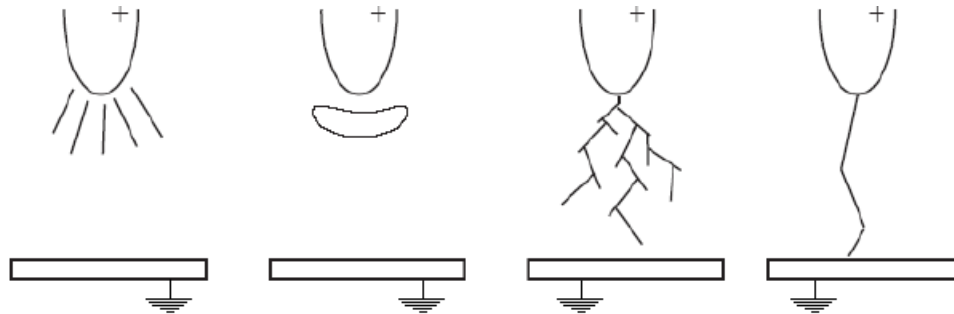
Figure 1-2: Different regimes of positive discharge in needle-plane geometry as the voltage on the needle is increased. From left to right: burst pulse corona, glow corona, streamer corona, and spark [6].

1.2.1 The mechanism

As mentioned earlier, the gap between the electrodes in the corona discharge can be divided into two regions: the ionization region and the drift region. Ionization region is a narrow region (typically less than 100 µm) close to the tip of the needle with the strongest electric field and the drift region is the region which is farther away from the tip of the needle and has a much lower electric field.

In the case of the positive corona discharge, the electrons and the negative ions in the air gap are quickly absorbed by the needle. At the same time, the positive ions drift away from the needle and ultimately get deposited on the ground plane. In addition to the electrons

and charged ions, there are some excited molecules and atoms present in the air gap, too. In the process of the return of some of the excited species to their ground state, photons are emitted which trigger the photoionization process. In simple words, ionization of the neutral molecules as a result of the impact of photons is called photoionization. It is generally accepted in the literature that the photoionization in the air is the result of the absorption by oxygen molecules of photons emitted from the return of the excited nitrogen molecules to their ground states. This is the key mechanism for sustaining the positive corona discharge. As the energized electrons collide with different molecules and generate positive ions as well as excited molecules, the photons are emitted from the return of excited species to their ground states. These photons are able to travel some distance and trigger the photoionization process at a farther location. The photoionization process, unlike its impact ionization counterpart (the impact of neutral molecules with the energized electrons), is a non-local phenomenon. Electrons produced by the photoionization, on their way towards the needle, trigger the impact ionization and excitation of different molecules and, hence, the discharge is sustained. The details of this topic are discussed in chapter 4.

1.3   Negative corona discharge

If the corona electrode is connected to a negative DC voltage, the discharge is called negative corona discharge. The different regimes of the negative discharge in the needle-plane geometry, as the voltage level is increased, are shown in Figure 1-3. The regimes, as shown from left to right, are: Trichel pulse corona, pulseless corona (negative glow corona), and spark. The discharge current in the Trichel pulse regime appears in the form a train of regular pulses called Trichel pulses named after G. W. Trichel [7].
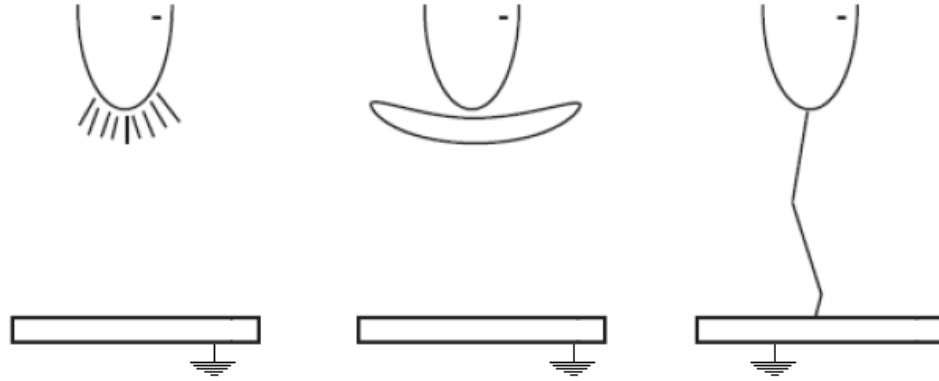
Figure 1-3: Different regimes of negative discharge in needle-plane geometry as the voltage on the needle is increased. From left to right: Trichel pulse corona, pulseless corona (negative glow corona), and spark [6].

Due to the fast transition from the Trichel pulse regime to the spark regime at atmospheric pressure, in practice, it is difficult to realize a steady state negative glow corona. In fact, the stable negative glow corona is classically known to exist only in low pressure sealed gas tubes. However, this regime is achievable at atmospheric pressure by introducing a gas flow in the gap which quenches the thermal instabilities by the convective removal of energy dissipated in the discharge. Changing the shape of the ground plane to that of a crater right below the needle tip could be used to stabilize the glow regime as well [8]. The details of this topic are discussed in Chapter 3.

1.3.1   The mechanism of the Trichel pulse

Trichel pulses, which are the regular train of current pulses observed in the negative corona discharge, is the result of a series of repetitive processes in the air gap between the corona and the ground electrode.

As mentioned earlier, there are two distinct regions in the corona discharge: the region close to the tip, the ionization region, and the region farther from the tip, the drift region. In the ionization region, due to the collision of highly accelerated electrons with neutral molecules, the avalanche ionization occurs. In most cases, this region is less than a fraction of millimeter around the corona electrode. On the other hand, the drift region is the region mostly filled with the negative ions. In the ionization region, the ionization reaction predominates over the attachment reaction. The boundary between the ionization region

and the drift region is generally defined where the reduced electric field E/N=120 Td (E is the magnitude of the electric field and the N is the density of the neutral molecules, 1 Td= 10^{-21} Vm^2). Beyond the ionization region, the electric field decreases and electrons do not have sufficient energy to ionize the neutral molecules. Therefore, the attachment reaction becomes predominant provided of the gas contains sufficient electronegative molecules and the number of electrons decreases in the drift region. Since in the drift region, there might be some electrons left with sufficient energy for the ionization of gas molecules, some authors assume another layer, called the plasma layer, which starts from the ionization boundary and extends a few millimeters into the drift region. Davidson [9] has defined this region as the corona plasma region, in which some corona-enhanced chemical reactions are possible and its boundary is given by the radius at which the reduced electric field E/N=80 Td. At this value, the mean kinetic energy of electrons is 1.85 eV and some electrons are energetic enough to cause electron-impact ionization. Figure 1-4 shows the schematic of the ionization and drift regions in a point to plane negative corona discharge.
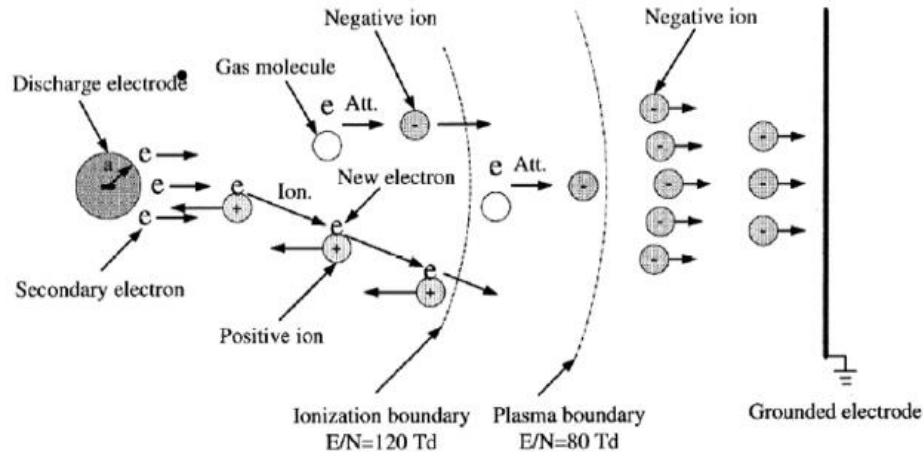
Figure 1-4: Schematic of the ionization and drift regions in negative corona discharge [10].

As a result of the avalanche ionization, a cloud of positive ions is created close to the corona electrode in the ionization region. On the other hand, the attachment reactions create a cloud of negative ions just outside the ionization layer. When these clouds become dense enough to perturb the Laplacian field between the two electrodes, the electric field in the

area between the two clouds is decreased. Moreover, the electric field between the positive ions and the corona electrode is increased (Figure 1-5).
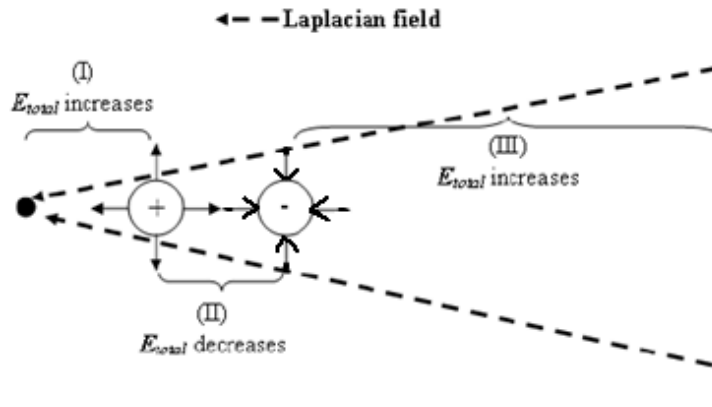
Figure 1-5: Schematic of the perturbation of Laplacian field when the clouds of positive and negative ions become dense enough [10].

The increased electric field in the ionization layer increases the avalanche ionization in this area which causes a very fast build-up of the corona current. As soon as the cloud of negative ions becomes dense enough, the ionization layer and, hence, the avalanche ionization is limited to the region (I), as shown in Figure 1-5. Since the corona electrode has negative polarity, the positive ions, on the other hand, move towards the corona electrode. When the peak concentration point of the positive ions reaches the corona electrode, the injection of the secondary electrons from the needle will be at its maximum. Hence, the corona current will be at its maximum. At this moment, the avalanche ionization has not yet stopped. For a short time after the maximum of the pulse, avalanche ionization still occurs. Therefore, the total number of electrons in the space still increases after the pulse peak. However, since the positive ions are being deposited on the corona electrode and the deposition rate is larger than the generation rate, the number of positive ions decreases during this time.

Finally, negative ions, which are being accumulated throughout the process at the edge of the ionization region, become dense enough to diminish the electric field in the whole ionization region. Hence, the ionization process ceases and the current pulse decays. After

this step, the attachment reaction is the only process present which increases the total number of negative ions in the air gap.

It is generally accepted that the secondary emission of the electrons from the corona electrode is the main mechanism for sustaining the negative corona discharge. These electrons are ejected from the surface of the corona electrode due to the bombardment of the electrode surface by the positive ions. As the negative ions move towards the ground plane, the electric field in the ionization regions starts increasing again. On the other hand, the secondary emission of electrons from the needle provides seed electrons for the next pulse. Hence, the discharge is sustained.

1.4   Applications of the corona discharge

The corona discharge has many applications in the industry, medicine, and the everyday life. Some of these applications were discovered and commercialized more than a century ago. In 1907, the first major successful commercial application of electrostatic precipitator was accomplished [11]. Since then, numerous researchers devoted their attention to the particle charging and electrostatic precipitators using different geometries [12, 13].

Ozone generation is also an important application of the corona discharge. The oxidative properties of this gas have been used for water treatment and odor control [14, 15]. Ozone is generally produced by passing a stream of dry air or oxygen through a corona discharge volume, where oxygen molecules (O_2) in the stream are converted to ozone (O_3). Putting a dielectric film on the ground electrode converts corona discharge to Dielectric Barrier Discharge (DBD) and increases the efficiency of the process.

Electrophotography and electrographic printing make use of small corona devices as surface chargers. The photoconductive drum of a copier/printer must be given a uniform charge prior to exposure to the light image. Exposure to light discharges the surface, leaving patterns of charge on the drum which can attract oppositely charged toner particles. The toner is then transferred to the paper with the influence of a charger on the back side of the paper; the charger produces an electric field that enhances transfer. Corona chargers

also remove the residual charges on the photoconductive drum, so that it may be cleaned prior to subsequent exposures [6].

Flue gas treatment and air pollution control are other known applications of corona discharges. Numerical and experimental studies of the removal of NOx and SOx from the flue gas have been conducted [16, 17].

The idea of smoke triggered corona discharge for an ionic smoke sensor working without a radioactive ionization source was published by Mokhtari et al. [18]. It is based on the decreasing of the corona discharge onset voltage by a factor of 5 in the presence of smoke particles. A novel method for designing a respiratory monitoring sensor based on the Trichel pulses has been suggested by Deng et al. [19]. This method is based on using a simple field ionization sensor, which consists of a needle electrode and a grounded plane. It is shown that different respiratory patterns such as normal breathing, fast breathing, and apnea could be monitored in real-time by detecting the changes in the frequency of the Trichel pulses.

Medical applications such as dental cavity treatment with the help of plasma produced in corona discharge [20] and biofilm decontamination on the teeth surface by exposing the teeth to a positive streamer or negative Trichel pulses [21] have been investigated by the researchers.

Electrospraying [22, 23], semiconductor technology [24], air flow control [25], decoloration of chemical compounds [26], food and water decontamination [27] are other applications of the corona discharge technology.

The importance of the corona discharge is not only due to the useful applications it has; it may have unwanted effects as well. It is generally undesirable in electric power transmission lines, where it causes power loss, audible noise, and electromagnetic interference. Corona discharge is also harmful if it happens inside the electrical components, such as transformers, capacitors, electric motors and generators where it progressively damages the insulating materials [10].

1.5 Thesis objectives

The objective of this thesis to conduct a comprehensive numerical and experimental study of the formation of Trichel pulses in the negative DC corona discharge in atmospheric air. Throughout the thesis, the studied geometry consists of a needle (corona electrode) which is placed perpendicularly above a ground plane.

In the numerical analysis, three charged species: electrons, positive ions, and negative ions have been included. Therefore, the inception voltage of the corona discharge will not be calculated using Peek's law and will be left to the coefficients of involved reactions.

The effect of several parameters: the needle voltage, needle-plane distance, radius of the tip of the needle, existence of some reactions and the existence of the photoionization phenomenon on the characteristics of the pulses have been studied. The frequency of the pulses, DC current and in some cases the temporal characteristics of the pulses (rise time, fall time, and pulse width) are the main parameters of interest.

1.6 Thesis outline

The thesis is divided into 7 chapters. The outline of each chapter is summarized below:

Chapter 2: A review of the relevant publications in the area of positive and negative corona discharge, and Trichel pulses is presented. In addition, published papers in the area of the photoionization phenomenon, to the extent of the conducted studies regarding its impact on the corona discharges, have been reviewed as well.

Chapter 3: A numerical investigation of the formation of the Trichel pulses is presented. A needle with the tip radius of 35 µm and a needle-plane spacing of 6 mm over the voltage range of -3.5 kV to -12 kV is studied. This Chapter also focuses on the transition of the Trichel pulse regime to the glow discharge.

Chapter 4: This Chapter describes the incorporation of the photoionization phenomenon in the model, which was presented in Chapter 3. For this purpose, a three-term exponential approximation was used for adding three more equations to the system of equations established in Chapter 3.

Chapter 5: During the studies conducted in Chapter 3, it was found that the numerical model was more sensitive to some coefficients than others. The goal of this chapter is to describe the effect of variation of different model coefficients on the characteristics of the pulses.

Chapter 6: The results of an experimental study of the characteristics of Trichel pulses are presented. In this study, four different needles with radii of curvatures ranging from 18 to 57 microns were used and applied voltage on the needle was varied from the onset voltage (-4 kV to -6 kV) to -10 kV.

Chapter 7: A brief introduction to the electron energy equation and a summary of the unsuccessful attempts for including this equation in the corona discharge model is given.

Chapter 8: A general summary of the thesis and some recommendations for future studies are given in this Chapter.

Chapter 2

2 « Literature review »

This chapter presents a comprehensive review of the papers published in the literature in the area of the theoretical and the experimental investigations of corona discharges and Trichel pulses, especially the ones focused on the needle-plane geometry. Due to the vital role the photoionization phenomenon plays in sustaining the positive corona discharge, papers in the area of the photoionization are also reviewed.

2.1 Early discovery and research

Trichel pulses in a needle-plane (also known as point-plane) configuration were first reported by G. W. Trichel in 1938 [7]. The pulses (Figure 2-1) were first discovered as a train of regular current pulses in a needle-plane circuit with the needle connected to a negative DC voltage. Trichel conducted the experiments by placing the needle 3 cm away from the ground plane. He repeated the experiments with 4 different needles and hypothesized that the magnitude and the frequency of pulses have a definite relationship to the corona current, point size and gas pressure. He also predicted that the frequency is independent of spacing between the point and the plane.
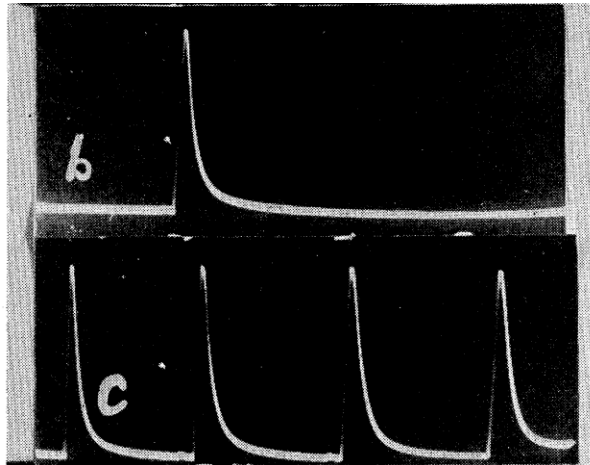
Figure 2-1: Train of regular pulses observed by G. W. Trichel [7].

This work was later complemented by Loeb et al. [28], where more details were given about the role of the cloud of negative ions. The fact that the accumulation of this cloud leads to the suppression of the electric field and quenching of avalanche ionization was also discovered. Some researchers were suspicious in supporting this theory. Cernak and Hosokawa [29] observed a similarity between the development and the initial decaying stage of the Trichel pulses and the breakdown pulse in a short negative point to plane discharge in nitrogen (an electropositive gas). Based on these similarities, they hypothesized that the quenching of Trichel pulses cannot be caused solely by the accumulation of negative ions. Later, they extended their studies by adding a small admixture of SF_6 which increases the attachment coefficient, keeping the ionization coefficient and the secondary emission of the electrons constant [30].

Loeb and his co-workers believed that the Trichel pulses can only exist in electronegative gasses, such as oxygen and air, which was later supported by the findings of Weissler [31], who studied the existence of Trichel pulses in different gasses. He reported that the Trichel pulses are not observed in pure hydrogen and nitrogen (these are electropositive gasses), but noticed that adding a trace of oxygen to these gasses will result in the generation of Trichel pulses. This idea was challenged later by Akishev et al. [32, 33], who proved that under specific circumstances the pulses can be observed in nitrogen, too. Loeb [34] also believed that the frequency of the Trichel pulses near corona onset voltage was equivalent with the time of the transit of the negative ions across the gap. Gardiner and Craggs [35] conducted some experiments studying the negative ions formed in the process of formation of Trichel pulses in lowered pressure air (10-30 Torr) and were able to confirm Loeb's theory.

In 1951, Bandel [36] conducted a survey study on the point to plane corona in air for a range of pressures and point sizes for both the positive and negative polarities. He noticed in the case of negative polarity, as the voltage level is increased, under some conditions, a transition from Trichel pulse regime to "pulseless Townsend-type discharge" happens. Although the transition wasn't investigated deeper, he realized it was accompanied by a jump in the discharge current. More recently, Akishev et al. [8] published a report discussing the pulseless glow regime and the methods to stabilize it. They suggested

changing the shape of the anode (ground plane) to that of a crater right below the needle tip could be used to stabilize the negative glow regime at atmospheric pressure.

In 1974, Lama and Gallo reported [37] the results of a series of systematically designed experiments with the aim of finding the relation between the electrical properties of pulses (DC current, frequency and injected charge per pulse) and macroscopic properties of the discharge circuit (radius of tip, needle to plane spacing and applied voltage). Combining the experimental findings and theoretical analysis, they also formulated a theory of the existence of several clouds of negative ions in the air gap rather than having only one such cloud at a time. Despite all the success they had, they weren't able to record the real current pulses because the minimum observable pulse period in their experimental equipment was 0.25µs. Akishev et al. [8] published the idea of controlling the frequency and amplitude of Trichel pulses with the radius of the tip and DC current kept constant. The method they used involved introducing air flow and geometrical effects on the discharge elements (e.g., putting dielectric screens around the pin and restrictions in cross sections of the drift region).

In 1981, van Brunt et al. [38] studied the corona discharges for both positive and negative polarities in SF_6 which had been discovered as a great insulator. They observed Trichel-like irregular pulses in this gas for the negative discharge.

In 1985, Cross et al. [39] observed a step on the leading edge of the Trichel pulses. They reported that this step exists in the larger point radii and disappear in the smaller ones. They also noticed that the first pulse in the discharge current was significantly different from succeeding ones and in particular the leading-edge step was present for all studied points. In the same year, Morrow laid some theoretical grounds for justifying these leading-edge steps [40].

The characteristics of Trichel pulses in low-pressure gasses were also studied by other authors [35, 41-43]. It was shown in [41, 42] that the rise time of pulses in the air with pressure reduced to several Torr could increase up to 10µs.

Some researchers were interested in the effect of the air flow on the characteristics of Trichel pulses. In 1966, Nygaard et al. [44] studied the variation of the frequency of the pulses due to the blowing of a wind. Recently, Deng et al. [45] reported that by increasing the transverse airflow (perpendicular to the needle-plane symmetry line), the frequency becomes lower and the peak of the pulse gradually rises to higher values. They have also studied the effect of humidity on the Trichel pulses and found that the magnitude of Trichel pulses grows gradually with increasing humidity and the frequency of pulses increases with humidity [46].

2.2   Numerical models

Although the attempts to develop a mathematical model of corona discharges started from the mid-1960s [47], the work presented by Morrow [40, 48] is believed to be the first well-documented report on this topic. He used a combination of Finite Difference (FD) and Flux Corrected Transport (FCT) methods for solving three continuity equations for three charged species and Poisson's equation, assuming a one-dimensional model of the problem. Despite the detailed explanation of the different stages of the pulse formation, he was only able to reproduce the first pulse by following the discharge to 213ns. Chen and Davidson [9] have proposed a 1D stationary model for modeling the plasma region of both positive and negative corona discharges in a wire-cylinder geometry. They used FD for their 3 species (electrons, positive and negative ions) model and assumed a constant electric field (Peek's formula) on the wire boundary. Later in 1997, Morrow applied the same technique for investigating the positive glow corona [49] and explained why onset streamers always precede the formation of the glow in the positive corona discharge. Napartovich et al. [50] suggested a quasi-one-dimensional model assuming a constant distribution for all quantities (densities of charged species and electric field) in every cross section of the discharge channel perpendicular to the axis of symmetry.

Akishev et al. [51] have conducted a thorough study of the formation of Trichel pulses in the needle-plane configuration by solving three transport equations and one Poisson's equation in a 2D axisymmetric geometry. They predicted the distributions of three charged

species in the air gap and also the distribution of current density on the cathode surface at different instants of formation of a Trichel pulse.

Although the Finite Element Method (FEM) has proved to be a very effective tool for modeling the corona discharge phenomenon, it requires some stabilizing strategies for achieving a convergent solution. Various authors have tried different methods by combining FEM with other techniques. Zhang et al. [52] developed a model with a combination of the Boundary Element Method (BEM) and FEM for solving the electric field and Method of Characteristics (MOC) for solving the distribution of charged species. Khaddour et al. [3] used a combination of MOC and FEM to analyze the corona discharge in a blade-plate geometry. Sattari et al. [53, 54] used a combination of the FEM and FCT to solve a 2D axisymmetric single-species model for a negative corona discharge with pulse and step voltage on the corona electrode. They were able to remove the artificial oscillations in the calculated results, which occur in classical FEM approach for treating the charge transport equations, using a three-step procedure. Later, they applied the same method for simulating negative DC corona discharge for a three-species model and explained the impact of different parameters of the model on the characteristics of Trichel pulses (frequency and DC current) [55]. The parameters of interest were the external resistance of the circuit, secondary electron emission and the mobilities of positive and negative ions.

Sattari et al. reported in [55] that the secondary emission coefficient of electrons doesn't significantly affect the Trichel pulse characteristics, which contradicts the findings of Tran et al. [56] who reported that the frequency of Trichel pulses increases if the secondary emission coefficient is increased.

Single-species models are not able to reproduce Trichel pulses and were mostly used for positive corona [53, 57]. On the other hand, multi-species models are more complicated and used widely for predicting the dynamic behavior of positive and negative corona discharge [43, 45, 56].

Although most of the numerical models for predicting the behavior of Trichel pulses are one- or quasi-one-dimensional [9, 48, 50, 58, 59], some authors used a two-dimensional

axisymmetric geometry for studying these pulses in needle-plane geometry [45, 55, 56]. This has the benefit of giving a quasi-three-dimensional picture of the occurring phenomena while using a reasonable amount of computational resource.

Characteristics of Trichel pulses in oxygen with the reduced pressure of 50 Torr including 24 reactions and 10 ionic and excited species in a 2D axisymmetric model have been studied by Duran-Olivencia et al. [43]. They found out that the production of the neutral and excited oxygen atoms is only limited to the duration of each pulse and they are not produced during the inter-pulse interval. In contrast, ozone is generated continuously and its temporal growth does not reflect the formation of pulses.

Tran et al. [56] have studied the differences and the similarities between negative DC corona discharge and negative Dielectric Barrier Discharge (DBD) in a 2D axisymmetric geometry. They explained different stages of Trichel pulse formation for a 3.3mm air gap in a needle-plane geometry. They showed that during the negative half-cycle of DBD, only one discharge current pulse is produced instead of a pulse sequence as for the corona discharge case. They also conducted a similar numerical study for a very short gap of 1 mm [60] and concluded that the frequency of the pulses increases with the secondary emission coefficient.

2.3   Photoionization

Penney et al. [61] conducted a series of experiments for measuring the photoionization produced by the point-plane corona discharges in the air over a pressure range of 0.1 to 18 Torr. They expressed their results in terms of the pressure multiplied by the distance from the discharge point (Rp), in the range of 1<Rp<550 cmTorr. For many later authors, this work became the reference for the comparison of the suggested numerical methods with the experiments [62-65]. Based on the results published in [61], a decade later, Zheleznyak et al. [66] proposed a nonlinear numerical model consisting of a non-local integral for photoionization in air. Despite the fact that this model was very time-consuming to run, it has been later recognized in the literature as the classical integral model for photoionization in air.

Naidis [62] has studied the photoionization phenomenon in the dry and moist air. Based on the data published by Zheleznyak et al. [66], he showed that the absorption of radiating states by water molecules is necessary for modeling the photoionization in moist air. Since the model was based on solving the classical integral suggested in [66], it was very time-consuming.

Following the efforts for finding a more efficient numerical model for the photoionization phenomenon, Ségur et al. [67] have suggested using the improved Eddington approximation, originally developed by Larsen et al. [68], to model this phenomenon for obtaining a more accurate prediction of the behavior of the streamers. Later, Bourdon et al. [64] presented a comparison of the Eddington approximation, the improved Eddington approximation, and the Helmholtz equation approximation, suggested by Luque et al. [63], for the modeling of photoionization source term in non-thermal gas discharges. They discussed the importance of the accurate definition of the boundary conditions in the compared numerical models. Luque et al. [63] and Papageorgiou et al. [69] had suggested a zero Dirichlet boundary condition for the boundaries of the computational domain for the Helmholtz equation model.

Recently, Pancheshnyi [65] developed a model for a quantitative analysis of the photoionization mechanism and its rate in nitrogen-oxygen mixtures. He suggested a correction factor for generalization of the model to any arbitrary N_2-O_2 mixture over a wide range of reduced electric fields.

2.4   Summary

Despite all the numerical works published in the area of Trichel pulse, there is a lack of detailed model explaining the distributions of the charged species in the air gap in different stages of the formation of the Trichel pulse. Moreover, numerical investigation of the transition of the Trichel pulse regime to the glow discharge regime in atmospheric air is a topic which definitely needs more attention.

The photoionization phenomenon is mostly ignored in the modeling of the corona discharge. We believe it would be beneficial to have a three-species self-sustained model for positive corona discharge including the photoionization phenomenon.

Sensitivity analysis of the frequency, DC current and the temporal characteristics of the pulses to the model coefficients is another issue which definitely has room for more investigation.

Chapter 3

3 « Numerical investigation of the formation of Trichel pulses in a needle-plane geometry »

This Chapter presents a numerical investigation of the formation of the Trichel pulses in negative DC corona discharge for a needle-plane configuration in atmospheric air. The needle voltage should be higher than the corona onset voltage. A 2D axisymmetric model of the problem considering three charged species (electrons, positive ions, and negative ions) and consisting of a hyperboloid needle with a tip radius of 35 µm and needle-plane spacing of 6 mm over the voltage range of -3.5 kV to -12 kV has been studied. The needle was defined using the parametric equations of a parabola:

$$r = 2 \cdot R \cdot t \qquad \text{(3-1)}$$
$$z = R \cdot t^2 + h \qquad \text{(3-2)}$$

where r, z, R, h, and t are the r-coordinate, z-coordinate, radius of the tip of the needle, needle-plane gap, and the parameter, respectively. In this Chapter, h=6 mm, R=35 µm, and the parameter t varies in the range of zero and 29.277 which results in a 3 cm long needle. The needle, ground plane, and the computation domain is shown in Figure 3-1.
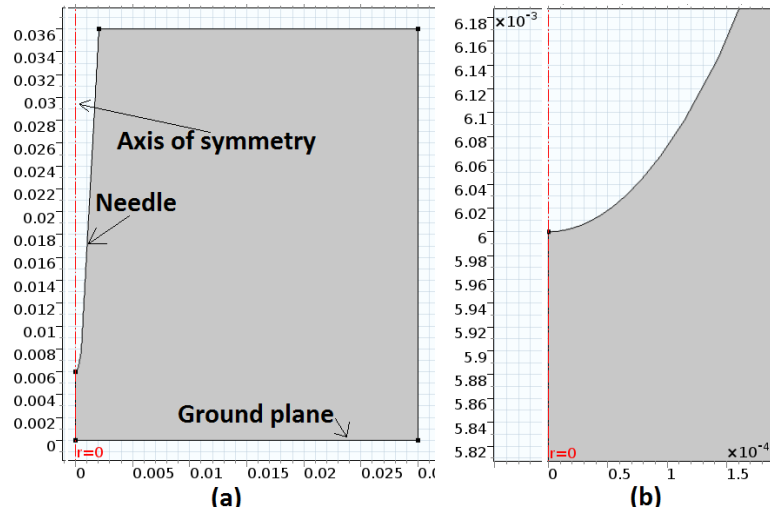
Figure 3-1: Representation of the computation domain, needle, and the ground plane: (a) overall view and (b) zoomed view of the needle tip.

The radius of the needle tip and the needle-plane distance was chosen in a way so that the results of the numerical simulations could be compared with the experimental results published before by Lama and Gallo [37]. As mentioned in the previous chapter, Lama and Gallo reported [37] the results of a series of systematically designed experiments with the aim of finding the relation between the electrical properties of pulses (DC current, frequency and injected charge per pulse) and macroscopic properties of the discharge circuit (radius of tip, needle to plane spacing and applied voltage).

The aim of this Chapter is to present a thorough investigation of the charged species' distribution in the air gap during the different stages of Trichel pulse formation as well as the time variation of peak densities and total number of the three charged species. The distribution of the current density on the ground plane is compared with the empirical Warburg formula. The transition of the discharge from the Trichel pulse regime to glow discharge will also be investigated.

In the following, first, the description of the developed numerical model is explained. In this part, the physics of the governing equations and geometry of the proposed model is presented. Then, the simulation results along with the detailed description of the formation of Trichel pulses with the aid of both temporal and spatial graphs are reported. A comparison of these results with the experiments of Lama et al. [37] is then presented and, finally, the prediction of transition of discharge from the Trichel pulse regime to glow discharge regime is discussed.

3.1   Description of the model

The model investigated in this chapter is a 2D axisymmetric needle-plane geometry for negative DC corona discharge in which the gas is air at atmospheric pressure. The needle, which is 3 cm long, has a hyperbolic tip and is placed 6 mm away and perpendicularly to the ground plane. The simulations are carried out for the radius of curvature of the needle tip equal to 35 µm. The tip radius, type of the needle and needle-plane spacing were chosen in a way so that the results could be compared with the experimental results published by Lama and Gallo [37]. Simulations were carried out for DC voltages in the range of -3.5 kV to -12 kV. It was found that the -3.5 kV was the corona onset voltage for this specific

configuration. The computational domain is a 3 cm × 3.6 cm rectangle in which the ground plane forms the bottom boundary. Figure 3-2 and Table 3-1 illustrate the boundaries and the boundary conditions for all simulated distributions. For fully understanding the descriptions given in Table 1, one needs to consider that the proposed model consists of 4 partial differential equation (Eqs. 3-1 to 3-4), with each one of them requiring specific boundary conditions.
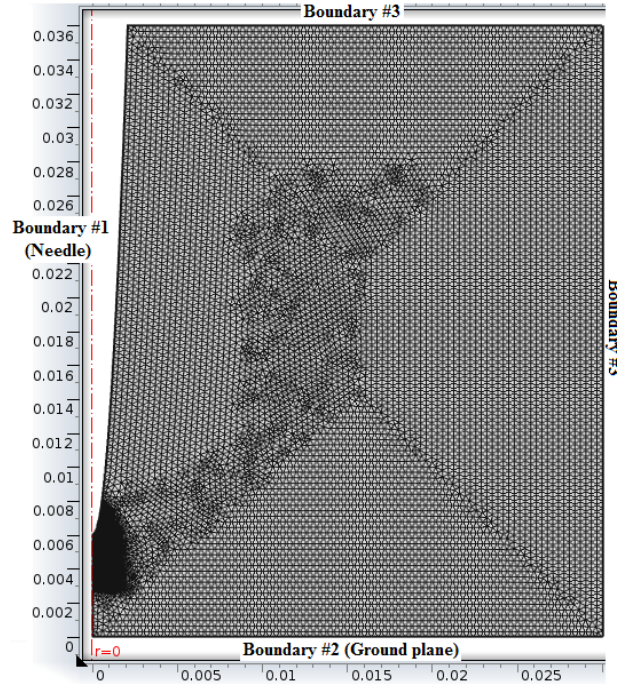
Figure 3-2: The description of the boundaries and the discretization of the investigated model. Horizontal and vertical axes are in (m).

The geometry reported in [56] has a smaller computational domain, so one might consider here using a smaller computational domain for the sake of economizing on the computation resources. In this case, it is important to note that in reality the conditions imposed on boundaries #3 ("zero charge") are artificial and for that reason, these boundaries should be as far as possible from the needle tip to minimize the impact of those boundaries on the electric field. It was numerically confirmed that the variation of the Laplacian electric field at the needle tip was less than 1% for the domains larger than 3 cm × 3.6 cm in the current model.

Table 3-1: Conditions imposed on boundaries for Eqs. 3-1 to 3-4

	Boundary #1	Boundary #2	Boundary #3
Electron's drift-diffusion, Eq. 3-3	Flux of secondary electrons (Eq. 3-14)	Outflow $-\vec{n} \cdot D_e \nabla n_e = 0$	Open boundary $\begin{cases} -\vec{n} \cdot D_e \nabla n_e = 0; & \vec{n} \cdot \left(-\mu_e \vec{E}\right) \geq 0 \\ n_e = 0; & ; \vec{n} \cdot \left(-\mu_e \vec{E}\right) < 0 \end{cases}$
Positive ion's drift-diffusion, Eq. 3-4	Outflow $-\vec{n} \cdot D_p \nabla n_p = 0$	Zero density $n_p = 0$	Open boundary $\begin{cases} -\vec{n} \cdot D_p \nabla n_p = 0; & \vec{n} \cdot \left(\mu_p \vec{E}\right) \geq 0 \\ n_p = 0; & ; \vec{n} \cdot \left(\mu_p \vec{E}\right) < 0 \end{cases}$
Negative ion's drift-diffusion, Eq. 3-5	Zero density $n_n = 0$	Outflow $-\vec{n} \cdot D_n \nabla n_n = 0$	Open boundary $\begin{cases} -\vec{n} \cdot D_n \nabla n_n = 0; & \vec{n} \cdot \left(-\mu_n \vec{E}\right) \geq 0 \\ n_n = 0; & ; \vec{n} \cdot \left(-\mu_n \vec{E}\right) < 0 \end{cases}$
Poisson's, Eq.3-6	Negative DC voltage	Ground potential	Zero charge $\vec{n} \cdot \left(\varepsilon \vec{E}\right) = 0$

3.1.1   Governing equations

With the aim of having a completer picture of the Trichel pulse phenomenon, the proposed model considers the presence of three species: electrons, positive ions, and negative ions. This is computationally more expensive compared to the simpler models, which only consider the presence of electrons and negative ions [52]. The movement, generation, and dissipation of these charged species are taken into account by three drift-diffusion equations as well as a Poisson's equation that is needed for calculating the distribution of the electric field in the air gap. Thus, the following four equations need to be solved simultaneously [56]:

$$\frac{\partial n_e}{\partial t} + \nabla \cdot \left(-\mu_e \vec{E} n_e - D_e \nabla n_e\right) = S_e \qquad (3\text{-}3)$$

$$\frac{\partial n_p}{\partial t} + \nabla \cdot \left(\mu_p \vec{E} n_p - D_p \nabla n_p\right) = S_p \qquad (3\text{-}4)$$

$$\frac{\partial n_n}{\partial t} + \nabla \cdot \left(-\mu_n \vec{E} n_n - D_n \nabla n_n\right) = S_n \qquad (3\text{-}5)$$

$$\nabla^2 V = \frac{-e\left(n_p - n_e - n_n\right)}{\varepsilon_0} \qquad (3\text{-}6)$$

where n_e, n_p, n_n, μ_e, μ_p, μ_n, D_e, D_p, D_n, S_e, S_p, S_n are the number densities$(1/m^3)$, mobilities (m^2/Vs), diffusion coefficients (m^2/s) and source terms $(1/m^3 s)$ of electrons, positive ions, and negative ions, respectively. Moreover, V, ε_0, and e represent the voltage, vacuum permittivity, and the electron charge (SI units), respectively. Finally, $\vec{E}(V/m)$ is the electric field vector. For describing the source terms of the charged species,

reactions occurring in the air gap need to be taken into account. Four main reactions: ionization, attachment of electrons to neutral molecules, recombination of electrons with positive ions and recombination of positive and negative ions, are considered:

$$e + N_2 (O_2) \rightarrow 2e + N_2^+(O_2^+) \qquad\qquad (3\text{-}7) \text{ ionization}$$

$$e + O_2 \rightarrow O_2^- \qquad\qquad (3\text{-}8) \text{ attachment}$$

$$e + N_2^+ (O_2^+) \rightarrow N_2 (O_2) \qquad\qquad (3\text{-}9) \text{ recombination of electrons}$$
with positive ions

$$O_2^- + N_2^+ + N_2 (O_2) \rightarrow N_2 + O_2 + N_2 (O_2) \qquad (3\text{-}10) \text{ recombination of positive}$$
and negative ions
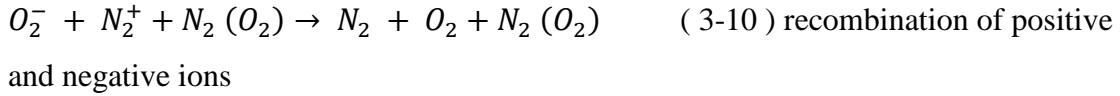
Because of the higher electronegativity of the oxygen molecule compared to the nitrogen molecule, the majority of the produced negative ions in the air are negative oxygen ions. In fact, it is accepted in the literature that the regular current pulses are not present in the discharges which occur in pure nitrogen. This is due to the vital role of the negative ions in the periodic process of diminishing the electric field in the negative discharge.

Although a full chemical kinetic model for plasma in dry air contains some hundreds of reactions and species including neutral molecules, electronically excited species and ions [50], it is proven that the included three charged species and four main reactions well describe the behavior of the discharge and the Trichel pulses [56]. Given $\alpha(1/m)$, $\eta(1/m)$, $k_{ep}(m^3/s)$ and $k_{np}(m^3/s)$ as the coefficients for the above mentioned reactions respectively, the source terms in the Eqs. 3-1 to 3-3 will be as follows:

$$S_e = \alpha n_e |\mu_e \vec{E}| - \eta n_e |\mu_e \vec{E}| - k_{ep} n_e n_p \qquad\qquad (3\text{-}11)$$

$$S_p = \alpha n_e |\mu_e \vec{E}| - k_{ep} n_e n_p \qquad\qquad (3\text{-}12)$$

$$S_n = \eta n_e |\mu_e \vec{E}| - k_{np} n_n n_p \qquad\qquad (3\text{-}13)$$

Swarm parameters (mobilities and diffusion coefficients) of electrons and other charged species, as well as the coefficients for the reactions involved, are summarized in Table 3-2. The ionization and attachment coefficients and the electron mobility used here are the ones

which were reported in [45, 56, 58]. Different functions for these coefficients were reported in [70], which result in more intense ionization. The mobilities of positive and negative ions reported in [70] are used in the current model. It should be mentioned that the model is very sensitive to these parameters, especially to the ionization and attachment reaction coefficients. This sensitivity reflects both in the numerical stability of the model and accuracy of the results. Sensitivity analysis of the model to these parameters is discussed in Chapter 5.

Table 3-2: Swarm parameters used in the simulation [56, 70]; $\vec{E}$ in(V/m).

Parameter	Value	Unit
Ionization coefficient α	$3.5 \times 10^5 \exp(-1.65 \times 10^7/|\vec{E}|)$	$[1/m]$
Attachment coefficient η	$1.5 \times 10^3 \exp(-2.5 \times 10^6/|\vec{E}|)$	$[1/m]$
Coefficient of recombination of positive and negative ions k_{ep}	2×10^{-13}	$[m^3/s]$
Coefficient of recombination of positive ions and electrons k_{np}	2×10^{-13}	$[m^3/s]$
Mobility of electrons μ_e	$1.9163 \times |\vec{E}|^{-0.25}$	$[m^2/(Vs)]$
Mobility of positive ions μ_p	2.43×10^{-4}	$[m^2/(Vs)]$
Mobility of negative ions μ_n	2.7×10^{-4}	$[m^2/(Vs)]$
Diffusion coefficient of electrons D_e	0.18	$[m^2/s]$
Diffusion coefficient of positive ions D_p	0.028×10^{-4}	$[m^2/s]$
Diffusion coefficient of negative ions D_n	0.043×10^{-4}	$[m^2/s]$

The Negative corona is a self-sustained discharge, which requires a source of secondary electrons in order to produce consecutive pulses. Collision of positive ions to the corona needle surface causes the secondary emission flux of electrons into the domain:

$$\Gamma_e = \gamma n_p \mu_p |\vec{E}| \qquad\qquad (\text{3-14})$$

where $\Gamma_e(1/m^2 s)$ represents the flux of secondary electrons on the needle surface and γ indicates the secondary emission coefficient. The value of γ is assumed 0.01 in the current model [70]. It should be noted here that other than the secondary electrons resulting from collision of positive ions to the needle surface, natural ambient electrons can exist in the air gap as well. Once the discharge is initiated, these electrons are negligible in the negative discharge compared to the ones resulting from Eq. 3-14, however they are needed for initiating the discharge.

3.1.2   Numerical method

Although FEM has proved to be a very effective tool for modeling the corona discharge phenomenon [45, 56], it requires some stabilizing strategies for achieving a convergent solution. Various authors have tried different methods by combining FEM with other techniques. Sattari et al. [53, 55, 70] used a combination of FCT for solving the charge transport equations and FEM for solving the Poisson's equation. Zhang et al. [52] developed a model with a combination of the Boundary Element Method (BEM) and FEM for solving the electric field and Method of Characteristics (MOC) for solving the distribution of charged species.

One of the common methods for stabilizing the FEM, when it is used for solving transport equations, is to use artificial isotropic diffusion (ID). The way this type of stabilization works is that instead of solving the convection-diffusion problem with the physical diffusion coefficient D, the stabilized diffusion coefficient $D_{stab}=D+D_{art}$ is used, in which $D_{art}=\delta h|v|$, where $0<\delta<0.5$ is the tuning parameter, h is the longest side length of the mesh element and $|v|$ is the drift velocity of the charged species. This method is considered as being an inconsistent one, as it obviously alters the original problem by adding artificial diffusion in all directions. The stabilization method used in this paper is based on streamline diffusion (SD), which is different from the above-explained method. It is well-established in the literature that SD is considered as a consistent stabilization method which doesn't perturb the original problem and adds diffusion only in the direction of the electric field [71, 72]. The fundamental reason for this method being consistent is that the added stabilizing term approaches to zero if the approximate solution approaches the exact solution of the convection-diffusion problem. As a result, as the solution error is decreasing by consecutive iterations, the stabilizing term is vanishing [71]. It is proved in the literature that the SD is less stable than the ID, but is more accurate. The accuracy of ID is at best O(h), but the accuracy of SD is at least O $(h^{p+1/2})$, where p ≥ 1 is the order of the basis function [73].

Another consistent method, which is more time consuming as compared to SD, is called crosswind diffusion (CWD); it adds some diffusion in the direction perpendicular to the

electric field [72]. Generally, CWD is suitable for models with higher electric field [74]. Both the SD and CWD are categorized as anisotropic diffusion methods.

Due to the nature of the problem, which exhibits a very non-uniform and strong electric field near the needle tip, a non-uniform triangular mesh was used (Figure 3-2). The size of the elements varies from 0.75µm at the needle tip to 400 µm in the area far from the needle tip. The total number of elements in the computational domain exceeds 240,000 which results in approximately 900,000 degrees of freedom by having linear and quadratic discretization for continuity equations and Poisson's equation, respectively. Each simulation, which was carried out using a desktop PC with Intel Core i7-4960 CPU, takes between 12 to 72 hours to complete.

A Gaussian distribution of neutral plasma (electrons and positive ions) is assumed as initial conditions [56]:

$$n_{e,p} = n_{max} \times \exp\left(-\frac{(r-r_0)^2}{2s_0^2} - \frac{(z-z_0)^2}{2s_0^2}\right) \qquad (\,3\text{-}15\,)$$

where $n_{max} = 10^{12}$ 1/m³ is the maximum density, (r_0, z_0) are the coordinates of needle tip, and $s_0 = 25\mu m$ is the radius of initial distribution. Zero initial density is assumed for negative ions.

3.2   Simulation results

The discharge current is calculated using the method proposed by Sato [75]. This method is based on the energy balance in the discharge gap, which involves the movement of charged species under the effect of electric field:

$$I = \frac{1}{|V|} \iint_S 2\pi r \left(\mu_e n_e + \mu_p n_p + \mu_n n_n\right) \vec{E}.\vec{E}_L dr dz \qquad (\,3\text{-}16\,)$$

where r and z are cylindrical coordinates, $\vec{E}_L$ is the Laplacian electric field, V is the applied voltage on the needle and S is the 2D axisymmetric domain.
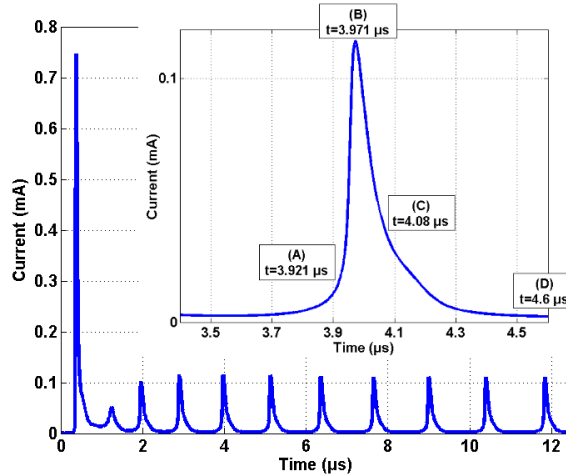
Figure 3-3: Current pulses for the model with -4 kV corona voltage; needle-plane spacing and tip radius are 6 mm and 35 µm, respectively.

Figure 3-3 illustrates the predicted current pulses for -4 kV supply voltage along with the magnified view of an individual pulse. The rise time (10% to 90%) of the pulse is 64 ns and the decay time (90% to 10%) is 240 ns. The rise time of the obtained pulse doesn't agree with the findings of the other authors [51, 56] and is longer than reported by them. However, we have found that the temporal characteristics of the pulse strongly depends on different model coefficients, most importantly the ionization reaction coefficient; e.g. 5% and 10% increment in the ionization reaction coefficient will reduce the rise time to 51 ns and 45 ns respectively. The ionization reaction coefficients reported in the literature vary by a factor of up to 3 [45, 70] and the one we used is the smallest one. We preferred to choose all parameters (including the reaction rate coefficients) from a single database rather than picking parameters from different sources.

Four different stages of formation of the Trichel pulse, which are labeled in the magnified view of Figure 3-3, are identified below.

3.2.1   Stage A, pulse initiation

In this stage, clouds of electrons, and positive and negative ions are created in the vicinity of the needle tip from the seed electrons due to ionization and attachment reactions; the positive ions are closer, while the negative ions and electrons are farther from the corona electrode. Two different regions can be distinguished in the air gap: the ionization region,

28

in which the ionization reaction is dominant due to the intense electric field, and the drift region, in which the attachment reaction is dominant due to the weaker electric field. The border between both regions is somewhere between the clouds of positive and negative charges.
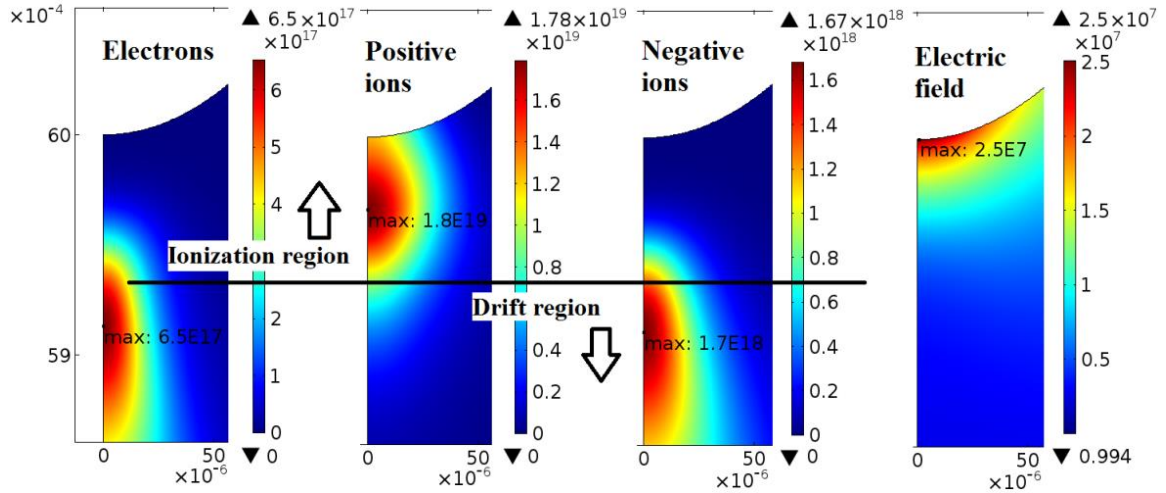
Figure 3-4: Distributions of charged species during stage A as indicated in Figure 3-3. All densities are in $(1/m^3)$ and the electric field is in (V/m). The approximate border between ionization and drift regions is marked with the horizontal solid line. Horizontal and vertical axes are in (m).

Figure 3-4 illustrates the distributions of charged species at this stage. Chen and Davidson [9] have defined a third region called the plasma region in which the corona-enhanced chemical reactions are possible and besides covering the ionization region, it extends a few millimeters into the drift region [10]. For the purpose of the current study though, we divide the gap into two regions only.

The presence of positive charges near the needle tip increases the electric field in the ionization region leading to a very fast build-up of new electrons and positive ions by the ionization reaction. As the electrons (already existing ones and new ones) are repelled away from the ionization region, negative ions are accumulating due to the attachment reaction right at the edge of the drift region. As positive ions are moving towards the needle, the ionization region is getting narrower and narrower during this stage. Positive ions are also deposited on the needle, but the rate of production of new positive ions by the ionization

reaction is much greater than that of absorption by the needle. The process of narrowing the ionization region continues until the next stage.
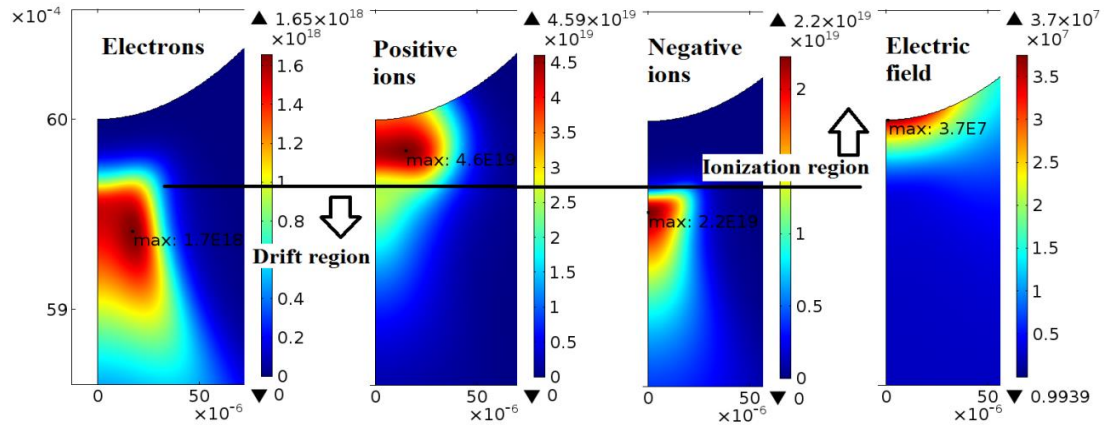
Figure 3-5: Distributions of charged species and electric field at the instant of the electric field being suppressed (stage B as indicated in Figure 3-3). All densities are in $(1/m^3)$ and the electric field is in (V/m). The width of the ionization region is considerably narrower compared to Figure 3-4. Horizontal and vertical axes are in (m).

3.2.2   Stage B, electric field suppression

At this stage, the ionization region has its narrowest width (approximately 30 µm) which results in limiting the production of new electrons (Figure 3-5). Thus, despite the increasing peak value of the electric field at the needle tip, the peak-value of electron concentration starts reducing at this stage followed by an immediate reduction of the peak value of the positive ion concentration (Figure 3-6). On the other hand, the cloud of negative ions is dense enough to suppress the electric field in the area between the ion cloud and the tip of the needle. This leads to the reduction of the peak value of the electric field. About 10 nanoseconds later, the current magnitude will also start to decrease. Finally, after a relatively long delay, the peak-value for the negative ion concentration also starts decreasing. So, the time sequence of reduction in the peak values at this stage which is shown in Figure 3-6 is electrons, positive ions, electric field, current and negative ions. It is also interesting to note that the location of the peak densities of electrons and positive ions are not on the axis of symmetry but situated approximately 20 µm away from the axis.

It is not clear whether the off-axis peak point of electron density at this stage is due to a numerical artifact or due to a real physical reason such as the diffusion of electrons. This phenomenon has been observed by other authors in the past [56] as well and the reason is not quite clear. While Tran et al. [56] don't rule out the possibility of a real physical reason, they also suspect that the inaccurate representation of 3D phenomenon in 2D axisymmetric geometry could be a possible reason.
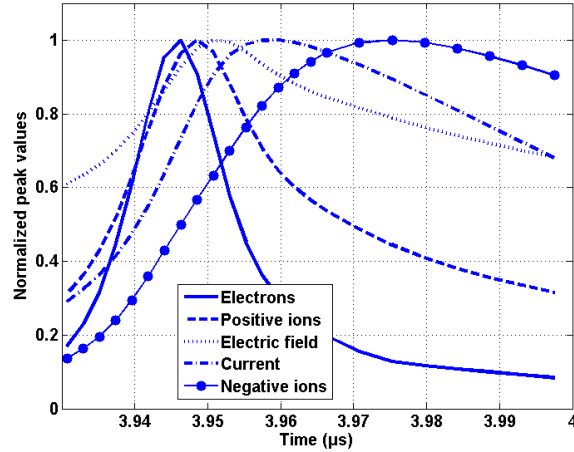
Figure 3-6: Normalized peak values of charged species' concentration, electric field, and current as a function of time during stage B as indicated in Figure 3-3.

3.2.3   Stage C, drift of negative ions
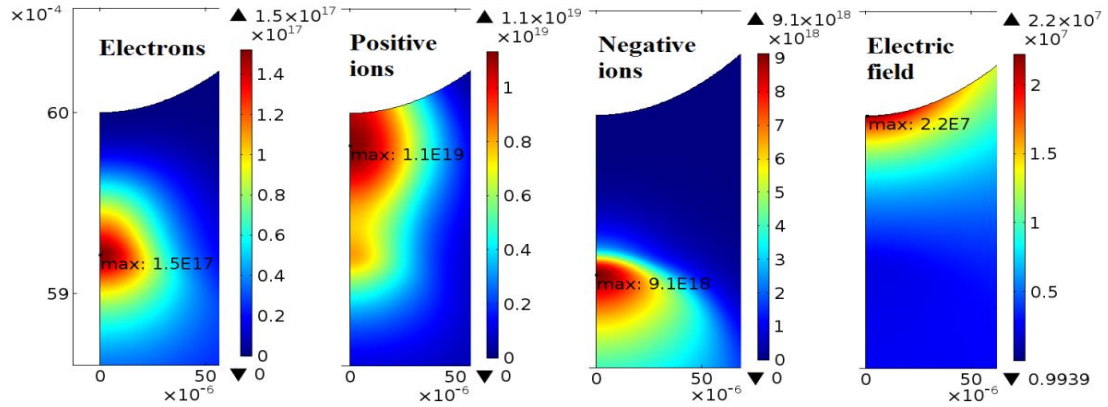
Figure 3-7: Distributions of charged species and electric field during stage C as indicated in Figure 3-3. All densities are in $(1/m^3)$ and the electric field is in (V/m). Horizontal and vertical axes are in (m).
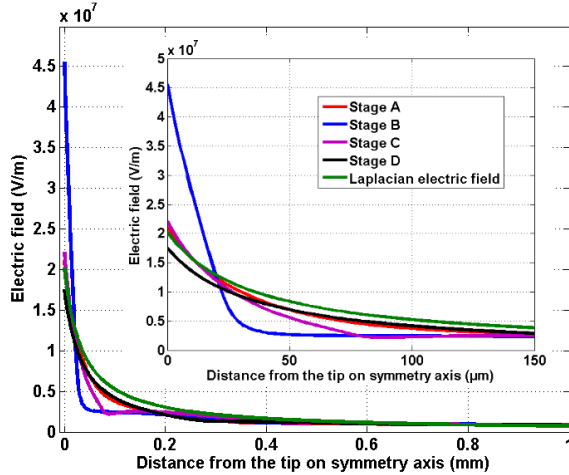
Figure 3-8: Electric field along the axis of symmetry at different stages of formation of Trichel pulse as indicated in Figure 3-3. Electric field during stage B has the greatest value near the tip. It is also noticeable that the electric field in the whole air gap in stage D is below the Laplacian electric field.

After the electric field falls below the ionization level in the majority of the air gap near the needle tip, the dissipation rate of positive ions and electrons will be larger than their production rate. In this stage, before the positive ions peak concentration reaches the cathode, the points of the peak concentration of the positive and negative ions are still close enough to be able to weaken the Laplacian electric field in the area in between. Thus, some positive ions are left behind the main positive cloud and form an island of trapped positive charges just at the top of the point of the negative ions' peak concentration (Figure 3-7). This weakened electric field behind the main cloud of positive ions is noticeable as a small dip on the curve of stage C in Figure 3-8 in the area between 5 and 10 µm away from the tip. At some later time, the positive ions left behind will be absorbed by the needle as well.

3.2.4   Preparation for next pulse

As the process of absorbing positive ions continues, secondary electrons are ejected from the needle surface into the gap according to Eq. 3-14. As shown in Figure 3-8, during this stage, the electric field has its lowest magnitude in the area near the tip of all the stages. Actually, this field is below the Laplacian electric field in the whole air gap. After negative ions have moved far enough from the tip, the electric field near the cathode recovers and

electrons from secondary emission get the chance to trigger the avalanche ionization for the next pulse.
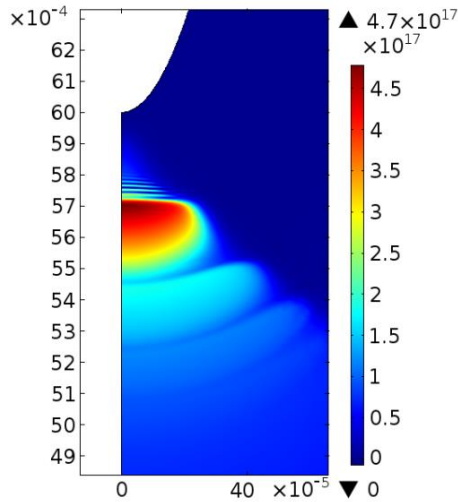
Figure 3-9: Distribution of negative ions during stage D as indicated in Figure 3-3. Each separate cloud represents the formation of one pulse. Due to the diffusion of negative ions, after some distance, the clouds are not distinguishable. Horizontal and vertical axes are in (m).

The preparation time (inter-pulse time) is much shorter than the time needed for a cloud of negative ions to travel from the point near the cathode to the ground plane. The frequency of the pulses is related to the drift of the cloud of negative ions from the needle tip, but it doesn't necessarily mean that the formation of the next pulse will start only after the cloud of negative ions has reached the ground plane. This confirms the concept of the existence of several clouds of negative ions in the air gap at any time rather than just one negative ion cloud [37]. The next pulse in the train of pulses will come as soon as the latest cloud of negative ions has moved far enough from the tip and the electric field increases above the onset level. The existence of several clouds of negative ions can be seen in Figure 3-9. This figure could also be used as the basis for explaining the fact that the consecutive pulses in Figure 3-5 have a smaller magnitude than the first pulse. In fact, the magnitudes of pulses are gradually becoming smaller and smaller as the time passes in the model. The decrement of pulses' amplitude is not noticeable for the consecutive pulses in the scale of Figure 3-5 though. The first pulse forms in the gap which is free of negative ions and the electric field
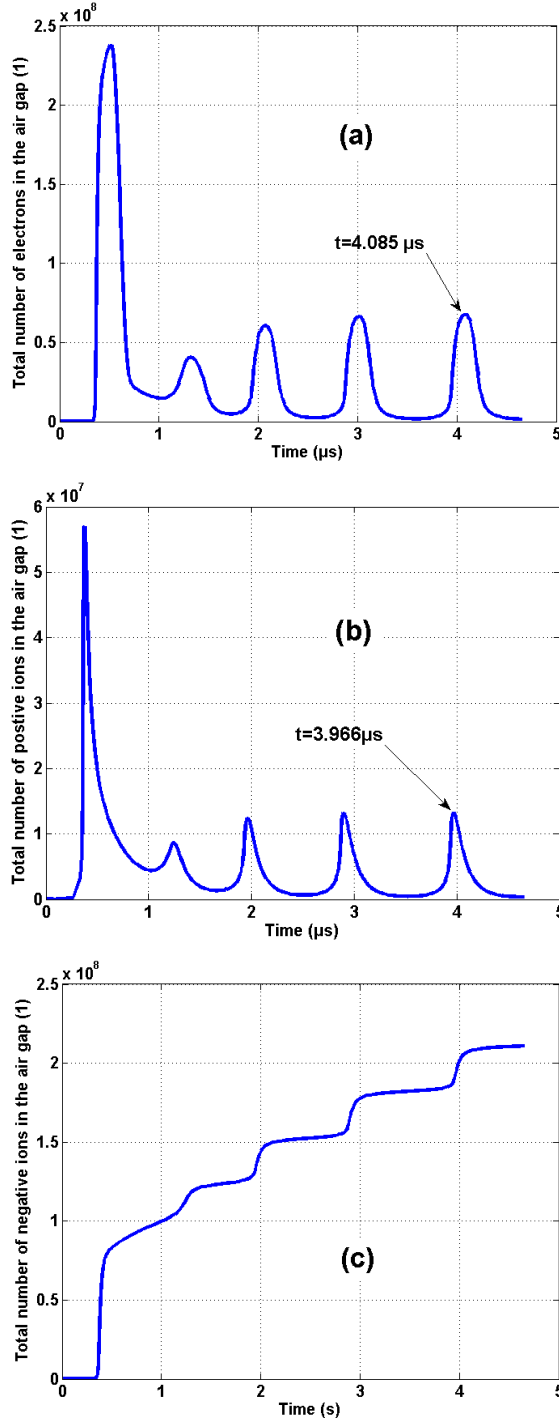
Figure 3-10: Total number of (a) electrons, (b) positive ions and (c) negative ions in the air gap versus time.

gets the chance to increase further. However, this is not the case for consecutive pulses. As the gap is filling with negative ions, the electric field gets suppressed faster for consecutive

pulses which causes the amplitudes to become smaller and smaller. Steady state amplitude will be reached once the forefront of negative ions bridges the whole gap.

Figure 3-10 depicts the total number of charged species in the air gap versus time. It can be observed in this Figure that the total number of electrons and positive ions follow the same trend as current, but the total number of negative ions in the air gap is increasing after each pulse. These findings are consistent with those reported in [55]. Each incremental step in Figure 3-10(c) is an indicator of one Trichel pulse. These step increments should reach steady-state at some point if the model is let run long enough to allow the negative ion clouds to fill the air gap. Comparing the maximum points on Figure 3-10(a) and (b), it can be observed that despite the fact that the peak density of electrons starts decreasing before the positive ions (as shown in Figure 3-6), the total number of electrons holds longer than the total number of positive ions during the stages which the current pulse starts decreasing (stage B). This could be justified by the fact that the positive ions are being absorbed very fast by the needle during this stage which reduces its total number in the air gap, whereas the local production of positive ions due to ionization still continues for a short time. Moreover, by comparing Figure 3-6 and Figure 3-10 (a and b), it is revealed that the peak value of electric field starts decreasing before the total number of electrons and positive ions in the air gap start to reduce.

Figure 3-11 depicts the distribution of current density on the cathode surface at different instants of formation of a Trichel pulse. Starting from the tip of the needle, it is observed that the current density propagates like a wave on the needle surface. This phenomenon was reported before in [51]. The change of sign of current density along the cathode surface on curve 2 is explained as being due to the displacement current variation produced by a change in the electric field [51].
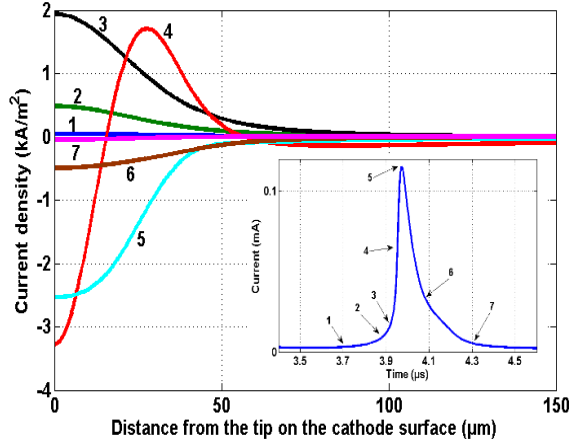
Figure 3-11: Distribution of the current density on the cathode surface at different instants of formation of a Trichel pulse.
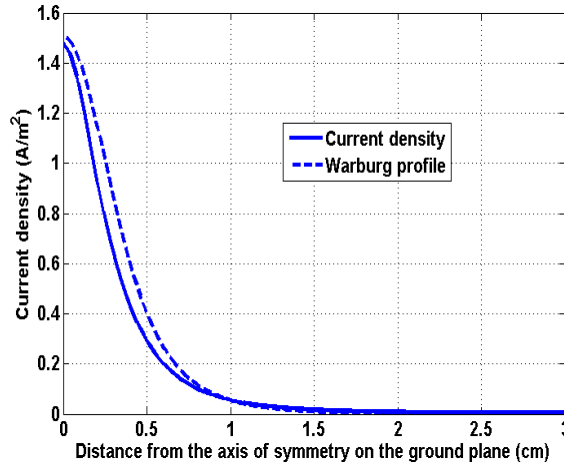
Figure 3-12: Comparison of the Warburg profile with the calculated current density on the ground plane at the instant of current peak.

Moreover, comparison of the Warburg profile [76] with the current density on the ground plane at the peak of the current (stage B as shown in Figure 3-3 or the instant 5 as shown in Figure 3-11) shows a great agreement. This comparison is presented in Figure 3-12. It should be mentioned here that the surface integral of any of the curves given in Figure 3-11and Figure 3-12 agrees with the value of the total current.
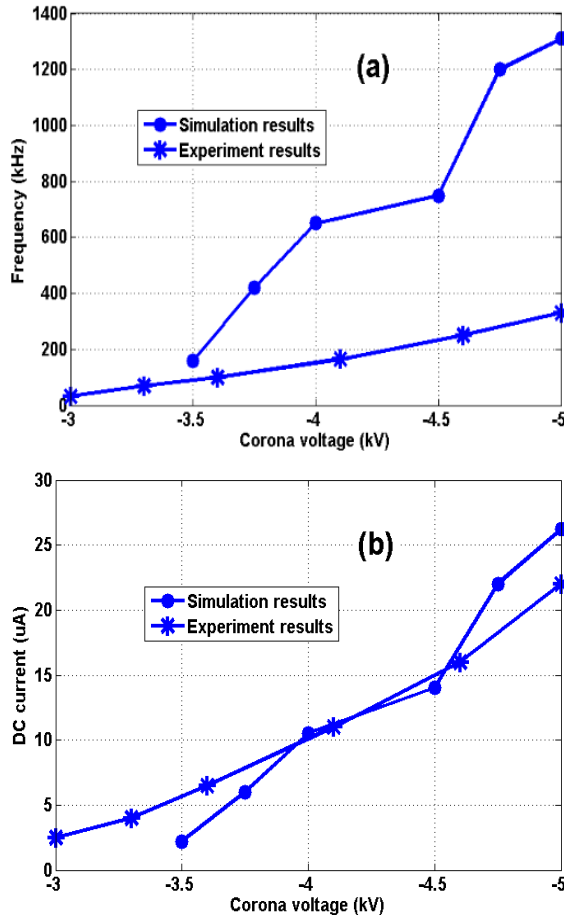
Figure 3-13: Comparison of simulated and experimental (a) frequencies, and (b) DC currents for different voltages. The needle-plane spacing and radius of curvature of the tip are 6 mm and 35 µm, respectively.

3.3 Comparison with experimental data

For the purpose of assessing the validity of the proposed model, results of pulse frequency and average DC current for different negative voltages on the needle are compared with the experimental data published by Lama and Gallo [37]. They reported results for a needle of 35 µm radius of curvature for voltages ranging from -3 kV to -5 kV. In the simulations, however, the corona pulses were not observable for voltages smaller than -3.5 kV. Therefore, the range of compared results with the experiments is from -3.5 kV to -5 kV. The comparison, which is presented in Figure 3-13, gives an acceptable agreement for the DC currents. The results for the frequency, however, are less satisfactory and suggest that some of the parameters in the model need to be adjusted. The coefficient of secondary

emission of electrons (γ) and also the ionization coefficient (α) play major roles here. Other simplifications in the assumed model, such as neglected photoionization, photoemission, many ionic and excited species and reactions, may be responsible for lack of a better agreement as well.

3.4   Transition to glow discharge regime

As the negative voltage on the needle is increased, the frequency of the Trichel pulses increases and the negative ion clouds get closer and closer to each other until finally they merge and form a relatively flat curve, which is called the glow discharge. The typical range of the current in this regime is normally one order of magnitude greater than that of the Trichel pulse regime. Due to the fast transition of Trichel pulse regime to spark regime in atmospheric pressure, in reality, it is difficult to realize steady-state glow discharge at atmospheric pressure. In fact, the stable glow discharge is classically known to exist only in low pressure sealed gas tubes [8], however, this regime is achievable at atmospheric pressure by introducing a gas flow in the gap which quenches the thermal instabilities by the convective removal of energy dissipated in the discharge [77]. Changing the shape of the anode to that of a crater right below the needle tip could be used to stabilize the glow regime as well [8].

The current model doesn't include the thermal instabilities of the formed plasma channel in the air gap and it's assumed that the discharge is stabilized using at least one of the abovementioned methods. With this assumption, the main features of glow discharge in the presented geometry (Figure 3-1) are predicted here. These features are: formation of a plasma channel all the way from the needle to the ground plane, which is deduced by the uniform distribution of negative and positive charges in the air gap, the enhancement of electric field in the drift region, and formation of the anode layer (the glow region near the anode, which is observed as visible blue film on the ground plane). The transition from Trichel pulse regime to glow discharge starts as the ratio of pulse peak to the minimum current starts decreasing. The pulse peak in the Trichel pulse regime is typically 20 times greater than the minimum current. In the current model, this ratio decreases from 7 to 3 for

the voltage range from -7 kV to -10 kV. Finally, the glow regime is reached at -12 kV. The currents for -9 kV and -12 kV discharges are shown in Figure 3-14.
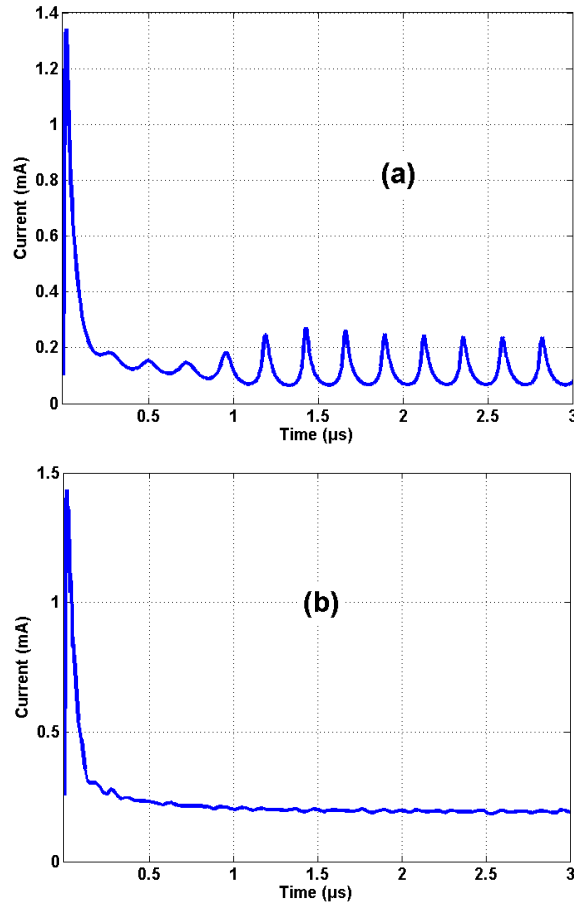
Figure 3-14: Current waveforms for (a) -9 kV, and (b) -12 kV. According to the simulations, the transition to the glow discharge regime starts from -6 kV and at -12 kV Trichel pulses completely disappear.

Comparison of the Poissonian and Laplacian fields in the area far from the needle for the -12 kV shows an enhancement of electric field in the area near the ground plane (Figure 3-15, blue line). As it can be observed in this Figure, the electric field enhancement to a level at which the ionization reaction overcomes the attachment reaction arises at first at the anode. In fact, putting the ionization and attachment coefficients in Table 3-2 equal with each other will lead to E=2.57×10^6 (V/m). This phenomenon, which is associated with the formation of a clearly visible blue layer on the ground plane in the experiment has been explained before by Akishev et al. [8]. This layer is called the "anode layer".

39
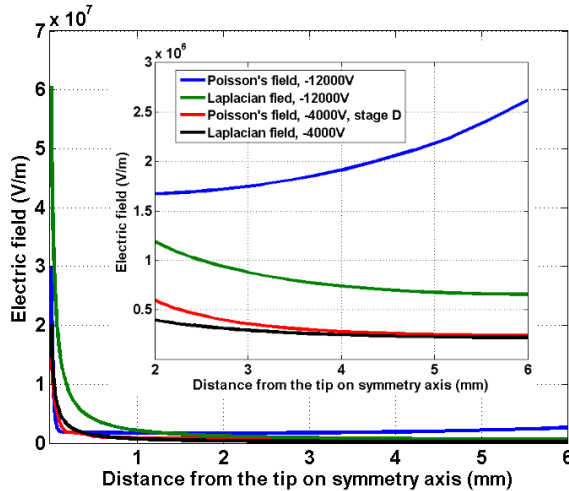
Figure 3-15: Comparison of Poisson's field and Laplacian field along the axis of symmetry for -4 kV and -12 kV. The magnified view is for the area near the ground plane.

Actually, we believe the key factor controlling the transition from the Trichel pulse regime to glow discharge regime is the electric field which should be strong enough throughout the whole gap. This was not the case in the Trichel pulse regime, in which the strong electric field was limited to the ionization region. On the other hand, the negative ions have smooth distribution in the air gap in the glow discharge regime rather being in the form of separate packs which was the case in the Trichel pulse regime (Figure 3-9). The smoothness of the distribution of the negative ions is observable in Figure 3-16. This Figure illustrates the distributions of different charged species and the electric field in the -12 kV discharge. It should be stressed here again, that the realization of these circumstances in reality is not possible without applying air flow (for removing heat) and crater-shaped ground plane for avoiding the initiation of breakdown right under the tip, on the ground plane [8].
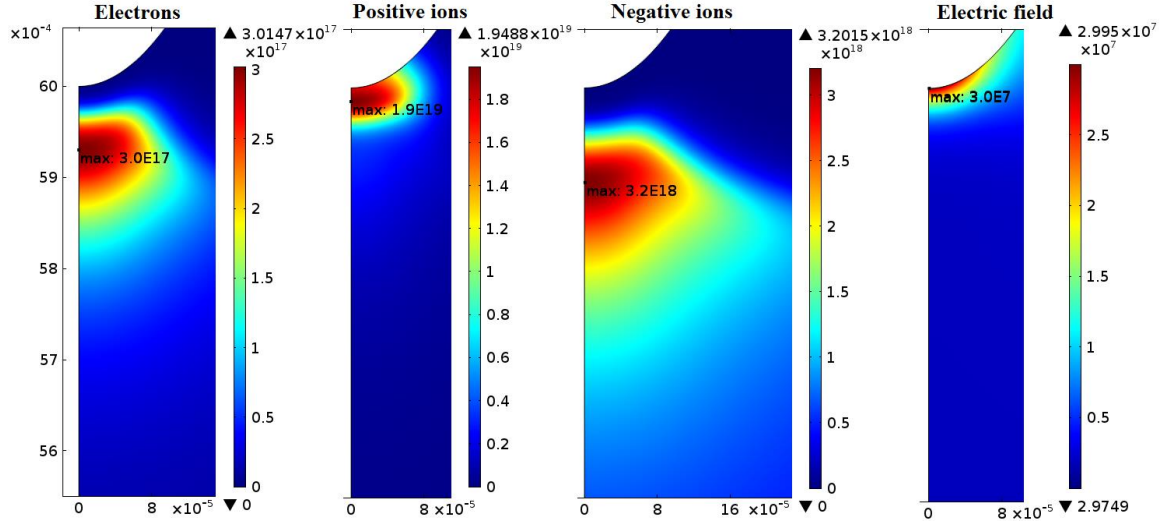
Figure 3-16: Distributions of charged species and electric field during glow discharge regime (-12 kV). All densities are in $(1/m^3)$ and the electric field is in (V/m). Horizontal and vertical axes are in (m).

Figure 3-17 represents the comparison of the densities of ions and also the ionization source terms along the axis of symmetry from needle tip to the ground plane for glow discharge (-12 kV) and Trichel pulse discharge (-4 kV). It can be observed that the whole air gap is filled with positive and negative ions during the glow discharge, which is the result of enhanced electric field and formation of plasma channel in the gap. Complete filling of the gap by plasma means that the transition to glow discharge is completed [8]. It should be noted here that the curve of the positive ions in the -12 kV discharge is not extended to the end in this Figure. The reason for that is the fact that the positive ions have zero boundary condition on the ground plane and the vertical axis has a logarithmic scale. Moreover, due to the coarse mesh in the area near the ground plane, approximately 400 µm, the density jumps from around 1e15 $(1/m^3)$ to zero.
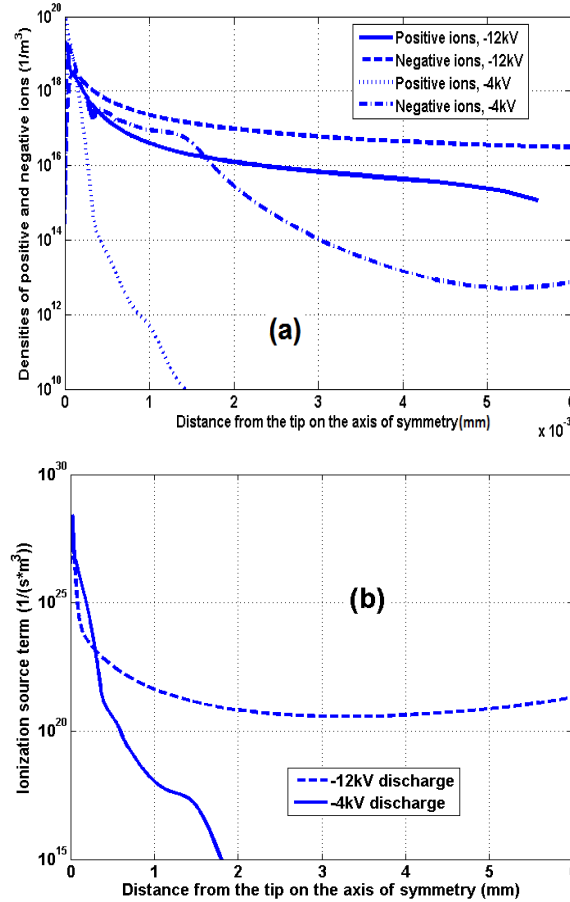
Figure 3-17: Comparisons of (a) the densities of ions and (b) the ionization source term, along the axis of symmetry for glow discharge (-12 kV) and corona discharge (-4 kV).

3.5   Conclusions

The formation of Trichel pulses in the negative corona discharge in the air has been numerically investigated in this chapter. The computational model is based on solving the drift-diffusion equations for three basic ionic species and the Poisson equation for the electric field. The results show the temporal evolution of the major distributed parameters (density of ionic species, electric field) as well as the global measured parameter, the electric current.

Different stages in the pulse formation have been identified. In the first stage (pulse initiation), the presence of a dense cloud of positive ions near the tip enhances the electric field in the area near the needle tip. This process continues until the clouds of negative and

positive ions are dense enough to diminish the electric field in the ionization region. Off-symmetry axis peaks were noticed for electrons and positive ions in the stage of diminishing electric field. It was shown that the peak values of different ionic densities occur at different instants of time. After the cloud of negative ions drifts sufficiently far away from the needle, the electric field gets the chance to recover in the area near the tip and with the help of the secondary emission of the electrons, the gap will be ready for the next pulse. It was shown that in the Trichel pulse regime, several clouds of negative ions simultaneously exist in the air gap and the inter-pulse time is shorter than the time takes for a cloud of negative ions to cross the gap. The fact that the first pulse in the train of Trichel pulses had greater amplitude than the consecutive ones was explained by the absence of negative ions in the air gap while the first pulse is being formed.

Comparison of the simulation and experimental results shows a good agreement for DC currents and an acceptable one for frequencies. Moreover, the numerical model predicted the inception voltage of corona discharge -3.5 kV, which is higher than the one reported in the experiments (-3 kV).

The numerical model predicts that the transition from the Trichel pulse to glow discharge regime for a needle-plane configuration with 6 mm spacing and 35 µm tip with atmospheric pressure air concludes at -12 kV, as the current waveform becomes flat and a plasma channel is formed from the cathode to the anode. The simulations showed that the augmentation of the electric field in the area far from the needle tip in the glow discharge regime starts from the ground plane which is associated with a clearly visible blue film on the ground plane in the experiments.

Chapter 4

4 « Study of the impact of photoionization on negative and positive needle-plane corona discharge in atmospheric air »

In this Chapter, a 2D axisymmetric model of the atmospheric pressure needle-plane corona discharge incorporating the photoionization phenomenon is presented. In simple words, the Eqs. 3-1 to 3-4 presented in Chapter 3, are solved along three more equations to incorporate the photoionization phenomenon. The model presented in this Chapter is solved for both polarities of the corona discharge, positive and negative.

In general, most of the studies published in the literature regarding photoionization are limited to the streamers in positive discharges [69, 78] and it is generally accepted that it is photoionization that is the major source for the production of seed electrons ahead of the cathode-directed streamers [79], while negative streamers have attracted much less attention [63]. To the author's best knowledge, no quantitative studies of photoionization in the corona discharges (both positive and negative) and its comparison with other sources of production of electrons in those discharges could be found in the literature. Moreover, although there are many three-species, self-sustained negative corona models studied in the literature, in the case of the positive corona models, they are mostly limited to single and two-species ones. The main focus of this Chapter is to present three-species, self-sustained, positive and negative corona discharge models including the photoionization phenomenon. These models will enable us to conduct a quantitative study of the impact of photoionization on the characteristics of Trichel pulses (frequency and DC current of the pulses) and its vital role in sustaining the positive corona. Also, a comparison of the relative importance of the different sources of production of electrons in positive and negative corona discharge will be presented. Fulfilling these purposes requires a fast computation method for including the photoionization in the corona discharge model. The method suggested by Bourdon et al. [64], which is based on the model developed by Luque et al. [63] and also used in [69], is implemented here. In this method, the photoionization phenomenon is modeled with the help of three Helmholtz equations which consist of some

tuning coefficients. There was significant uncertainty over the values of some key coefficients in the suggested model. To be able to accurately incorporate the photoionization phenomenon in the negative corona discharge, as a first step, these coefficients needed to be accurately determined. Since photoionization is the main source of producing electrons for sustaining a positive corona discharge, the coefficients were determined by comparing the results of the positive corona numerical model and the experimental results presented in [57].

In the first two sections of this Chapter, the physics behind this phenomenon and the challenges in numerical calculations are described. The next two sections are devoted to implementing the equations describing the photoionization in the positive and negative corona discharge models. The results are compared with the existing experimental data in the literature and some new insights have been presented at the end regarding the relative importance of the different sources of production of new electrons in both positive and negative discharges.

4.1 Photoionization model in atmospheric air

It is generally accepted in the literature that the photoionization in the air is the result of the absorption by oxygen molecules of photons emitted from excited nitrogen molecules [62, 65]. Zheleznyak et al. [66] suggest the radiation emitted by the singlet states $N_2(b^1 \Pi, b'^1 \Sigma_u^+, c^1 \Pi_u$ and $c'^1 \Sigma_u^+)$ in the wavelength range of 98-102.5 nm is the source of this phenomenon. The excitation of the nitrogen molecules is the result of the impact of the energized electrons accelerated in the electric field [66]:

$$e + N_2 \rightarrow N_2^* + e \Rightarrow N_2^* \rightarrow N_2 + h\nu(98 - 102.5nm) \Rightarrow O_2 + h\nu \rightarrow O_2^+ + e \qquad (4\text{-}1)$$
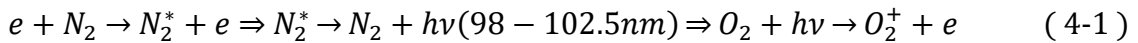
The photoionization process plays a vital role in the propagation of positive streamers in gasses and has been studied most often in this framework [69, 78]. It is generally assumed to be the only mechanism for the production of seed electrons causing the propagation of the cathode-directed streamers [79]. This phenomenon was also studied by a few authors for the propagation of negative streamers [63].

The classical numerical model of photoionization in air was suggested by Zheleznyak et al. [64, 66]:

$$S_{ph}(\vec{r}) = \iiint_{V'} \frac{I(\vec{r'})g(R)}{4\pi R^2} dV' \qquad (\,4\text{-}2\,)$$

where $S_{ph}(\vec{r})$ is the rate of photoionization at the point of observation $\vec{r}$, $I(\vec{r'})$ is the emission of ionizing UV photons from source point $\vec{r'}$ due to the impact ionization reactions, $R = |\vec{r} - \vec{r'}|$ is the distance between source and observation points and, finally, $g(R)$ is the absorption function. This Equation should be integrated over the whole domain (or at least over the effective range of the photoionization emitting source) for finding the rate of photoionization at each point of observation. As suggested by this Equation, photoionization is a nonlinear function of the electric field. In addition, the photoionization at a given point occurs due to the radiation source at another point. This introduces non-locality to the problem. Handling the non-locality of this phenomenon is computationally very demanding. The function $g(R)$ is defined by:

$$\frac{g(R)}{p_{O_2}} = \frac{\exp(-\chi_{min}p_{O_2}R) - \exp(-\chi_{max}p_{O_2}R)}{p_{O_2}R \ln(\chi_{max}/\chi_{min})} \qquad (\,4\text{-}3\,)$$

where χ_{max} and χ_{min} are the maximum and minimum values of the absorption coefficients of ionization radiation by oxygen in the wavelength domain 98-102.5 nm and their values are 2 Torr^{-1}cm^{-1} and 0.035 Torr^{-1}cm^{-1}, respectively [78]. Also, p_{O_2} is the partial pressure of molecular oxygen in atmospheric pressure air which is usually 150 Torr. The reason the left side of the Eq. 4-3 is divided with p_{O_2} is that the right side of the equation is preferred to be merely a function of $p_{O_2}R$ which is an important parameter for photoionization in oxygen-nitrogen mixtures [64, 66].

The function $I(\vec{r'})$ in Eq. 4-2 represents the emission of photons in the discharge volume, which is proportional to the number of ionizing collisions of accelerated electrons with the nitrogen molecules:

$$I(\overrightarrow{r'}) = \xi \frac{p_q}{p + p_q} S_i(\overrightarrow{r'}) = \xi \frac{p_q}{p + p_q} \alpha \mu_e |\vec{E}| n_e \qquad (4\text{-}4)$$

where ξ and p_q are the proportionality factor and the quenching pressure (in Torr), respectively, over which there is uncertainty in the literature [63, 65, 78]. The factor $p_q/(p + p_q)$ accounts for the probability of non-radiative de-excitation of nitrogen molecules due to the collision with other molecules [63]. $S_i(\overrightarrow{r'})$ is the rate of production of new electrons due to the impact ionization, which is equal to the product of the ionization coefficient (1/m), drift velocity of electrons (m/s) and number density of electrons (1/m^3). α, μ_e, $|\vec{E}|$ and n_e are the coefficient of ionization reaction, mobility of electrons, intensity of electric field (V/m) and concentration of electrons, respectively.

It seems that there is not a solid agreement over the values of p_q and ξ in the literature. Although everyone agrees that the factor ξ weakly depends on the electric field and the data in [66] shows that in the range of $150 \leq$ E/N ≤ 600 Td, ξ diminishes from 0.12 to 0.06 [78], in the works of Luque et al. [63] and Kulikovsky [78] it was assumed that $\xi = 0.02$ and $\xi = 0.1$, and p_q was assumed to be 60 and 30 Torr, respectively.

Instead of integrating Eq. 4-2, which is very time-consuming, the approach proposed by Bourdon et al. [64] is used here. This approach, which is based on the method suggested by Bourdon et al. [64] and used by Papageorgiou et al. [69] as well, interpolates the absorption function $g(R)$ by the sum of three exponential terms:

$$\frac{g(R)}{p_{O_2}} = p_{O_2} R \sum_{j=1}^{3} A_j \exp(-\lambda_j p_{O_2} R) \qquad (4\text{-}5)$$

Substituting this approximation in the Eq. 4-2 gives:

$$S_{ph}(\vec{r}) = \sum_{j=1}^{3} \left\{ \underbrace{\iiint_{V'} \frac{I(\overrightarrow{r'})(p_{O_2})^2 A_j \exp(-\lambda_j p_{O_2} R)}{4\pi R} dV'}_{S_{ph}{}^j(\vec{r})} \right\} = \sum_{j=1}^{3} S_{ph}{}^j(\vec{r}) \qquad (4\text{-}6)$$

The advantage of this method is that the term $S_{ph}{}^{j}(\vec{r})$ in above equation is the solution of the Helmholtz equation:

$$\left(\nabla^2 - \left(\lambda_j p_{O_2}\right)^2\right) S_{ph}{}^{j}(\vec{r}) = -A_j\left(p_{O_2}\right)^2 I(\vec{r}) \qquad (4\text{-}7)$$

where $I(\vec{r})$ and p_{O_2} are the same as defined in Eqs. 4-3 and 4-4, respectively, and the coefficients A_j and λ_j are the constant numbers given in Table 4-1 [69]. As the result of this approximation, the problem of solving Eq. 4-2, which is a very expensive from the numerical point of view, is replaced with the problem of solving three equations (Eq. 4-7) assuming $j=1,2$ and 3. It is noteworthy to mention that the reason the three-term exponential approximation is preferred over the two-term exponential approximation as compared in [64], is that the two-term approximation doesn't represent acceptable agreement with the absorption function suggested by Zheleznyak et al. [66] for the values of $p_{O_2}R$ greater than 50 Torr cm [64].

Table 4-1: Constant coefficients for Eq. 4-7

	$A_j(cm^{-2}Torr^{-2})$	$\lambda_j(cm^{-1}Torr^{-1})$
$j = 1$	1.986×10⁻⁴	0.0553
$j = 2$	0.0051	0.1460
$j = 3$	0.4886	0.89

4.2 Governing equations of the model

The corona discharge model incorporating the photoionization phenomenon consists of three continuity equations (responsible for the movement of three charged species: electrons, positive ions, and negative ions), Poisson's equation and three Helmholtz equations (responsible for the photoionization):

$$\frac{\partial n_e}{\partial t} + \nabla \cdot \left(-\mu_e \vec{E} n_e - D_e \nabla n_e\right) = S_{ph} + \alpha n_e \left|\mu_e \vec{E}\right| - \eta n_e \left|\mu_e \vec{E}\right| - k_{ep} n_e n_p \qquad (4\text{-}8)$$

$$\frac{\partial n_p}{\partial t} + \nabla \cdot \left(\mu_p \vec{E} n_p - D_p \nabla n_p\right) = S_{ph} + \alpha n_e \left|\mu_e \vec{E}\right| - k_{ep} n_e n_p \qquad (4\text{-}9)$$

$$\frac{\partial n_n}{\partial t} + \nabla \cdot \left(-\mu_n \vec{E} n_n - D_n \nabla n_n\right) = \eta n_e \left|\mu_e \vec{E}\right| - k_{np} n_n n_p \qquad (4\text{-}10)$$

$$\nabla^2 V = \frac{-e(n_p - n_e - n_n)}{\varepsilon_0} \qquad (\,4\text{-}11\,)$$

$$\left(\nabla^2 - \left(\lambda_j p_{O_2}\right)^2\right) S_{ph}{}^j(\vec{r}) = -A_j\left(p_{O_2}\right)^2 I(\vec{r}) \; ; \; j = 1,2,3 \qquad (\,4\text{-}12\,)$$

$$S_{ph} = \sum_{j=1}^{3} S_{ph}{}^j \qquad (\,4\text{-}13\,)$$

where $n_e, n_p, n_n, \mu_e, \mu_p, \mu_n, D_e, D_p, D_n$ and S_{ph} are the number densities ($1/m^3$), mobilities ($m^2/(Vs)$), and diffusion coefficients (m^2/s) of electrons, positive ions and negative ions, and the photoionization source term, respectively. Moreover, V, ε_0, and e represent the potential, vacuum permittivity, and the electron charge, all in SI units, respectively. Four main reactions: ionization, attachment of electrons to neutral molecules, recombination of electrons with positive ions and recombination of positive and negative ions, with the reaction coefficients $\alpha(1/m)$, $\eta(1/m)$, $k_{ep}(m^3/s)$ and $k_{np}(m^3/s)$, respectively, as explained in Chapter 3, are considered in the investigated model [45, 80].

4.3   Simulation results for positive corona discharge

The model consisting of Eqs. 4-8 to 4-13 is solved using a commercial finite element package COMSOL. The modules: "Transport of diluted species", "Helmholtz equation" and "Electrostatics" are used for the drift-diffusion equations, photoionization equations, and Poisson's equation, respectively. The studied models, which have either 6 mm or 2 cm air gap, consist of approximately 190,000 and 250,000 non-uniform triangular mesh elements, respectively leading to more than 1 million degrees of freedom. Drift-diffusion equations are numerically stabilized by streamline diffusion (SD). This is proven to be a very efficient method in this specific application [80]. The implicit method "backward differentiation formula" (BDF) is used for determining the time steps. BDF methods have been used for a long time and are known for their stability [81]. The boundary conditions for Eqs. 4-8 to 4-11 are the same as the conditions explained in [80].

Proper boundary conditions for the Helmholtz equations (Eqs. 4-11 and 4-12) are also necessary. Zheleznyak's equation (Eq. 4-2) is valid in an infinite space and in the investigated problem here a different Green function would be needed. The exact boundary conditions for the Helmholtz equation would need to consider the photon reflection from the needle surface and could vary between a complete reflection to a complete absorption. In order to simplify the problem, the zero Dirichlet boundary conditions at the boundaries of the computational domain were assumed [63, 69]. This boundary condition on the needle requires a very fine mesh in the adjacent area so a convergent model could be obtained. In all the models studied here, the maximum size of the mesh element in the immediate area of the needle tip is 1 micron and a mesh growth rate of 1.01 in the critical neighboring areas was imposed. It has been checked that the assumption of the zero boundary condition on the needle yields a solution very close to the solution of a model in which the results of Zheleznyak's equation were imposed on the needle.

In an attempt to reduce the uncertainties revolving around the values of p_q and ξ, we decided to assume $p_q = 60$ Torr and sweep the values of ξ in a range of $0.02 \leq \xi \leq 0.08$. The geometry of the model was chosen so the results of the positive corona discharge could be compared with the experimental results published in [57]. The needle-plane model consisted of a 2 cm air gap, a needle of 95 µm tip radius and an infinite ground plane. Best agreement was obtained for $\xi = 0.06$. The obtained I/V vs. V characteristics is illustrated in Figure 4-1. It can be noticed in this Figure that the onset voltage of the numerical model is higher than that of the experimental one. This issue, which has been noticed in other numerical models as well [80], could be explained by the existence of microscopic surface irregularities leading to microscopic field hot spots on the needle surface. These hot spots on the needle are ignored in numerical models.

After this stage, the established photoionization model was ready to be incorporated in the negative corona discharge developed previously in [80].
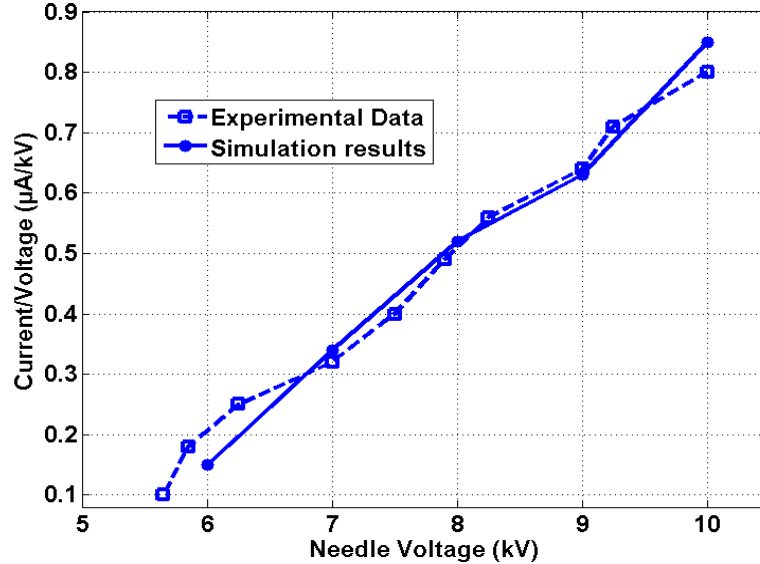
Figure 4-1: Validation of the simulation results of positive corona discharge for $\xi = 0.06$ with the experimental results published in [57]. The discharge model consists of a 2 cm air gap and a 95 µm tip radius.

4.4 Simulation results for negative corona discharge

For the purpose of quantifying the impact of photoionization phenomenon on the characteristics of the Trichel pulses produced in a negative corona discharge, the results of the Trichel pulse simulations reported in [80] were reproduced after including the photoionization process with the parameters established in the previous section. The geometry of the model consists of a 6 mm air gap between a needle with a 35 µm tip radius and a ground plane. All the simulations carried out in this report are for 2D axisymmetric models and the surrounding discharge gas is assumed to be air at 1 atm pressure. The comparison is made in the voltage range of -3.5 kV to -5 kV for the frequency of the pulses and the DC current. The comparison results shown in Figure 4-2 reveals an average of 5% increase in both the frequency and the DC current of the pulses. It should be noted here that the results presented in Figs. 1 and 2 have different geometries and the significant difference of the DC currents shouldn't be surprising (the DC currents in Figure 4-1 fall in the range of approximately 1 to 10 µA). The negative discharge model presented in Figure 4-2 has a much smaller air gap compared to the positive discharge model of Figure 4-1. Although the radius of curvature of the negative model is smaller than that of the positive

discharge, it is a generally proven fact that the smaller air gap leads to a larger current in the electrical discharges [37]. It should also be noted that the chosen voltage ranges for the Figure 4-1 and Figure 4-2 are in accordance with their respective compared experimental results (references [57, 80], respectively).
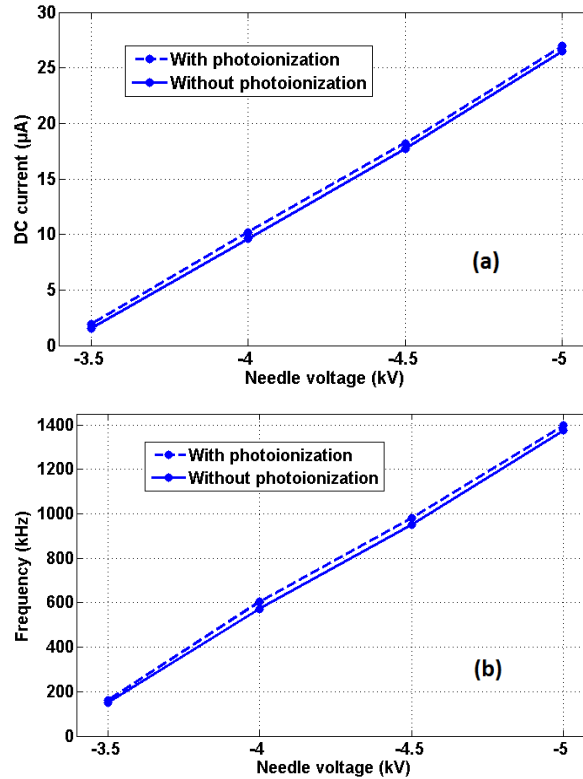
Figure 4-2: Comparison of (a) DC currents and (b) frequencies of Trichel pulses with and without photoionization source included. The negative discharge model presented here is the one which was investigated in [80] and consists of a 6 mm air gap and a 35 μm tip radius.

4.5   Discussions

Before conducting a quantitative comparison of the sources of production of electrons in corona discharge, photoionization, impact ionization, and secondary emission of electrons (only in the negative discharge), the correlation between photoionization and impact ionization should be clarified. Although, as stated in Eqs. 4-4 and 4-12, from a numerical point of view it appears that the photoionization source term is strongly dependent on the impact ionization source term, in reality, the photoionization is triggered by photons

produced from excited nitrogen molecules, not the electrons produced from impact ionization (Eq. 4-1). Nevertheless, in the literature, it is accepted that the number of the photons produced in the discharge volume is proportional to the number of ionizing collisions of accelerated electrons [66]. This approximation is reflected in the linearity and non-locality of the Helmholtz equations representing this phenomenon (Eq. 4-12). It should be noted that this assumption is not always valid; e.g., in the regimes of higher voltage discharges with rapidly moving ionization wave, excited nitrogen molecules could continue radiating photons for much longer time compared to the lower voltage regimes.

In this part, the results of two models with exactly the same geometry (6 mm air gap and 35 µm needle tip) and same voltage level, one with +4500 V and the other with -4500 V on the needle, are discussed and compared. The negative discharge model is actually the same as the one presented in Figure 4-2.

4.5.1   Positive corona discharge

Figure 4-3 depicts the distributions of the impact ionization and the photoionization source terms ($m^{-3}s^{-1}$) in the positive corona discharge in the area near the needle tip and along the axis of symmetry (the line starting from the needle tip and going straight downward to the ground plane). As it is shown in Figure 4-3 (a), the impact ionization electrons, which are mostly produced close to the tip (area of the strongest electric field), trigger the photoionization at a farther distance while getting quickly absorbed by the needle. On the other hand, electrons produced by photoionization trigger the impact ionization on their way towards the tip. Hence, the discharge is sustained. The non-locality of the photoionization is the key characteristic in sustaining the discharge which gives enough time for the photoionization electrons to gain enough energy as they accelerate through the increasing field thus triggering impact ionization. It is also noticed in Figure 4-3 (b) that the photoionization electrons are distributed in a much larger area compared to the impact ionization electrons which are concentrated only near the needle tip. Moreover, the difference of the peak concentrations shows that in the positive discharge, a small number of electrons produced from photoionization is enough for triggering the avalanche impact ionization and sustaining the discharge.
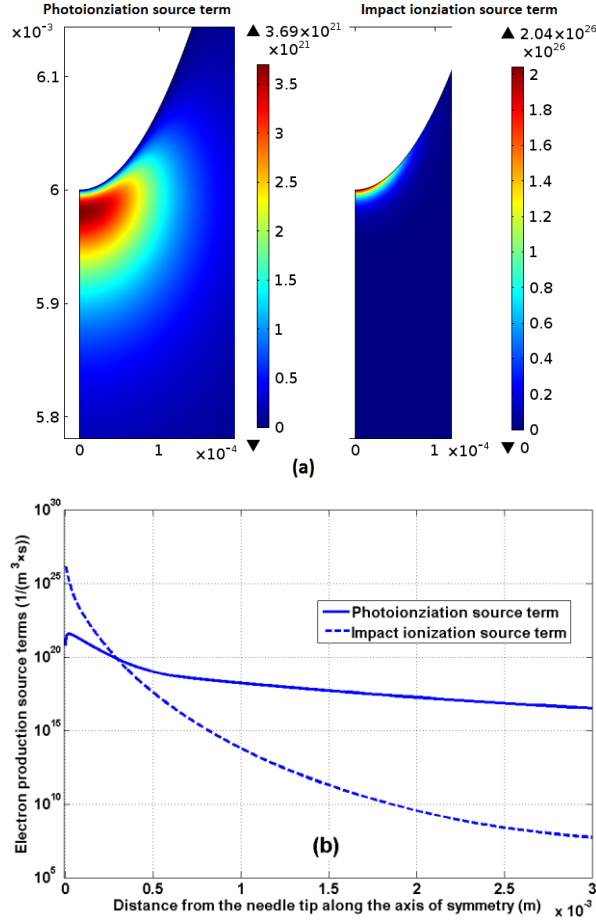
Figure 4-3: Distributions of photoionization and impact ionization source terms (m^{-3}s^{-1}) for the +4500 V corona discharge in the (a) area near the needle tip (horizontal and vertical axes are r and z cylindrical coordinates (m), respectively), and (b) along the axis of symmetry. The model consists of a 6 mm air gap and 35 μm tip radius.

One might wonder about the role of the background ambient electrons in the self-sustaining process of the positive corona discharge, generated, for example, by cosmic radiation, which is a valid argument in some cases. Pancheshnyi [79] discussed the importance of the presence of the background natural electrons in the propagation of the cathode-directed streamers. He suggested that the cosmic rays are the major source of the natural ionization and other sources, such as radioactive radiation, are negligible. Although the direct measurement of electron-ion pair production due to cosmic rays is very difficult, Pancheshnyi [79] suggests the value 10^6 m^{-3}s^{-1} could be used as the most probable number.

However, our simulations show that in the case of the corona discharges (both positive and negative polarities) the background ambient electrons don't play any role in the process of self-sustaining the discharge. The ambient electrons are required only for initiating the discharge and during the discharge, photoionization and impact ionization keep the positive corona discharge self-sustained.

In order to better quantify the effect of photoionization, the number of produced electrons due to photoionization and the impact ionization are compared with each other. The integrals IIS and IPS are defined as:

$$IIS = \iint_S 2\pi r \alpha n_e |\mu_e \vec{E}| dr dz \qquad\qquad (\,4\text{-}14\,)$$

$$IPS = \iint_S 2\pi r S_{ph} dr dz \qquad\qquad (\,4\text{-}15\,)$$

where S, r and z represent the 2D axisymmetric integration surface and cylindrical coordinates, respectively. Both source terms (impact ionization $\alpha n_e |\mu_e \vec{E}|$, and photoionization S_{ph}) are expressed in m^{-3}s^{-1}, so their integrals will be in 1/s. The positive discharge current, ratio of these two integrals (IIS/IPS), and the value of the IIS at the steady state current is shown in Figure 4-4. The first number on the arrow and the number in the brackets are the values of IIS and the ratio IIS/IPS, respectively. Comparison of the ratio IIS/IPS=566 with the orders of magnitude difference noticed in their peak values (Figure 4-3) is actually consistent with the discussions presented regarding the much larger area the photoionization electrons occupy in the air gap compared to the impact ionization electrons. It was also observed that varying the voltage level in the whole range of the carried out simulations (4 kV to 6 kV) doesn't cause a noticeable variation in the ratio IIS/IPS at the steady state current level. This could be justified by the linearity of the Helmholtz equation (Eq. 4-12). In fact, the ratio IIS/IPS is determined by the shape of the ionization region and since the positive discharge in stationary in terms of both spatial distribution and time variation, the ratio remains constant.
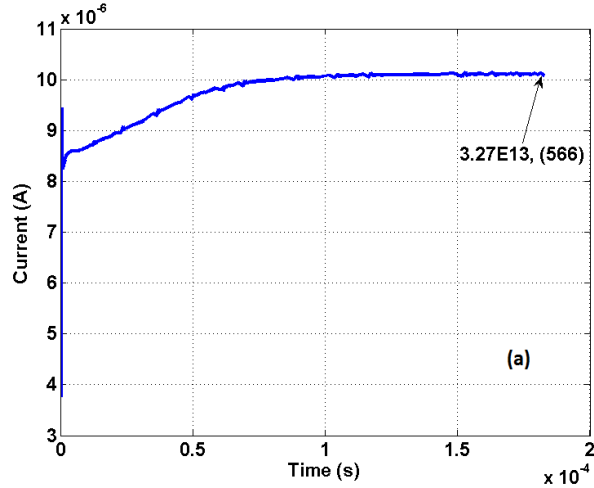
Figure 4-4: Calculated IIS and the ratio IIS/IPS at steady state in the +4500 V discharge. The first number on each arrow and the number inside the brackets are the values of IIS in (1/s) and the ratio IIS/IPS, respectively. The model consists of a 6 mm air gap and 35 µm tip radius.

4.5.2   Negative corona discharge

Studying the spatial distribution of the photoionization and impact ionization source terms for the negative corona discharge, as illustrated in Figure 4-5, shows that the peak location of the impact ionization electrons is a bit farther from the tip as compared to the positive corona discharge (Figure 4-3). In fact, the peak locations of the two sources are closer to each compared to the positive corona discharge and electrons from both sources travel approximately the same distance (have similar drift velocities) while being repelled in to a progressively smaller field. This point coupled with the fact that the peak values of two sources have orders of magnitude difference with each other justifies the minor role the existence of the photoionization in the negative corona discharge plays. Similarly, to the case of the positive discharge, it is observed in Figure 4-5 (b) that the photoionization electrons are distributed over a much larger area in the discharge volume than the impact ionization electrons.
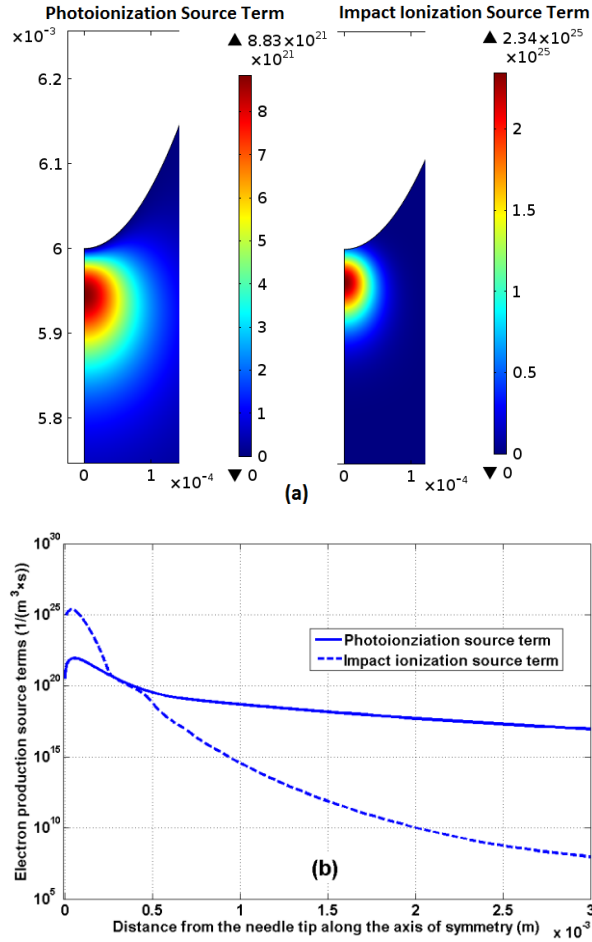
Figure 4-5: Distributions of photoionization and impact ionization source terms (m⁻³s⁻¹) for the -4500 V corona discharge in the (a) area near the needle tip (horizontal and vertical axes are r and z cylindrical coordinates (m), respectively), and (b) along the axis of symmetry. The model consists of a 6 mm air gap and 35 µm tip radius. Both plots are created at the inter-pulse instant of the discharge current.

Comparison of the total number of electrons produced from the two sources (impact ionization and photoionization) with the help of the ratio IIS/IPS at different stages of formation of the Trichel pulse is presented in Figure 4-6. It is observed that the number of electrons produced by the impact ionization is on average 100 times larger than those of photoionization (numbers inside the brackets in Figure 4-6 vary in the range of 70 to 123). This again confirms the minor role the existence of photoionization electrons plays in the discharge current.

Further inspecting the numbers given in Figure 4-6 reveals that at the peak point of a Trichel pulse, the domination of the impact ionization over the photoionization is the strongest. On the other hand, the effect of the photoionization is most pronounced on the rising edge of the current pulse. Conducting the same investigation for other voltage levels (from -3500 V to -5000 V) shows a very small variation in the numbers given in Figure 4-6, however, the general trend doesn't change. Comparing the IIS at different instants of the pulse shows that its value is constantly increasing on the rising edge of the pulse (from 2.81E14 (1/s) to 1.1E15 (1/s) at the peak point) and constantly decreasing to 1.19E13 (1/s) at the inter-pulse instant, during the falling side of the pulse. Since the impact ionization plays the major role in the formation of the pulse, the fact that the IIS has its largest value at the peak point of the pulse and smallest value at the inter-pulse instant is logical. However, the greater value of the ratio IIS/IPS at the falling side of the pulse compared to the rising side depicts that the photoionization process is more affected by the decrease of the electric field compared to the impact ionization.
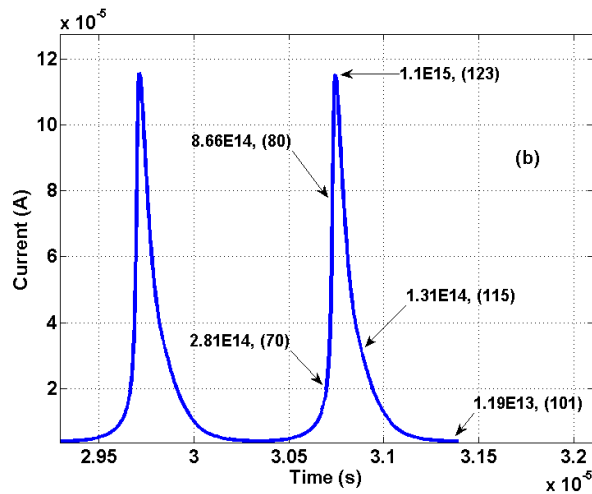
Figure 4-6: Calculated IIS and the ratio IIS/IPS for different instants of time in the -4500 V discharge. The first number on each arrow and the numbers inside the brackets are the values of IIS in (1/s) and the ratio IIS/IPS, respectively. All numbers for the first pulse are identical to those of the second one. The model consists of a 6 mm air gap and 35 μm tip radius.
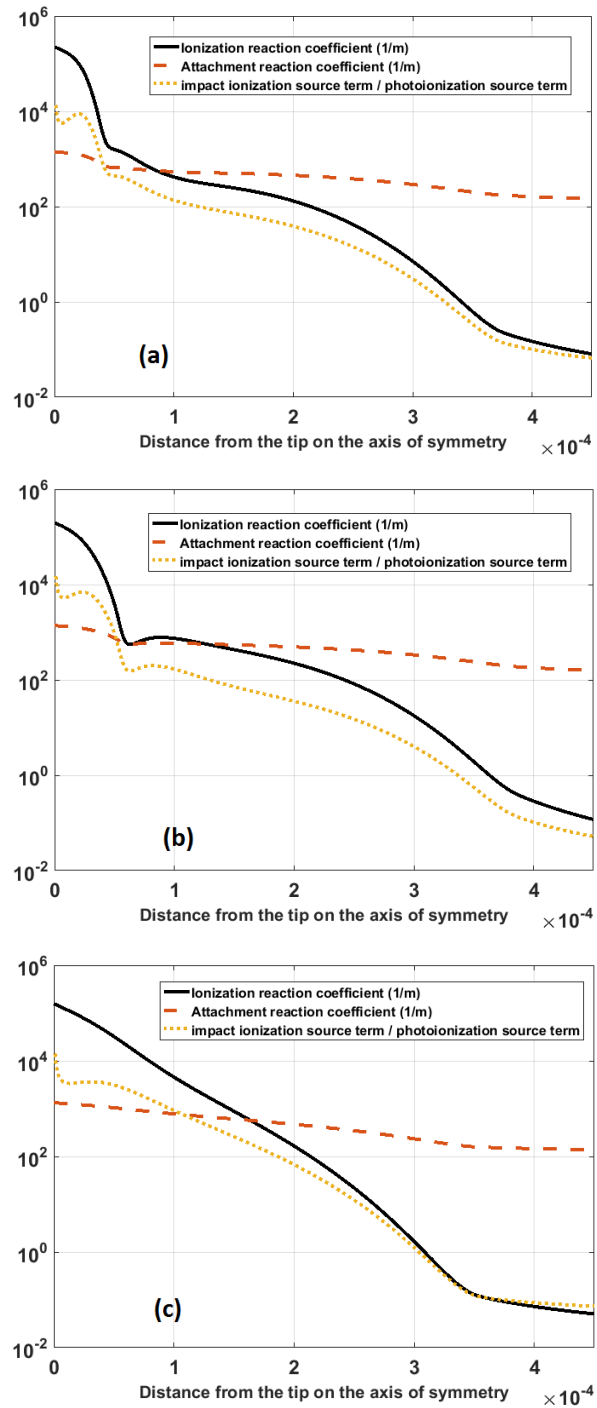
Figure 4-7: Comparison of the ionization reaction coefficient, attachment reaction coefficient, and the ratio *impact ionization source term / photoionization source term* **along the axis of symmetry at the time instants (a) right at the pulse peak, (b) the middle of the falling side of the pulse, and (c) the inter-pulse.**

Figure 4-7 presents the comparison of the ionization reaction coefficient, attachment reaction coefficient, and the ratio of *impact ionization source term / photoionization source term*. Figure 4-7 (a) to 1-7 (c) depict these values along the axis of symmetry at the time instants right at the pulse peak, at the middle of the falling side of the pulse, and at the inter-pulse time instant, respectively. The point where the ionization and attachment coefficients become equal could be compared to the ionization front in the negative streamers. The area behind this point is the ionization region, and the area ahead of this point is the drift region. Getting closer to the needle from this point (ionization region) will make the ionization coefficient greater than the attachment and going in the other direction (drift region) will make attachment coefficient predominant. It is well-known that in the negative streamers the mentioned ratio ahead of the ionization front should be much smaller than the area behind the ionization front. Similar observations can be noticed in Figure 4-7.

Comparison of the ratios IIS/IPS obtained for the positive and the negative discharges might seem misleading. Since the ratio for positive discharge was larger than the one for negative discharge, one might deduce that the photoionization in positive discharge plays a smaller role which is not correct. It should be noted that the ratio in each discharge is merely dependent on the shape of the ionization region and its distance from the needle which are stationary in the positive discharge and time-varying in the negative discharge. Hence, the ratios of the two discharges cannot be compared with each other.

It is well-known that the secondary emission of the electrons from the cathode surface due to the positive ion bombardment is the main mechanism for having a self-sustained negative corona Trichel pulses [55, 80]. Comparison of the number of the secondary electrons injected from the cathode surface with the number of electrons produced due to photoionization at different instants of formation of a Trichel pulse in the -4500V discharge is illustrated in Figure 4-8. The first number on each arrow is the frequency of the secondary emitted electrons (SEE) from the cathode surface in (1/s), and the second number in the bracket is the ratio SEE/IPS. Note the secondary emission coefficient (γ) used in [80], which was equal to 0.01, has been used here as well. The numbers in the Figure 4-8 depict that the SEE is less than the IPS on the rising edge of the pulse. This

could be justified by the fact that the secondary emitted electrons injected from the needle surface are the result of the bombardment of the needle by positive ions which move much slower than the photons which initiate the photoionization immediately. In other words, while the emitted photons from the excited nitrogen molecules immediately initiate the photoionization in the air gap, the positive ions which are the result of either impact ionization or photoionization are moving slowly towards the needle on the rising side of the pulse. After the positive ions have reached to the needle and the pulse began falling, the IPS becomes smaller than the SEE. Despite the fact that the SEE and the IPS have approximately the same values during the different stages of the Trichel pulse (Figure 4-8),
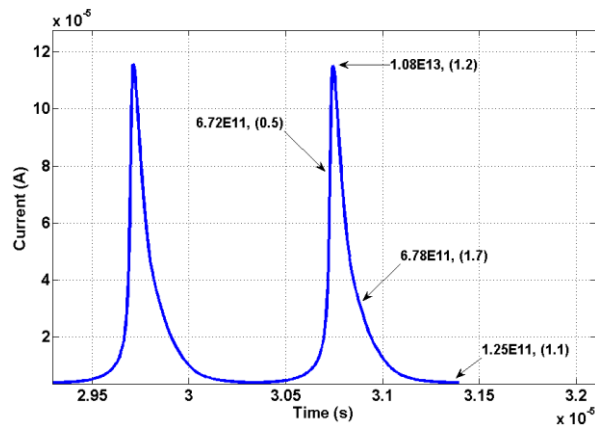
Figure 4-8: Comparison of the number of secondary emitted electrons (SEE) from the cathode with the number of electrons produced due to the photoionization. The first number on each arrow is the frequency of SEE in (1/s) and the second number in the brackets is the ratio SEE/IPS. All numbers for the second pulse are identical to those of the first one. The model here consists of a 6 mm air gap and 35 μm radius of the needle tip with -4500V applied on the needle.

since the secondary emitted electrons from the needle are produced in the area with very strong electric field, they have greater contribution (compared to the photoionization electrons) in the discharge current. It is important to notice that the discharge current is calculated by multiplying the density of the charged species with their drift velocities [80]. Comparing the numbers calculated in the Figs. 6 and 8, it is also concluded that the total number of electrons produced by impact ionization in the discharge volume is on average 100 times greater than those of secondary emitted electrons. In other words, a small number

61

of secondary emitted electrons is enough for sustaining the negative discharge, just like photoionization for sustaining the positive discharge.

4.6   Conclusions

A 2D-axisymmetric model for a quantitative study of the role of photoionization in the needle-plane positive corona discharge and also its impact on the characteristics of Trichel pulses in the negative corona discharge was presented in this Chapter. The three-term exponential approximation using three Helmholtz equations was applied for modeling the photoionization. The coefficients of the involved equations were validated by reproducing the experimental results of a positive corona discharge using a three-species, self-sustained model. The crucial role of the photoionization in sustaining the positive corona discharge is explained by studying the spatial distribution of the photoionization and impact ionization sources.

The presence of photoionization in the negative discharge model caused only slight variation (5% increase) in both the frequency and the DC current of the Trichel pulses. The insignificance of this impact was justified by calculating the ratio IIS/IPS at different stages of the formation of Trichel pulse along with studying the spatial distribution of the photoionization and impact ionization source terms. It was concluded, since the number of electrons produced by the impact ionization is on average 100 times larger than those of photoionization and the electrons produced by both sources travel approximately the same distance (undergo the same conditions of drift velocity) in the air gap, the incorporation of photoionization in the negative discharge model doesn't affect the discharge current significantly.

The number of secondary emitted electrons (SEE) from the cathode surface was also compared with the number of the electrons produced by photoionization (IPS) in the negative discharge. It was shown that the SEE had on average the same value as IPS. Moreover, it was concluded that the secondary emitted electrons in the negative discharge play a similar role as photoionization electrons in the positive discharge.

Chapter 5

5 « Parametric study of the characteristics of the Trichel pulses »

Since there are several sets of coefficients suggested in the literature for modeling the positive and negative corona discharge [82], it seems beneficial to understand the importance of these coefficients individually in terms of their impact on the characteristics of the pulses: the frequency, the DC current, and the rise time. The main goal of this Chapter is to conduct an investigation of the impact of the ionization reaction rate coefficient, attachment reaction rate coefficient, mobilities of charged species (electrons, positive ions, and negative ions), and the coefficient of the secondary emitted electrons from the needle, on the frequency, DC current, and the rise time of the Trichel pulses in the needle-plane negative corona discharge in atmospheric air. For this purpose, a base model was developed using the swarm parameters and the method previously discussed in Chapter 3 and the impact of variation of each of the abovementioned parameters individually on the characteristics of the pulses was investigated. The characteristics of the pulses were also studied using another set of model coefficients which includes an extended number of reactions such as detachment of the electrons from negative ions.

5.1   The numerical model

Similar to the model explained in Chapter 3, the base model presented in this chapter consists of three drift-diffusion equations governing the motion, generation, and recombination of the three charged species: electrons, positive ions, and negative ions. The distribution of the electric field is also calculated using Poisson's equation. There are four reaction coefficients contained in the base model: ionization $\alpha(1/m)$, attachment of the electrons to neutral molecules $\eta(1/m)$, recombination of positive and negative ions $k_{np}(m^3/s)$, and recombination of electrons and positive ions $k_{ep}(m^3/s)$. Equations included in the model are the ones explained in Chapter 3 (Eqs. 3-3 to 3-6).

Swarm parameters used in the base model are the ones listed in Table 3-2. Eqs. 3-3 to 3-6 were solved by the COMSOL Multiphysics package using the "transport of diluted

species" module for the drift-diffusion equations and the "electrostatics" module for Poisson's equation. A non-uniform triangular mesh consisting of 240,000 elements with the maximum element size of 1 µm near the needle tip was used. Linear and quadratic discretizations were used for the drift-diffusion and Poisson's equations, respectively.

The base model studied in this Chapter consists of a 3 cm long needle, which is placed perpendicularly 6 mm away from the ground plane. The needle is connected to -4500 [V] and the coefficient of the secondary emission of electrons from the needle is equal to 0.01, as suggested in Chapter 3. The boundary conditions for the included equations are also the same as the ones described in Chapter 3.

5.2 Parametric study

This section presents the results of the parametric study of the impact of variation of the ionization reaction coefficient α, attachment reaction coefficient η, electron mobility μ_e, positive ion mobility μ_p, negative ion mobility μ_n and the coefficient of the secondary electrons emitted from the needle γ on the frequency, DC current and the rise time of the pulses. Moreover, the impact of the existence of the recombination of positive and negative ions k_{np} and the recombination of electrons and positive ions k_{ep} was studied by excluding these reactions from the base model.

5.2.1 Coefficients of the ionization reaction α and the attachment reaction η

The impact of varying the ionization and the attachment reactions' coefficients in the range of ±10% on the frequency, DC current and the rise time of the pulses are shown in Figure 5-1. It is observed that the frequency of the pulses increases as a result of increasing any of the coefficients of these reactions and it is more sensitive to the variation of the ionization coefficient, compared to the attachment coefficient. According to the simulation results, it is also evident that the ionization reaction coefficient not only plays an important role in the characteristics of the obtained pulses, but it also affects the convergence of the model, even when increased by as little as 5%. The solver is forced to take smaller time steps when the ionization coefficient is increased. On the other hand, the DC current was
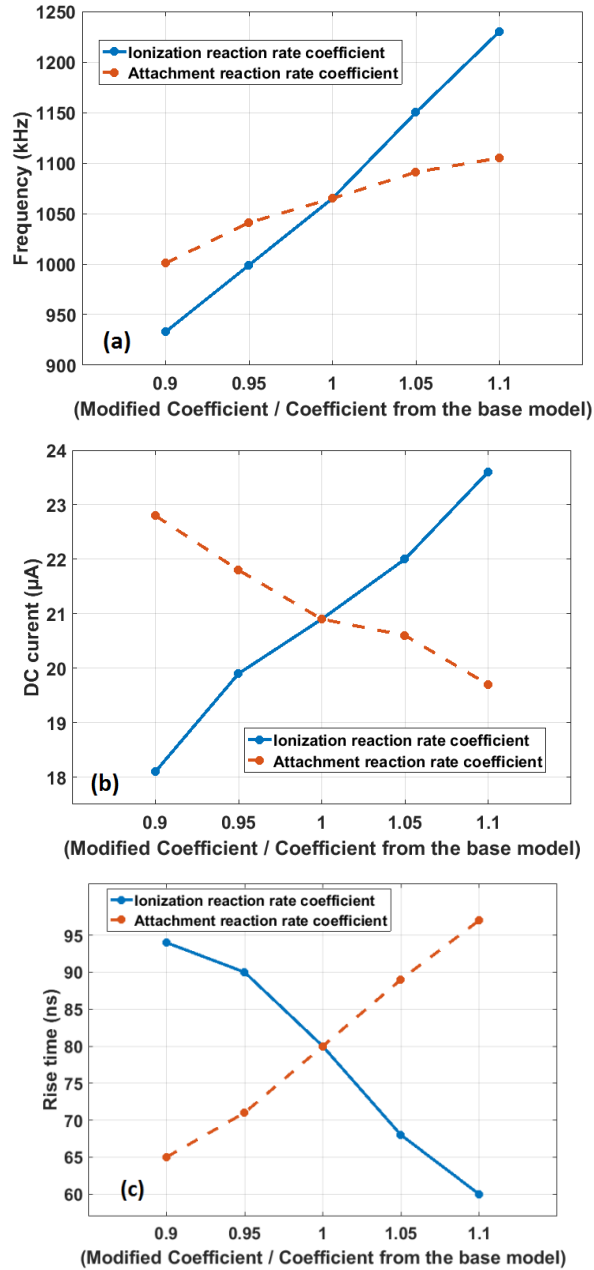
Figure 5-1: The sensitivity of (a) the frequency, (b) the DC current, and (c) the rise time of the pulses to the variations of the coefficients of the ionization and attachment reactions.

found to be proportional and inversely proportional to the ionization coefficient and attachment coefficient, respectively. Like the frequency, the variation range of the DC current is greater when the ionization coefficient is varied compared to the case where the attachment coefficient is varied. It is also observed that increasing the ionization coefficient

results in a shorter rise time for the pulses. The attachment coefficient has opposite effect on the rise time. The rise time seems to be equally sensitive to the variations in the coefficients α and η.

To understand the relation between the frequency and the DC current of the pulses, and the ionization coefficient, one should recall the basic concept of the formation of the Trichel pulse. The accumulation of positive ions near the tip due to the ionization enhances the electric field between the cloud of positive ions and the tip. On the other hand, the accumulation of the negative ions in the farther region reduces the electric field in the whole region between the cloud of negative ions and the tip. The higher the ionization coefficient, the harder it is for the negative ions to diminish the electric field and the higher the amplitude of the pulses will be. On the other hand, since the formation of the next pulse depends on the re-accumulation of positive ions near the tip after the negative ions have moved far enough, the higher ionization coefficient will lead to the faster formation of the next pulse, and, hence, higher frequency. It is obvious that the shorter time between the pulses along with the higher pulse amplitude results in higher DC current.
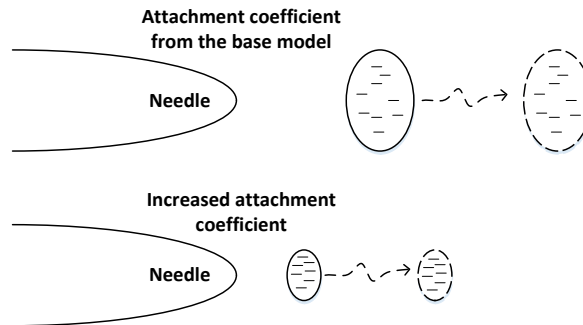
Figure 5-2: Schematic representation of the impact of the attachment coefficient on the formation of the cloud of the negative ions near the tip. Smaller ovals in the bottom figure correspond to a smaller net charge.

A schematic representation of the impact of the attachment coefficient on the formation of the cloud of the negative ions is shown in Figure 5-2. As the attachment coefficient increases, the volume in which the attachment reaction predominates over the ionization reaction becomes closer to the needle tip. Therefore, the cloud of negative ions will form in the area closer to the tip. This means that the diminishing of the electric field near the

tip will be completed faster with a smaller number of negative ions. Hence, the amplitude of the pulses will become smaller. On the other hand, since the negative ions in the model with an increased attachment coefficient are in the area with the stronger electric field, they will move faster away from the tip, hence the electric field near the tip will recover faster and the process of the formation of the next pulse will begin sooner. It should be noted that the DC current is a function not only of the frequency but also the shape of the pulses (amplitude, rise time, fall time, and pulse width) and the resulting DC current is the combined effect of the variations in all these parameters. Although in this case, the increased frequency and the decreased amplitude contradict each other for determining whether the DC current should increase or decrease, it seems that the decreasing factors have a stronger impact.

The impact of the ionization and attachment coefficients on the rise time of the pulses could be studied in the light of the role the avalanche ionization plays in forming the rising side of the pulse. The higher rate of the avalanche ionization process, the sharper the rising side of the pulse. Since increasing the attachment coefficient enhances the rate of dissipation of electrons, it will decrease the rate of the avalanche ionization and, hence, lengthen the rise time of the pulse.

5.2.2 Electron mobility μ_e

Two modified models using different constant values for the electron mobilities have been studied. Comparison of these two constant electron mobilities with the mobility of the electrons assumed in the base model, which is a function of the electric field, is presented in Figure 5-3.

The results for the Trichel pulse characteristics for three different electron mobilities are given in Table 5-1. It is observed that increasing the constant μ_e decreases the frequency of the pulses although it is interesting to note that each is significantly larger than that found in the base model. The reason of this variation is not completely clear but one might refer to the Thomson formula and suspect that the electron energy in this variation range is in the range where the cross section of the ionization reaction is inversely proportional to the

electron energy [83]. Since the electron energy is proportional to the electron velocity, the increased mobility could cause the same effect as decreasing the ionization coefficient.
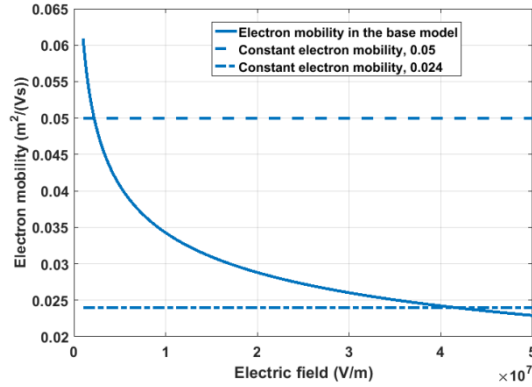
Figure 5-3: Comparison of the two constant electron mobilities with the mobility considered in the base model

Table 5-1: Simulation results for the base model and two modified models assuming constant electron mobilities

Electron mobility ($m^2/(Vs)$), $\vec{E}$ in (V/m)	Frequency of the pulses (kHz)	DC current of the pulses (μA)	Pulse rise time (ns)
$1.9163 \times \left\|\vec{E}\right\|^{-0.25}$ [1]	1065	20.9	80
0.024	1244	21.1	N.A.[1]
0.05	1210	20.7	160

5.2.3   Mobilities of positive ions μ_p and negative ions μ_n

Variations of the frequency, DC current, and the rise time with the variations of the mobilities of positive and negative ions by ± 10% are shown in Figure 5-4. It is observed that the frequency is proportional to the mobilities of both the positive and the negative ions. However, it is more sensitive to the variations of the mobility of the negative ions than to the mobility of the positive ions. While the DC current is increasing with the increased μ_n, it does not change with the variations of μ_p. On the other hand, the rise time seems to be fairly independent of the mobility of positive ions and inversely proportional to the mobility of the positive ions. In other words, the faster the positive ions, the faster

---

[1] The rise time of the pulse is defined as the time between 10% of the peak to the 90% of the peak. In this case the current does not drop to the 10% level.
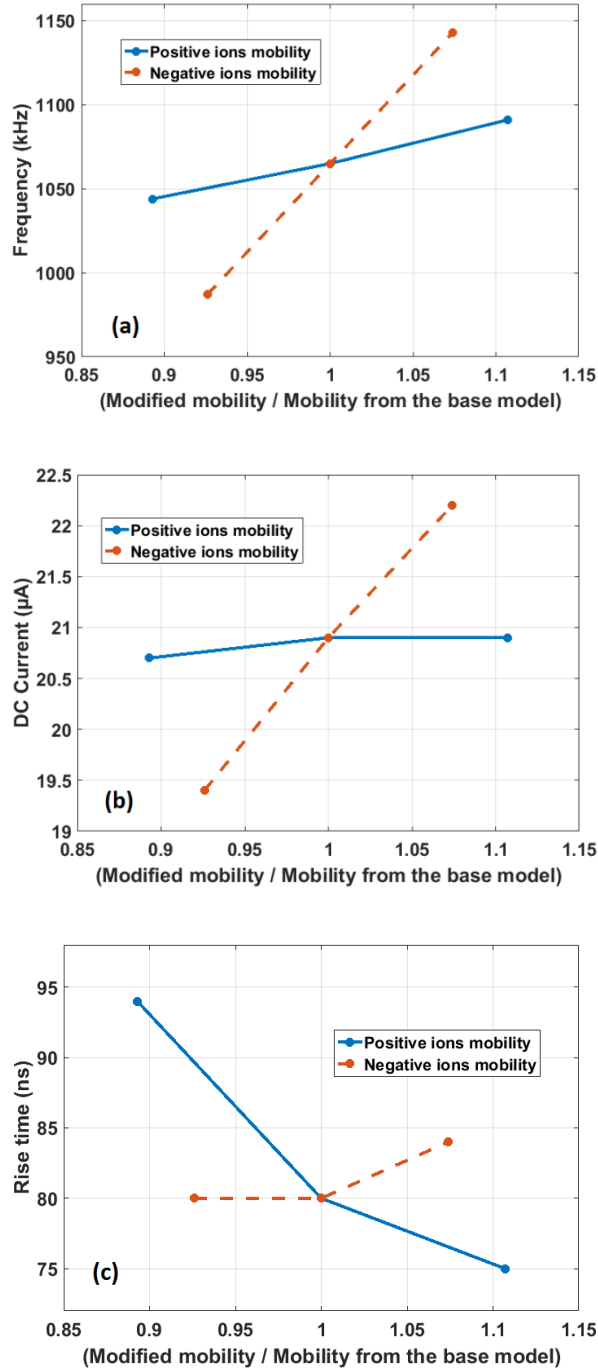
Figure 5-4: Variations of (a) the frequency, (b) DC current, and (c) the rise time with the mobilities of positive and negative ions.

the rise time of the pulse will be. Sattari et al. [55] had found earlier in their numerical model that increasing the mobilities of positive and negative ions together will lead to a

higher frequency and DC current. It should be noted though, that in the present study, these mobilities are varied individually, while all other parameters are kept constant.

Variation of the frequency with the mobility of positive ions could be explained by the fact that with the higher mobilities, during the process of preparing the air gap for the next pulse, positive ions will deposit faster on the needle leading to faster injection of the secondary electrons to the air gap, and, hence, consecutive pulses will come at a higher frequency. This explanation is schematically shown in Figure 5-5.

The effect of the mobility of the positive ions on the rise time of the pulses could also be explained using Figure 5-5. The higher the rate of the deposition of positive ions on the needle, the higher the rate of injection of the secondary electrons from the needle. This will lead to the enhancement of the avalanche ionization on the rising side of the pulse which makes the pulse sharper. It is evident that the negative ions play no role in the process of building the rising side of the pulse. So, it is not surprising to find out that the rise time of the pulse does not change with varying the mobility of negative ions.
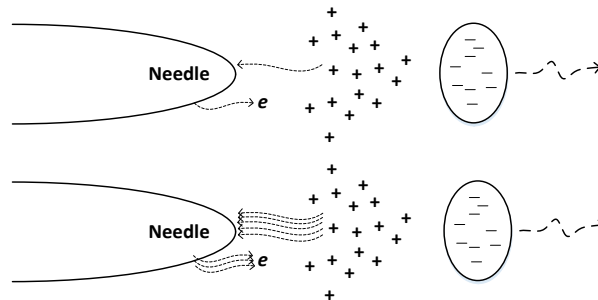
Figure 5-5: The impact of the increased mobility of positive ions. Faster deposition of positive ions on the needle will lead to the faster injection of secondary electrons from the needle surface.

The increasing frequency, as the mobility of negative ions is increased, could be justified by the role the negative ions play in the process of diminishing the electric field at the pulse peak and the fact that the electric field near the tip won't reach the threshold for avalanche ionization unless the negative ions are repelled far enough from the needle. The faster the negative ions move away from the needle after the electric field is diminished, the sooner
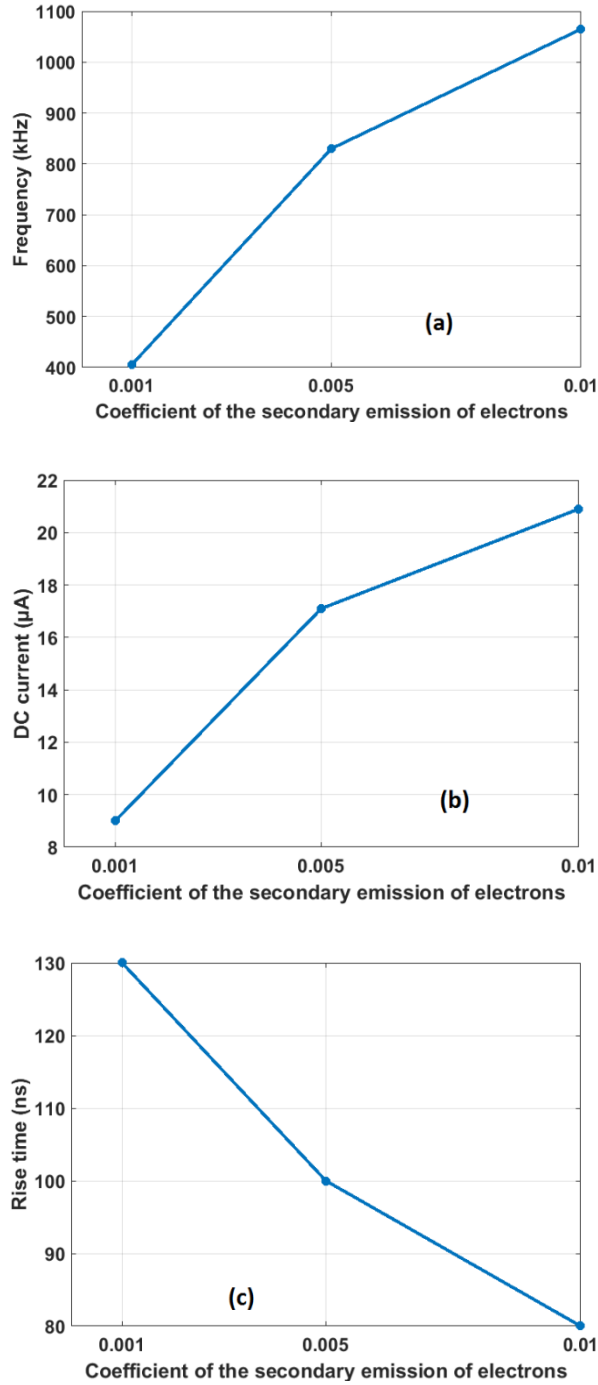
Figure 5-6: Variations of (a) the frequency, (b) DC current, and (c) the rise time with the coefficient of the secondary emission of the electrons

the electric field will reach the threshold for triggering the next avalanche ionization. Hence, the frequency will increase.

5.2.4 Coefficient of the secondary electrons emitted from the needle γ

Variations of the frequency, DC current and the rise time with the coefficient of the secondary emission of the electrons are shown in Figure 5-6. As this parameter is the subject of considerable variation in the literature, here it is varied over a range of an order of magnitude. It is observed that the higher coefficient γ results in higher frequency, higher DC current, and faster-rising pulse. These findings are not surprising in the sense that the higher the rate of the injection of the secondary electrons from the needle, the faster the avalanche ionization will be triggered. Moreover, DC current will also increase as the result of increasing the number of electrons in the area of the strong electric field, which will lead to a higher concentration of positive ions on the tip. It should be noted here that these findings contradict the findings reported earlier by Sattari et al. [55], who found that the frequency and the DC current don't change drastically by varying the coefficient of the secondary emission of electrons.

5.2.5 Existence of k_{np} and k_{ep}

The simulations showed that removing the recombination of positive and negative ions, and recombination of electrons and positive ions from the numerical model doesn't change the characteristics of the Trichel pulses as compared to the base model including all four reactions. The obtained frequency and the DC current for the modified base model excluding k_{np} and k_{ep} are 1048 kHz and 21 µA, respectively.

5.3 New model with an extended number of reactions

There are numerous sets of coefficients suggested in the literature for modeling atmospheric pressure discharges [82, 84]. The coefficients used in [84] are used here for finding the characteristics of Trichel pulses in the same geometry as the one used in the previous part (the air gap of 6 mm and a needle length of 3 cm). Soloviev et al. [84] have suggested a model with an extended number of reactions for modeling a surface dielectric

barrier discharge (SDBD) in atmospheric air. The reactions and coefficients included in this model are summarized in Table 5-2.

Table 5-2: Summary of the reactions and the coefficients included in the new model with an extended number of reactions [84]. The parameter (E/N) is the reduced electric field in units of 10^{20} Vm^2, k_B is the Boltzmann constant, and e is the unit charge.

Reaction / Parameter	Reaction rate coefficient / Parameter's value	Unit
Ionization e + N$_2$(O$_2$) → 2e + N$_2$$^+$(O$_2$$^+$)	$k_i = 10^{-6} \times (0.7668 + 0.018 \, (E/N)) \, 10^{-7.95-38.22/(E/N)}$	m^{3}s^{-1}
Dissociative electron-ion recombination e + O$_2$$^+$ → O + O	$k_{dr1} = 2 \times 10^{-13} \left(\frac{300}{T_e}\right)^{0.7}$	m^{3}s^{-1}
Dissociative electron-ion recombination e + O$_4$$^+$ → O$_2$ + O$_2$	$k_{dr2} = 1.4 \times 10^{-12} \left(\frac{300}{T_e}\right)^{0.5}$	m^{3}s^{-1}
Electron attachment e + O$_2$ → O^{--} + O	$k_{att} = 10^{-6} \times 10^{-10.21-5.7/(E/N)}$	m^{3}s^{-1}
Electron detachment O^{--} + N$_2$ → e +N$_2$O	$k_{dt} = 9.2 \times 10^{-19}$	m^{3}s^{-1}
Ion-ion recombination A$^+$ + B^{--} + (M) → A + B + M (M= N$_2$, O$_2$)	$k_r = 2 \times 10^{-12} \left(\frac{300}{T_i}\right)^{1.5}$	m^{3}s^{-1}
Electron temperature T$_e$	$\begin{cases} T_a + 8645(E/N)^{0.54069} & (E/N) < 1 \\ T_a + 8645(E/N)^{0.4} & (E/N) > 1 \end{cases}$	K
Electron mobility μ$_e$	$\begin{cases} 0.0866 & (E/N) < 1 \\ 0.0383 \times \left(1 + \dfrac{1.262}{(E/N)}\right) & 1 < (E/N) < 20 \\ 0.0275 \times \left(1 + 9.6/(E/N)\right) & (E/N) > 201 \end{cases}$	m^{2}V^{-1}s^{-1}
Electron diffusion D$_e$	$\dfrac{k_B T_e \mu_e}{e}$	m^{2}s^{-1}
Mobility of negative ions μ$_n$	3.2×10^{-4}	m^{2}V^{-1}s^{-1}
Effective mobility of positive ions μ$_p$	2.1×10^{-4}	m^{2}V^{-1}s^{-1}
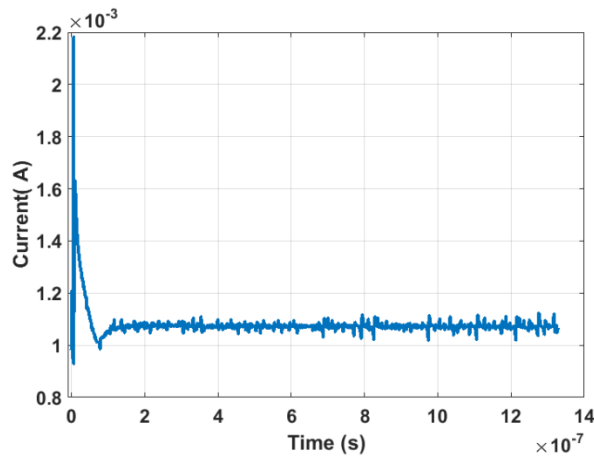
Figure 5-7: Discharge current with the 6 mm air gap needle-plane geometry and the coefficients suggested in [84]. The coefficient of the secondary emission of the electrons is assumed γ=0.01.

Applying the reactions and the coefficients summarized in Table 5-2 to the above-mentioned geometry, it was observed that the discharge reaches a steady-state condition in which the pulses disappear (Figure 5-7). It was found that excluding the detachment reaction (k_{dt}) brings back the pulsation mode of the current. It seems that in the presence of the detachment reaction, negative ions couldn't stay in the air gap to play their vital role in the formation of the pulses. Excluding the detachment reaction and assuming the coefficient of the secondary emission of electrons $\gamma = 0.001$ leads to a frequency and DC current of 2280 kHz, and 21.7 µA, respectively. The obtained frequency here is much higher than the one obtained in the model based on the coefficients suggested in [1]. If the coefficient of the ionization reaction is reduced 30% (the k_i is multiplied by a factor of 0.7) and $\gamma = 0.001$, the numbers will drop to 1587 kHz, and 16.3 µA. One of the possible reasons that the frequencies obtained from the discharges based on Table 5-2 is much higher than the ones obtained from the discharges based on Table 3-2 could be the mobility of negative ions which is higher in Table 5-2.

5.4   Conclusions

A 2D axisymmetric model for studying the impact of the numerical coefficients on the characteristics of the Trichel pulses in a negative needle-plane corona discharge was presented in this Chapter. The studied parameters were: ionization and attachment reaction coefficients, mobilities of electrons, positive and negative ions, and the coefficient of the secondary emission of the electrons. Following conclusions can be made from the results of the numerical models:

- Increasing the ionization coefficient or the coefficient of the secondary emission of the electrons increases the frequency and the DC current and also decreases the rise time.
- Increasing the attachment coefficient increases the frequency and rise time, and also decreases the DC current. It was observed that the frequency was more sensitive to the variation of the ionization coefficient compared to the variation of the attachment coefficient.
- Increasing the constant electron mobility decreases the frequency of the pulses.

- The frequency and the DC current increase, if the negative ion mobility is increased. The rise time of the pulse seems to be independent of μ_n. On the other hand, DC current does not change with the positive ion mobility.

- The existence of the reactions k_{ep} and k_{np} does not impact the characteristics of the Trichel pulses.

The detachment reaction, present in the set of the coefficients used by Soloviev et al. [84], causes the pulsation mode of the discharge to disappear. It was also found that the frequencies obtained using these coefficients were much higher than the expected values.

Chapter 6

6 « Experimental study of the characteristics of Trichel pulses »

The results of an experimental study of the negative corona discharge in a needle-plane geometry are reported in this Chapter. The experiments were conducted in air at room temperature, relative humidity, and atmospheric pressure. The impact of different parameters: the needle voltage, needle-plane distance, and the radius of curvature of the needle's tip on the frequency, DC current, and the temporal characteristics of the pulses (rise time, fall time and the pulse width) was studied. Four different needles with radii of curvatures ranging from 19 µm to 55 µm were used. The needle-plane distance was varied from 6 mm to 3 cm. The applied voltage on the needle was varied from the onset voltage (-4 kV to -6 kV) to -10 kV. It was observed that the temporal characteristics of the pulses, such as rise time, were not a function of the radius of the curvature of the needle's tip, voltage level, or the needle-plane distance. The experimental data were compared with the results of a series of numerical simulations as well as the experimental data published by Lama and Gallo. The experimental findings were found to be in a good agreement with Lama's and Gallo's work. Several discrepancies were found between the numerical and experimental results and possible reasons for those are discussed.

Li et al. [85] have conducted a series of experiments studying the variation of the frequency and the DC current of Trichel pulses in a needle-plane gap of 4 cm to 5.5 cm. For calculating the frequency of the pulses, they suggested an empirical formula based on the average electric field intensity and the corona onset field intensity instead of the applied voltage and the corona onset voltage. It is true that the impact of needle-plane distance and the radius of the tip were taken into account by using this method, however, due to the fact that the average electric field is calculated with the numerical solution rather than experimental measurement, it would be practically difficult to use the formula. Although in this work the authors found that the temporal characteristics of the pulses are independent of the varied parameters, they weren't able to measure the rise time, fall time,

or the pulse width. Later, they conducted a similar study for much longer gaps ranging from 10 cm to 50 cm [86].

Recently, Zhang et al. [87] conducted experimental studies of the Trichel pulses in a needle-plane discharge with a 5 mm air gap. They reported a linear variation for the rise time of the pulses as a function of the radius of the tip of the needle.

The main goal of this Chapter is to present the results of an experimental study of the effect of corona voltage, gap distance and tip radius on the characteristics of the Trichel pulses formed in a negative DC corona discharge in a needle-plane geometry. The measured characteristics were: the frequency of the pulses, DC current, rise time, fall time and the pulse width. In addition, the experimental results were compared with the numerical predictions which were obtained from the model reported previously [1]. The experiments consisted of four needles with the radii of curvature ranging from 19 µm to 55 µm. The distance between the needle and the plane was varied from 1 cm to 3 cm. The experiments were also conducted for a 6 mm air gap to compare the obtained frequency and the DC current with the findings reported in the work of Lama and Gallo [37].

6.1   Experiments

The following describes the equipment, procedure and the results of the conducted experiments for studying the characteristics of the Trichel pulses generated in the negative DC corona discharge in a needle-plane geometry.

6.1.1   Equipment

The various elements used in the experiments were as follows. The corona electrodes comprised of four nickel coated steel needles with different radii of curvatures ranging from 19 µm to 55 µm, each having a length of 4 cm. The radii of curvatures were measured using a Leica 6S D microscope. The tips were found to be not perfectly spherical so the radii were estimated using a best fit hemispherical template superimposed over the image of the tip. Individual needles were mounted above a square shaped metallic ground plane with 30 cm sides, using an insulated copper cylindrical mount which was connected to the HV cable on one side and held the needle on the other side (Figure 6-1). The system was

energized using a HV negative 0-15 kV DC supply and the needle voltage was measured using a Fluke 80k-40 HV probe connected to a Tektronix CDM 250 digital multimeter. The corona current was detected by measuring the voltage drop across a 1 kΩ high precision foil resistor in series with the ground plate using a Tektronix TDS 2024 oscilloscope (200 MHz and 2GS/s). In order to minimize ambient noise, the experimental apparatus was enclosed in a metallic cage with grounded walls. The oscilloscope probe was also shielded with a grounded aluminum foil. A schematic of the experiment setup is shown in Figure 6-2.
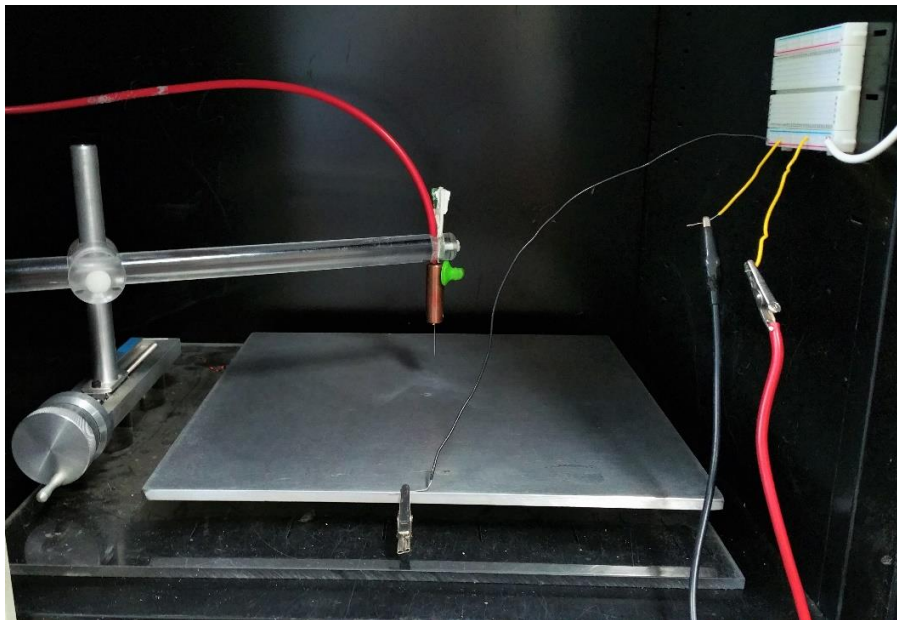
Figure 6-1: A view of the needle-plane setup
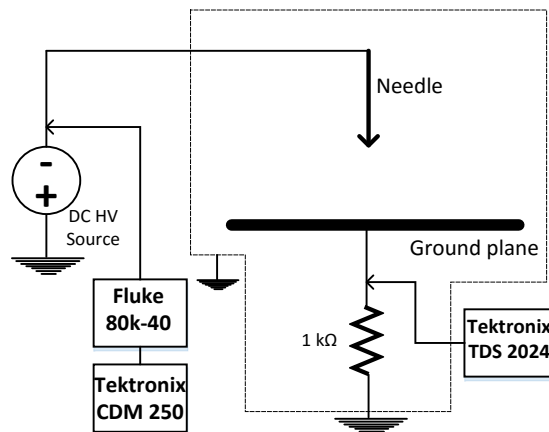
Figure 6-2: Schematic of the experiment setup

6.1.2   Procedure

The onset voltage for each needle was determined by starting from a very low voltage (-2 kV) and noting the voltage at which the pulses first appeared on the oscilloscope screen. On the other hand, it was found that -10 kV was a safe upper limit for all experiments to avoid sparking. So, the experiments were conducted between the onset voltage (which varies between -4 kV and -6 kV) and -10 kV. Although the measured corona onset voltages were generally slightly higher than the results of Peek's formula, they were in an acceptable agreement.

In order to measure the frequency of the pulses for a specific configuration, during each experiment, the average of the frequencies of 8 to 12 sets of pulses, each containing 6-10 pulses (depending on the frequency and the number of pulses which could fit on the oscilloscope's screen) were recorded. Typically, 4 to 6 experiments were conducted for each configuration thus giving an average total sample of approximately 400 pulses for each configuration. The average and the range of variation of these results were recorded on the graphs. It was found that during each experiment, after a short time (as short as 30 seconds in the higher voltage range), the frequency of the pulses started increasing. It was believed that this was due to the formation of local hot spots on the tip of the needle. This was confirmed by repeating a series of tests and showing that the initial pulse trains were reproducible. In order to avoid measuring unrealistic high frequencies, the recording of the train of pulses was carried out as quickly as possible. This increasing trend was also noticeable for the DC current, but with much slower rate.

The measurements of the frequencies in all the experiments were done by analyzing the recorded waveforms using MATLAB software after transferring them from the oscilloscope. However, for measuring the DC currents, an analog electrodynamic microammeter was used in the circuit after removing the 1 kΩ current-measuring resistor. In most of the cases the DC current reading of the oscilloscope using the resistor was in good agreement with the reading of the analog ammeter for the same experiment, but since the oscilloscope was more sensitive to ambient noise, the analog ammeter was more convenient than the oscilloscope. Since putting the analog microammeter and the 1 kΩ

resistor in the circuit together led to unrealistic large rise times for the pulses and also increased the level of noise, the measurements of frequency and the DC current had to be done separately. For the temporal characteristics of the pulses: rise time, fall time and the pulse width, we trusted the numbers given by the oscilloscope.

6.1.3   Results

A snapshot of a typical train of current pulses and closer view on a single pulse observed on the oscilloscope's screen during the experiments is shown in Figure 6-3.
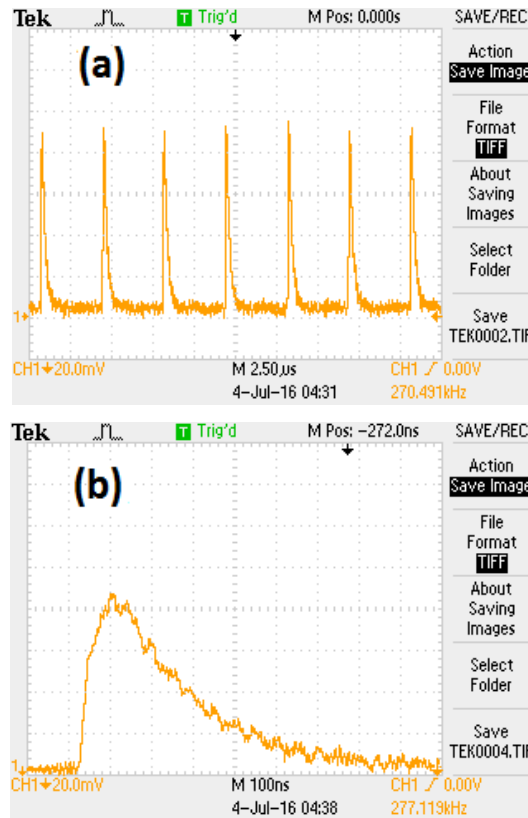
Figure 6-3: Snapshot of a typical set of Trichel pulses observed on the oscilloscope's screen (a) view of several pulses, (b) view of a single pulse. Applied voltage, the needle-plane distance, and the radius of the curvature were -10 kV, 3 cm, and 19 μm, respectively.

Variations of the frequency and the DC current with the applied negative voltage on the needle with a constant needle-plane distance of 2 cm are shown in Figure 6-4. It is observed that the variation of the frequency is larger than the variation of the DC current at the same

voltage level. This difference is more noticeable in the higher voltage range. This finding is consistent with the similar plots reported by Lama and Gallo [37].
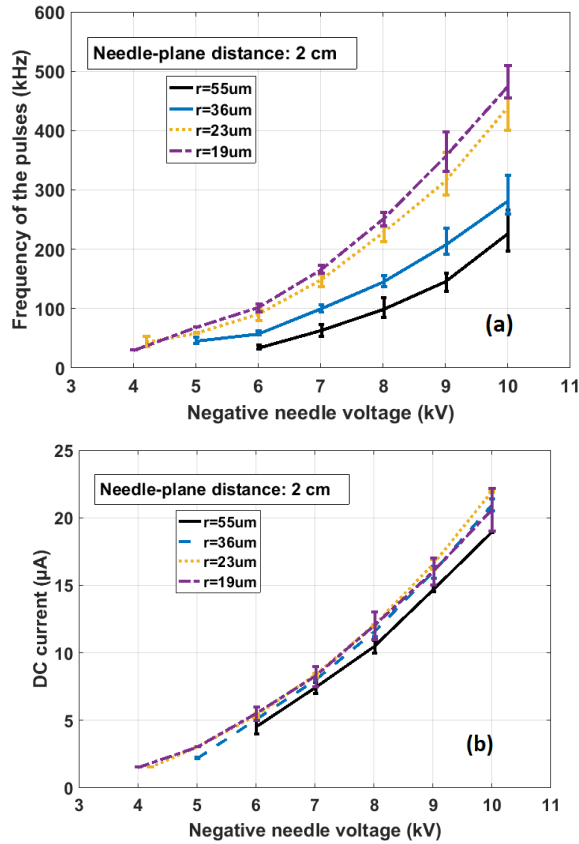
Figure 6-4: Variations of the (a) frequency of the pulses and (b) DC current with the applied negative voltage on the needle with a constant needle-plane distance of 2 cm. The range of the applied voltage for each needle starts from the onset voltage.

Variations of the frequency and the DC current with the needle-plane distance assuming a constant applied voltage of -10 kV are shown in Figure 6-5. Since the discharge gets closer to the spark regime as the air gap gets smaller, it is observed that the rate of increase of the DC current and frequency gets larger as the air gap decreases. On the other hand, increasing the needle-plane distance to the gaps larger than 2 cm doesn't change the frequency and the DC current significantly, assuming that the voltage is kept constant.
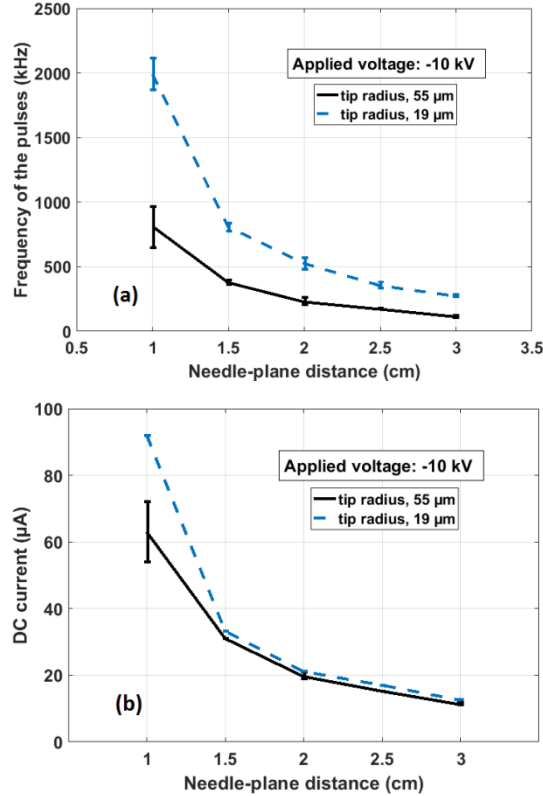
Figure 6-5: Variations of the (a) frequency of the pulses and (b) DC current with the needle-plane distance at a constant voltage applied to the needle of -10 kV.

Comparisons of the measurements of the frequency and the DC current with the findings of Lama and Gallo [37] for the closest needle tip are shown in Figure 6-6. It is observed that the agreement for the DC current is much better compared to the frequency of the pulses. Some uncertainties in the measurements of the radii of the curvatures might be the reason for the discrepancies. However, it is not surprising to notice that a larger radius of curvature leads to a smaller frequency for the pulses.

The results from all the experiments led to the average of 49 ns, 445 ns, and 220 ns for the rise time (10% to 90% of the peak), fall time (90% to 10% of the peak), and the pulse width (50% to 50% of the peak), respectively, with a standard deviation of less than 5%. Investigating these temporal characteristics led to the conclusion that these numbers don't change significantly by varying the voltage applied on the needle up to -10 kV, needle-plane distance from 6 mm to 3 cm or the radius of the tip of the needle from 19 µm to 55 µm. Although Li et al. [85] have not reported the rise time, fall time, or the pulse width of

the pulses, their findings led them to the conclusion that the rise time of Trichel pulse was not a function of the voltage, air gap, or the tip radius. In contrast, Zhang et al. [87] claimed that their findings show a linear proportionality between the rise time of the pulse and the radius of the tip of the needle. They reported that the rise time increases linearly from 15 ns to 95 ns while the radius of the tip of the needle varies from 50 µm to 350 µm. This observation not supported by the results presented here albeit it should be noted that the radii of needle tips used here are all less than 55 µm.
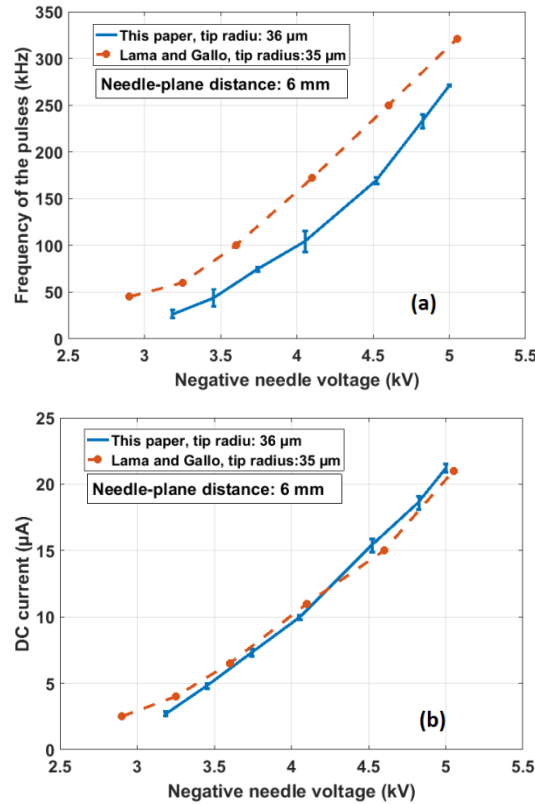
Figure 6-6: Comparison of the experimental results with the findings of Lama and Gallo [37].

We believe that the fact the temporal characteristics of Trichel pulses don't change with varying the macroscopic parameters (needle voltage, air gap, and tip radius) shouldn't be surprising. In fact, the rise time which is the time period between the point that the electric field exceeds the onset value and the point which the electric field gets quenched by the cloud of negative ions is primarily dependent on natural properties of the molecules with which the electrons are interacting (for air, oxygen is the main electronegative gas).

6.2 Comparison of the numerical model's results with the results of the experiments

In this Section, the results of the numerical simulations based on the model previously suggested by the authors [1] for the negative DC corona discharge in a needle-plane geometry are compared with the results of the conducted experiments.

6.2.1 Description of the numerical model

In a short summary, the numerical model described previously in Chapter 3 which consists of three drift-diffusion equations modeling the motion, generation and recombination of the three charged species: electrons, positive ions, and negative ions is used here. The configurations of the time-dependent solver and the mesh are the same as the ones used in Chapter 3 and the base model of Chapter 5.

It is well established in the literature that the negative corona discharge is a self-sustained discharge and mechanism behind this self-sustaining is the injection of the secondary electrons from the needle surface as a result of the bombardment of the needle surface with positive ions. There is no solid agreement among the authors over the value of the coefficient of the secondary emitted electrons from the needle, γ. The simulations show that the frequency of the pulses, DC current and the temporal characteristics of the pulses are strongly dependent on in the value of this coefficient. Although suggested values for γ in the literature vary in the range of 0.001 to 0.05 [1, 55, 88], we compared the results of the numerical models with γ ranging from 0.0005 to 0.01.

6.2.2 Comparison of the results

Trichel pulses obtained from the numerical model with -7 kV applied voltage on the needle, 36 µm radius of the tip of the needle, γ=0.001 and 2 cm needle-plane distance are shown in Figure 6-7.
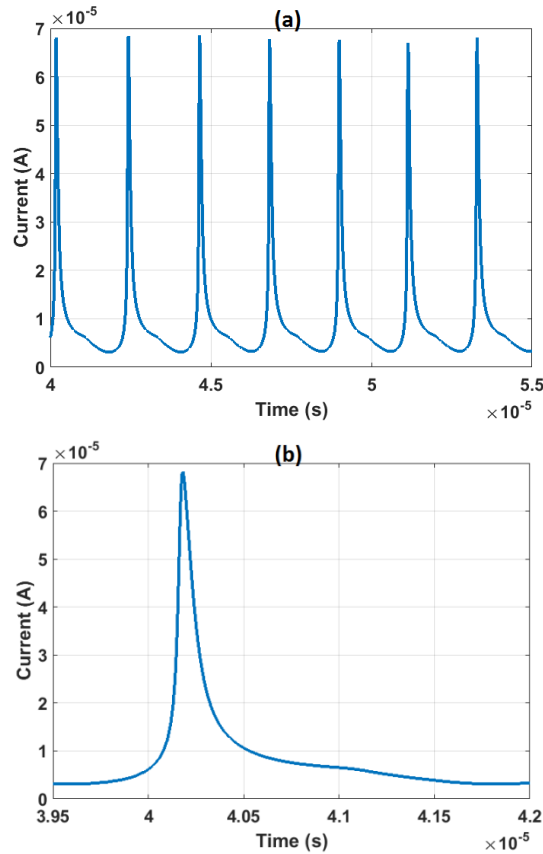
Figure 6-7: Representation of (a) the series of pulses and (b) single pulse obtained from the numerical model with the coefficients given in Table 3-2, γ=0.001, applied needle voltage of -7 kV, radius of the tip of the needle of 35µm and the needle-plane distance of 2 cm.

Comparison of the results of the numerical models with different values for γ and the experimental measurements is summarized in Table 6-1. As this coefficient is the subject of considerable variation in the literature, here it is varied over a range of more than an order of magnitude. It is observed that the variation of γ has a huge impact on the parameters of the obtained current waveform. The larger the value of γ, the higher the frequency and the DC current of the pulses and sharper the rising side of the pulse. These numerical findings are not surprising in the sense that the higher the rate of the injection of the secondary electrons from the needle will lead to more intense avalanche ionization near the tip. Making γ smaller with the goal of getting closer to the experimental frequency and the DC current perturbs the form of the pulse drastically. It should be noted that the rise times of the pulses in the studied numerical models were not a function of the voltage level,

85

needle-plane distance, or the radius of the tip of the needle, and were only a function of the coefficient of the secondary emission of the electrons. The discrepancies between the results of the numerical models and the experiments could be caused by the idealizing assumptions of the numerical model. There are a number of reasons for this. Firstly, the model only considers three species in the reactions whereas many more exist in coronas in ambient air. Also, it can be seen how sensitive the results are to variations in the values selected for the coefficients and there are considerable discrepancies between these values as found in the literature. Also in comparing these results with the experiments, although the experimental error may be reasonable it must be remembered that the instrumentation and the experimental set up introduce various stray capacitances, sources of noise and other parameters that are not included in the numerical model.

Table 6-1: Comparison of the results of the numerical simulations based on the model suggested in [1], assuming γ=0.0005, γ=0.001, and γ=0.01, with the experimental data (applied needle voltage of -7 kV, needle-plane distance of 2 cm, and radius of the tip of 36 μm)

	Frequency (kHz)	DC current (μA)	Rise time (ns)	Fall time (ns)	Pulse width (ns)
Numerical model, γ=0.0005	288	6.6	207	1020	120
Numerical model, γ=0.001	460	9.6	139	690	105
Numerical model, γ=0.01	1266	36	61	520	101
Experiment	**101**	**7.9**	**49.2**	**444.8**	**219.8**

6.3   Summary

The results of an experimental study of the characteristics of Trichel pulses: the frequency of the pulses, DC current, rise time, fall time, and the pulse width have been reported in this Chapter. The needle-plane distance was varied in the range of 6 mm to 3 cm. It was observed that the rate of growth of frequency and the DC current in shorter air gaps was greater compared to larger air gaps. The variations of the frequency and the DC current were studied with the voltage ranging from the corona onset (which was -4 kV to -6 kV) to -10 kV for four needles with the radii of curvatures ranging from 19 μm to 55 μm. It was observed, both experimentally and numerically, that the temporal characteristics of Trichel pulses are not a function of needle voltage, needle-plane distance, or radius of the

tip of the needle at least within the range of needle radii tested. The fall time, rise time, and pulse width were measured to be 49 ns, 445 ns, and 220 ns, respectively. Comparison of the experimental results with the numerical models showed that although the model with $\gamma=0.0005$ gives the closest results for the frequency and the DC current compared to the models with greater values of γ, but the temporal characteristics of the pulses were drastically perturbed as a result of reducing γ from 0.01 to 0.0005. While the model with $\gamma=0.01$ gives acceptable agreement for the rise time and the fall time of the pulse, it leads to much greater numbers for the frequency and the DC current compared to the experimental results.

Chapter 7

7 « Incorporating the electron energy equation in the corona discharge model »

In this chapter, a report of the unsuccessful attempts for including the electron energy equation in the corona discharge numerical model is presented. First, an introduction about the electron energy equation will be given and then the conducted attempts for including this equation in the numerical model will be presented.

7.1   Electron energy equation

In plasma kinetic theory, the position of a particle (in this case, electron) is described in a 6-dimensional phase space: three position dimensions $\vec{r} = (x, y, z)$ and three velocity dimensions $\vec{v} = (v_x, v_y, v_z)$; an electron's phase space position is described by $(\vec{r}, \vec{v}) = (x, y, z, v_x, v_y, v_z)$ and the volume of a small element of phase space is $d^3\vec{r}\,d^3\vec{v}$.

In general, according to the plasma kinetic theory, electron transport is described by the Boltzmann equation,

$$\frac{\partial f}{\partial t} + \vec{v} \cdot \nabla f - \frac{e}{m_e}\vec{E} \cdot \nabla_v f = C[f] \qquad\qquad (7\text{-}1)$$

In this equation, $f(\vec{r}, \vec{v}, t)$ is the distribution of the electrons at the velocity space $\vec{v}$ and the position space $\vec{r}$ at the time t. Also, e, m_e, and $\vec{E}$ represent the electron charge, electron mass, and electric field, respectively. Moreover, ∇f and $\nabla_v f$ are the gradients of the electron distribution in the position space and the velocity space:

$$\nabla f = \frac{\partial f}{\partial x}\hat{x} + \frac{\partial f}{\partial y}\hat{y} + \frac{\partial f}{\partial z}\hat{z} \qquad (7\text{-}2)$$

$$\nabla_v f = \frac{\partial f}{\partial v_x}\hat{v}_x + \frac{\partial f}{\partial v_y}\hat{v}_y + \frac{\partial f}{\partial v_z}\hat{v}_z \qquad (7\text{-}3)$$

where $\hat{x}$, $\hat{y}$, $\hat{z}$, $\hat{v}_x$, $\hat{v}_y$, and $\hat{v}_z$ represent the coordinate unit vectors. Right hand side of the Eq. 7-1 is the collision term which includes rate of change in f du to the elastic and inelastic collisions.

To be able to solve the Boltzmann equation, drastic simplifications need to be made. The problem is limited to the cases where the electric field and the collision probabilities are all spatially uniform, at least on the scale of the collisional mean free path. The electron distribution f is then symmetric in velocity space around the electric field direction. In the position space, f may vary only along the direction of the electric field. Using spherical coordinates in velocity space, the Boltzmann equation is re-written as [89, 90]:

$$\frac{\partial f}{\partial t} + v\cos\theta \frac{\partial f}{\partial z} - \frac{e}{m_e}|\vec{E}|\left(\cos\theta \frac{\partial f}{\partial v} + \frac{\sin^2\theta}{v}\frac{\partial f}{\partial\cos\theta}\right) = C[f] \qquad (7\text{-}4)$$

where, v is the magnitude of the velocity, θ is the angle between the velocity and the field direction, and z is the position along this direction. A common approach to solve this equation is to expand f in terms of the Legendre polynomials of $\cos\theta$ (spherical harmonics expansion) and then construct a set of equations for the expansion coefficients. For the purpose of the current model, expanding the polynomial up to two terms gives the required accuracy. This method is also called two-term approximation of the Boltzmann equation. The f is expanded as:

$$f(v,\cos\theta,z,t) = f_0(v,z,t) + f_1(v,z,t)\cos\theta \qquad (7\text{-}5)\ .$$

Substituting Eq. (7-5) in Eq. (7-4), multiplying by respective Legendre polynomials (1 and $\cos\theta$), and integrating over $\cos\theta$, gives the equations required for finding f_0 and f_1:

$$\frac{\partial f_0}{\partial t} + \frac{\gamma}{3}\varepsilon^{1/2}\frac{\partial f_0}{\partial z} - \frac{\gamma}{3}\varepsilon^{-1/2}\frac{\partial}{\partial\varepsilon}\left(\varepsilon|\vec{E}|f_1\right) = C_0 \qquad (7\text{-}6)$$

$$\frac{\partial f_1}{\partial t} + \gamma\varepsilon^{1/2}\frac{\partial f_0}{\partial z} - E\gamma\varepsilon^{1/2}\frac{\partial f_0}{\partial\varepsilon} = C_1 \qquad (7\text{-}7)$$

where, $\gamma = (2e/m)^{1/2}$ is a constant and $\varepsilon = (v/\gamma)^2$ is the electron energy in eV. Another approximation which is used in the literature is to separate the energy-dependence of f from its dependence on the time and the space. This assumptions, after generalizing the z to the three space dimensions is written as:

$$f_{0,1}(\varepsilon, z, t) = \frac{1}{2\pi\gamma^3} F_{0,1}(\varepsilon) n_e(z, t) \qquad (7\text{-}8)$$

Multiplying the Eqs. 7-6 and 7-7 by $\varepsilon^{1/2}$, integrating over all energies, and generalizing the z to the three space dimensions leads to the electron continuity equation:

$$\frac{\partial n_e}{\partial t} + \nabla \cdot \Gamma_e = S_e \qquad (7\text{-}9)$$

where, S_e is the net electron source term and Γ_e is the electron flux defined as:

$$\Gamma_e = -\mu_e E n_e - \nabla(D_e n_e) \qquad (7\text{-}10)$$

where, the electron mobility and the electron diffusion coefficients are given by :

$$\mu_e N = -\frac{\gamma}{3} \int_0^\infty \frac{\varepsilon}{\tilde{\sigma}_m} \frac{\partial F_0}{\partial \varepsilon} d\varepsilon \qquad (7\text{-}11)$$

$$D_e N = -\frac{\gamma}{3} \int_0^\infty \frac{\varepsilon}{\tilde{\sigma}_m} F_0 d\varepsilon \qquad (7\text{-}12)$$

Similarly, multiplying the Eqs. 7-6 and 7-7 by $\varepsilon^{3/2}$, integrating over all energies, and generalizing the z to the three space dimensions leads to the electron energy equation:

$$\frac{\partial n_\varepsilon}{\partial t} + \nabla \cdot \Gamma_\varepsilon + \vec{E} \cdot \Gamma_e = S_\varepsilon \qquad (7\text{-}13)$$

where, S_ε is the total energy transfer (usually loss) due to the collisions, n_ε is the electron energy density and Γ_ε is the electron energy flux defined as:

$$n_\varepsilon \equiv n_e \bar{\varepsilon} = n_e \int_0^\infty \varepsilon^{3/2} F_0 d\varepsilon \qquad (7\text{-}14)$$

$$\Gamma_\varepsilon = -\mu_\varepsilon E n_\varepsilon - \nabla(D_\varepsilon n_\varepsilon) \qquad (7\text{-}15)$$

where, $\bar{\varepsilon}$ is the mean electron energy. Also, the energy mobility coefficient μ_ε and the energy diffusion coefficient D_ε are defined as:

$$\mu_\varepsilon N = -\frac{\gamma}{3\bar{\varepsilon}} \int_0^\infty \frac{\varepsilon^2}{\tilde{\sigma}_m} \frac{\partial F_0}{\partial \varepsilon} d\varepsilon \qquad (7\text{-}16)$$

$$D_\varepsilon N = -\frac{\gamma}{3\bar{\varepsilon}} \int_0^\infty \frac{\varepsilon^2}{\tilde{\sigma}_m} F_0 d\varepsilon \qquad (7\text{-}17)$$

The parameter $\tilde{\sigma}_m$ in the Eqs. 7-11, 7-12, 7-16, and 7-17 is a parameter which is proportional to the total momentum-transfer cross section of all the elastic reactions involving electrons. This parameter could be calculated from the table of the cross sections of the reactions involved in the discharge.

Rate coefficients of the reactions could also be calculated from the solution of the Boltzmann equation [91]:

$$k_k = \gamma \int_0^\infty \varepsilon \sigma_k(\varepsilon) f(\varepsilon) d\varepsilon \qquad (7\text{-}18)$$

where, $\sigma_k(\varepsilon)$ and k_k are the cross section and the rate coefficient of the kth reaction. It should be noted here that the cross section table of any chemical reaction is the fundamental reaction information which could be obtained by experiments. In fact, the cross section data for most of the chemical reactions present in the atmospheric pressure discharge of common gases such as oxygen is published in the literature.

In summary, for including the electron energy equation in the corona discharge model, following steps should be followed:

- The set of the reactions involved in the model should be determined. The cross section data of those reactions as a function of electron energy should be prepared.
- The cross section data should be entered as the input for the "Boltzmann equation, two-term approximation" module in the COMSOL Multiphysics software. Then the electron transport coefficients: electron mobility, electron diffusion, electron energy mobility, and electron energy diffusion using the Eqs. 7-11, 7-12, 7-16, and 7-17 are calculated. Moreover, the rate coefficients of the reactions using the Eq. 7-18 will be calculated, too.

- The electron transport coefficients and the reaction rate coefficients obtained in the previous step will be used to solve the pair of continuity equations (Eqs. 7-9 and 7-13) for the electron density n_e and the electron energy density n_ε.

7.2 Different modules in COMSOL Multiphysics and their restrictions

The numerical model which was attempted solve consists of 5 equations:

$$\frac{\partial n_e}{\partial t} + \nabla \cdot \left(-\mu_e \vec{E} n_e - D_e \nabla n_e\right) = S_e \qquad (\,7\text{-}19\,)$$

$$\frac{\partial n_\varepsilon}{\partial t} + \nabla \cdot \left(-\mu_\varepsilon E n_\varepsilon - \nabla(D_\varepsilon n_\varepsilon)\right) + \vec{E} \cdot \left(-\mu_e \vec{E} n_e - D_e \nabla n_e\right) = S_\varepsilon \qquad (\,7\text{-}20\,)$$

$$\frac{\partial n_p}{\partial t} + \nabla \cdot \left(\mu_p \vec{E} n_p - D_p \nabla n_p\right) = S_p \qquad (\,7\text{-}21\,)$$

$$\frac{\partial n_n}{\partial t} + \nabla \cdot \left(-\mu_n \vec{E} n_n - D_n \nabla n_n\right) = S_n \qquad (\,7\text{-}22\,)$$

$$\nabla^2 V = \frac{-e(n_p - n_e - n_n)}{\varepsilon_0} \qquad (\,7\text{-}23\,)$$

Compared to the set of the equations presented in Chapter 3, the Eq. 7-20 for finding the distribution of the electron energy density is added here. It was mentioned in Chapter 3 that the "Transport of the diluted species" module was used for solving the three continuity equations of the three charged species (electrons, positive ions, and negative ions). The main advantage of this module in COMSOL is the various stabilization techniques available for the user: streamline diffusion, crosswind diffusion, and isotropic diffusion. It was explained in Chapter 3 that solving the continuity equations of the charged species in the corona discharge regime using the Finite Element Method definitely requires one of the above-mentioned stabilization techniques. It was also explained that the streamline diffusion was the best method which does not perturb the original problem.

The "Plasma module" in COMSOL includes the electron energy equation along with the electron continuity equation. Unfortunately, the only stabilization technique available in this module is the "source stabilization" which adds an extra term to the right-hand side of the Eq. 7-19:

$$S_{e,add} = N_A \exp(-\zeta \ln n_e) \qquad (\text{ 7-24 })$$

where, $N_A = 6 \times 10^{23}$ (m^{-3}s^{-1}) is a constant number and ζ is the user-defined tuning parameter. The suggested default value for ζ is 1. When the electron density is very low, this acts as a source term which prevents the electron density from approaching zero. As the electron density increases this term becomes exponentially smaller, eventually becoming negligible for high electron densities. Similar term is added to the right hand side of the Eq. 7-20 for avoiding the electron energy density approaching zero:

$$S_{\varepsilon,add} = N_A \exp(-\zeta \ln n_\varepsilon) \qquad (\text{ 7-25 })$$

Unfortunately, we weren't able to solve Eqs. 7-19 to 7-23 using the "plasma module". It seems that the stabilization technique suggested by COMSOL is not capable of solving drift-diffusion equations under the corona discharge regime. As mentioned in Chapter 3, it is an accepted fact in the literature that the Finite Element Method requires artificial diffusion for solving the continuity equation. It should be noted here that the model library of COMSOL has some examples of using plasma module for numerous electric discharges, but all of them are in the regimes with much weaker electric fields.

We also built several models attempting to solve the Eqs. 7-19 to 7-23 using the transport of diluted species modules. Unfortunately, these models didn't lead to a convergent solution either. For some reasons which are not completely clear, it seems that the streamline diffusion stabilization method is not capable of handling the Eq. 7-20.

It should be also noted here that in all the models with different modules, numerous possible solutions by manipulating the parameters of the time-dependent solver and the mesh configuration were tested, too. Unfortunately, none of them led to a convergent solution.

Chapter 8

8 « Summary of the thesis and recommendations for the future studies »

The first part of this Chapter is devoted to the summary of the results of the numerical models and the conducted experiments reported in this thesis. In the second part of the chapter, some recommendations for the future studies in this field are suggested.

8.1 Summary of the thesis

Numerical and experimental analysis of the negative corona discharge in the needle-plane geometry and atmospheric air was presented in this thesis. Positive corona discharge was also studied in Chapter 4 as part of the investigation of the impact of the photoionization phenomenon on the positive and the negative corona discharge.

The following statements could be given as summary of the important findings of this thesis:

- During the stage of the electric field suppression, which was the second stage of the formation of the Trichel pulse, the time sequence of the reduction of the peak values of the important quantities were: electron density, positive ion density, electric field magnitude, current, and negative ion density. It was also noticed that in this stage the width of the ionization region reduces up to 30 µm. It was also found that the location of the peak densities of the electrons and the positive ions are not on the axis of symmetry but situated approximately 20 µm away from the axis.

- It was shown that in the Trichel pulse regime, several clouds of negative ions simultaneously exist in the air gap and the inter-pulse time is shorter than the time it takes for a cloud of negative ions to cross the gap. This means that the preparation of the gap for the next pulse begins as soon as the cloud of negative ions move far enough from the tip which is much sooner than it reaches the ground plane.

- The numerical model predicted that the transition from the Trichel pulse regime to the glow discharge regime for the needle-plane configuration of a 6 mm spacing and 35µm tip with atmospheric pressure air concludes at -12kV, as the current waveform becomes flat and a plasma channel is formed from the cathode to the anode. The simulations showed that the augmentation of the electric field in the area far from the needle tip in the glow discharge regime starts from the ground plane which is associated with a clearly visible blue film on the ground plane in the experiments.

- A numerical model for the positive corona discharge including three charged species (electrons, positive ions, and negative ions) and the photoionization phenomenon was suggested in this thesis. Photoionization phenomenon was incorporated using the three-term exponential approximation.

- The study of the impact of the photoionization phenomenon on negative corona discharge revealed a 5% increase in both the frequency and the DC current of the discharge. The insignificance of this impact was justified by calculating the ratio IIS/IPS (Integral of the Impact Ionization Source term divided by the Integral of the Photoionization Source term) at different stages of the formation of Trichel pulse along with studying the spatial distribution of the photoionization and impact ionization source terms. It was concluded, since the number of electrons produced by the impact ionization is on average 100 times larger than those of photoionization and the electrons produced by both sources travel approximately the same distance (undergo the same conditions of drift velocity) in the air gap, the incorporation of photoionization in the negative discharge model doesn't affect the discharge current significantly.

- The sensitivity study of the model coefficients of negative corona discharge in needle-plane configuration revealed the fact that the ionization coefficient has a larger impact on both the frequency and the DC current of the discharge compared to the impact of the attachment coefficient. It was also found that the existence of the reactions: recombination of the electrons and the positive ions and

95

recombination of the positive and the negative ions do not impact the characteristics of the Trichel pulses.

- The detachment reaction, present in the set of the coefficients used by Soloviev et al. [84], causes the pulsation mode of the discharge to disappear. It was found that the frequencies obtained using these coefficients were much higher than the expected values.

- Comparison of the results of the experiments with the findings of Lama and Gallo [37] led to a better agreement for the DC current as compared with the frequency of the pulses. Moreover, the numerical model predicted higher frequencies and DC currents compared to the experiments. The comparison showed that although the numerical model with $\gamma=0.0005$ gives the closest results for the frequency and the DC current compared to the models with greater values of γ, but the temporal characteristics of the pulses were drastically perturbed as a result of reducing γ from 0.01 to 0.0005.

- The results from all the experiments led to the average of 49 ns, 445 ns, and 220 ns for the rise time (10% to 90% of the peak), fall time (90% to 10% of the peak), and the pulse width (50% to 50% of the peak), respectively, with a standard deviation of less than 5%. Investigating these temporal characteristics led to the conclusion that these numbers don't change significantly by varying the voltage applied on the needle up to -10 kV, needle-plane distance from 6 mm to 3 cm or the radius of the tip of the needle from 19 µm to 55 µm.

8.2   Recommendations for the future studies

The following recommendations are suggested for the future studies:

- The studied numerical models in this thesis mostly have included 4 main reactions and three charged species in the atmospheric air. It would be interesting to include the excited species and the reactions including them in the model.

- The numerical model of the transition of the negative corona discharge from the Trichel pulse regime to the glow discharge regime presented in Chapter 3 did not include some features of the plasma channel formed between the cathode and the

anode. The excessive heat produced in the channel is the main reason for the instabilities noticed in the experiments. Including this instability in the model and applying the suggested methods for stabilizing the glow discharge such as air flow or crater-shaped ground plane right under the needle, might give researchers some new insights about the nature of the negative glow discharge.

- The studies reported in this thesis could be conducted for other gasses such as oxygen.

As explained in Chapter 7, including the electron energy equation in the corona discharge model comes with many challenges. One might consider combining the tools provided in COMSOL with other algorithms for overcoming the drawbacks of this software. It was evident that the stabilization techniques provided in COMSOL were able to solve the continuity equations for the charged species. If one could come up with an algorithm for solving the electron energy equation in conjunction with the solutions provided by COMSOL for the rest of the equations, studying the distributions of the electron energy and electron density in the corona gap would be possible. "COMSOL with MATLAB" which is part of the COMSOL Multiphysics package provides flexible programming tools for implementing user-defined algorithms.

References

1. Dordizadeh P, Adamiak K, Castle G S P 2015 Numerical investigation of the formation of Trichel pulses in a needle-plane geometry *J. Phys. D: Appl. Phys* **48**(41) 415203

2. Xiao G, Wang X, Zhang J, Ni M 2014 Current analysis of DC negative corona discharge in a wire-cylinder configuration at high ambient temperatures *J. Electrost.* **72**(2) 107-119

3. Khaddour B, Atten P, Coulomb J 2007 Numerical solution and experimental test for corona discharge between blade and plate *IEEE Trans. Mag.* **43**(4) 1193-1196

4. Dumitran L M, Dascalescu L, Notingher P V, Atten P 2007 Modelling of corona discharge in cylinder-wire-plate electrode configuration *J. Electrost.* **65**(12) 758-763

5. Reguig A, Bendaoud A, Dordizadeh P, Dascalescu L 2016 Experimental and Numerical Study of Corona Discharge Generated by a Wire-Type Dual Electrode Located Between Parallel Grounded Strips *Proc. Electrost. Joint Conf.*

6. Chang J S, Lawless P A, Yamamoto T 1991 Corona discharge processes *IEEE Trans. Plasma Sci.* **19**(6) 1152-1166

7. Trichel G W 1938 The mechanism of the negative point to plane corona near onset *Phys. Rev.* **54**(12) 1078

8. Akishev Y S, Grushin M E, Kochetov I V, Karal'nik V B, Napartovich A P 2005 Negative corona, glow and spark discharges in ambient air and transitions between them *Plasma Sources Sci. Tech.* **14**(2) S18.

9. Chen J, Davidson J H 2003 Model of the negative dc corona plasma: comparison to the positive dc corona plasma *Plasma Chem. and Plasma Proces.* **23**(1) 83-102

10. Sattari P 2011 FEM-FCT Based dynamic simulation of Trichel pulse corona discharge in point-plane configuration *PhD thesis* The University of Western Ontario, London, Ontario

11. Castle G S P 2001 Industrial applications of electrostatics: the past, present and future *J. Electrost.* **51** 1-7

12. Adamiak K 1994 Simulation of corona in wire-duct electrostatic precipitator by means of the boundary element method *IEEE Trans. Ind. Appl.* **30**(2) 381-386

13. Alotto P, Codecasa L 2016 Corona Discharge Simulation of Multiconductor Electrostatic Precipitators *IEEE Trans. Mag.* **52**(3) 1-4

14. Chen J, Davidson J H 2002 Ozone production in the positive DC corona discharge: Model and comparison to experiments *Plasma Chem. and Plasma Process.* **22**(4) 495-522

15. Skalný J D, Orszagh J, Matejčík Š, Mason N J 2008 Ozone generation in positive and negative corona discharge fed by humid oxygen and carbon dioxide *Physica Scripta* (T131) 014012

16. Dinelli G, Civitano L, Rea M 1990 Industrial experiments on pulse corona simultaneous removal of NO x and SO 2 from flue gas *IEEE Trans. Ind. Appl.* **26**(3) 535-541

17. Yan K, Hui H, Cui M, Miao J, Wu X, Bao C, Li R 1998 Corona induced non-thermal plasmas: fundamental study and industrial applications *J. Electrost.* **44**(1) 17-39

18. Mokhtari Z, Hole S, Lewiner J 2013 Smoke triggered corona discharge sensor. *J. Electrost.* **71**(4) 769-772

19. Deng F, Ye L, Song K 2014 Respiratory Monitoring by a Field Ionization Sensor Based on Trichel Pulses *Sensors* **14**(6) 10381-10394

20. Sladek R E J, Stoffels E, Walraven R, Tielbeek P J A, Koolhoven R A 2004 Plasma treatment of dental cavities: a feasibility study *IEEE Trans. Plasma Sci.* **32**(4) 1540-1543

21. Kovalova Z, Zahoran M, Zahoranova A, Machala Z 2014 Streptococci biofilm decontamination on teeth by low-temperature air plasma of dc corona discharges *J. Phys. D: Appl. Phys.* **47**(22) 224014

22. Jaworek A, Sobczyk A, Czech T, Krupa A 2014 Corona discharge in electrospraying *J. Electrost.* **72**(2) 166-178

23. Osman H, Castle G S P, Adamiak K 2015 Numerical study of particle deposition in electrostatic painting near a protrusion or indentation on a planar surface J. Electrost. **77** 58-68

24. Thyen R, Weber A, Klages C P 1997 Plasma-enhanced chemical-vapour-deposition of thin films by corona discharge at atmospheric pressure *Surface and Coatings Tech.* **97**(1) 426-434

25. Moreau E 2007 Airflow control by non-thermal plasma actuators *J. Phys. D: Appl. Phys.* **40**(3) 605

26. Wang H, Li J, Quan X 2006 Decoloration of azo dye by a multi-needle-to-plate high-voltage pulsed corona discharge system in water *J. Electrost.* **64**(6) 416-421

27. Malik M A, Ghaffar A, Malik S A 2001Water purification by electrical discharges *Plasma Sources Sci. Tech.* **10**(1) 82

28. Loeb L B, Kip A F, Hudson G G, Bennet W H 1941 Pulses in negative point-to-plane corona. *Phys. Rev.* **60**(10) 714

29. Černák M, Hosokawa T 1988 Similarities between the initial phase of a transient nonuniform glow discharge in nitrogen and the negative corona Trichel pulse formation in an electronegative gas *Appl. Phys. Letters* **52**(3) 185-187

30. Černák M, Hosokawa T 1989 The first Trichel pulse of negative corona discharge in N2 with a small admixture of SF6 *Czech. J. Phys. B* **39**(9) 1032-1036

31. Weissler G L 1943 Positive and negative point-to-plane corona in pure and impure hydrogen, nitrogen, and argon *Phys. Rev.* **63**(3-4) 96

32. Akishev Y S, Grushin M E, Karal'nik V B, Trushkin N I 2001 Pulsed mode of a negative corona in nitrogen: I. Experiment *Plasma Phys. Reports* **27**(6) 520-531

33. Akishev Y S, Grushin M E, Karal'nik V B, Trushkin N I 2001 Pulsed mode of a negative corona in nitrogen: II. Numerical calculations *Plasma Phys. Reports* **27**(6) 532-541

34. Loeb L B 1965 Electrical coronas *University of California Press Berkeley*

35. Gardiner P, Craggs J 1977 Negative ions in Trichel corona in air *J. Phys. D: Appl. Phys.* **10**(7) 1003

36. Bandel H W 1951 Point-to-plane corona in dry air *Physical Review* **84**(1) 92

37. Lama W L, Gallo C F 1974 Systematic study of the electrical characteristics of the "Trichel" current pulses from negative needle-to-plane coronas *J. Appl. Phys.* **45**(1) 103-113

38. Van Brunt R J, Leep D 1981 Characterization of point-plane corona pulses in SF6 *J. Appl. Phys.* **52**(11) 6588-6600.

39. Cross J, Haddad G 1986 Negative point-plane corona in oxygen *J Phys. D: Appl. Phys.* **19**(6) 1007

40. Morrow R 1985 Theory of stepped pulses in negative corona discharges *Physical Review A* **32**(6) 3821

41. He S J, Ha J, Han Y H, Liu Z Q, Guo S Q 2013 Trichel pulses in a negative corona discharge in air at low pressure *J. Phys.: Conf. Series* **418** 012091

42.   He S, Jing H 2014 Spatio-temporal characteristics of Trichel pulse at low pressure *Phys. Plasmas* **21**(1) 012112

43.   Durán-Olivencia F J, Pontiga F and Castellanos A 2014 Multi-species simulation of Trichel pulses in oxygen *J. Phys. D: Appl. Phys.* **47**(41) 415203

44.   Nygaard K J 1966 Frequency of corona discharge Trichel pulses in air flows *J. Appl. Phys.* **37**(7) 2850-2852

45.   Deng F, Ye L, Song K 2013 Numerical studies of Trichel pulses in airflows *J. Phys. D: Appl. Phys.* **46**(42) 425202

46.   Deng F, Ye L, Song K, Huang T 2014 Effect of humidity on negative corona Trichel pulses *Japanese J. Appl. Phys.* **53**(8) 080301

47.   Ogasawara M 1966 Analysis of formation stage of corona discharge *J. Phys. Soc. of Japan* **21**(11) 2360-2372

48.   Morrow R 1985 Theory of negative corona in oxygen *Phys. Rev. A* **32**(3) 1799

49.   Morrow R 1997*The theory of positive glow corona J. Phys. D: Appl. Phys.* **30**(22) 3099

50.   Napartovich A P, Akishev Y S, Deryugin A A, Kochetov I V, Pan'kin M V, Trushkin N I 1997 A numerical simulation of Trichel-pulse formation in a negative corona *J. Phys. D: Appl. Phys.* **30**(19) 2726

51.   Akishev Y S, Kochetov I V, Loboiko A I, Napartovich A P 2002 Numerical simulations of Trichel pulses in a negative corona in air *Plasma Phys. Reports* **28**(12) 1049-1059

52.   Zhang J, Adamiak K, Castle G S P 2007 Numerical modeling of negative-corona discharge in oxygen under different pressures *J. Electrost.* **65**(3) 174-181

53. Sattari P, Castle G S P, Adamiak K 2010 FEM–FCT-Based Dynamic Simulation of Corona Discharge in Point–Plane Configuration *IEEE Trans. Ind. Appl.* **46**(5) 1699-1706

54. Sattari P, Castle G S P, Adamiak K 2011 Numerical simulation of Trichel pulses in a negative corona discharge in air *IEEE Trans. Ind. Appl.* **47**(4) 1935-1943

55. Sattari P, Gallo C F, Castle GSP, Adamiak K 2011 Trichel pulse characteristics— negative corona discharge in air *J. Phys. D: Appl. Phys.* **44**(15) 155502

56. Tran T N, Golosnoy I O, Lewin P L, Georghiou G E 2011 Numerical modelling of negative discharges in air with experimental validation *J. Phys. D: Appl. Phys.* **44**(1) 015203

57. Adamiak K, Atten P 2004 Simulation of corona discharge in point–plane configuration *J. Electrost.* **61**(2) 85-98

58. Kang W S, Park J M, Kim Y, Hong S H 2003 Numerical study on influences of barrier arrangements on dielectric barrier discharge characteristics *IEEE Trans. Plasma Sci.* **31**(4) 504-510

59. Soria-Hoyo C, Pontiga F, Castellanos A 2007 Particle-in-cell simulation of Trichel pulses in pure oxygen *J. Phys. D: Appl. Phys.* **40**(15) 4552

60. Tran T N, Golosnoy I O, Lewin P L, Georghiou G E 2009 Two dimensional studies of Trichel pulses in air using the finite element method *IEEE Conf. on Electrical Insulation and Dielectric Phenomena (Virginia Beach, VA)*

61. Penney G, Hummert G 1970 Photoionization measurements in air, oxygen, and nitrogen *J. Appl. Phys.* **41**(2) 572-57

62. Naidis G 2006 On photoionization produced by discharges in air *Plasma Sources Sci. Tech.* **15**(2) 253

63.	Luque A, Ebert U, MontijnC, Hundsdorfer W 2007 Photoionization in negative streamers: Fast computations and two propagation modes *Appl. Phys. Letters* **90**(8) 081501

64.	Bourdon A, Pasko V P, Liu N Y, Célestin S, Ségur P, Marode E 2007 Efficient models for photoionization produced by non-thermal gas discharges in air based on radiative transfer and the Helmholtz equations *Plasma Sources Sci. Tech.* **16**(3) 656

65.	Pancheshnyi S 2014 Photoionization produced by low-current discharges in O2, air, N2 and CO2 *Plasma Sources Sci. Tech.* **24**(1) 015023

66.	Zheleznyak M B, Kh M A, Sizykh S V 1982 Photoionization of mixtures of nitrogen and oxygen by gas discharge radiation *Teplofiz. Vys. Temp.* **20** 423

67.	Ségur P, Bourdon A, Marode E, Bessières D, Paillol J H 2006 The use of an improved Eddington approximation to facilitate the calculation of photoionization in streamer discharges *Plasma Sources Sci. Tech.* **15**(4) 648

68.	Larsen E W, Thömmes G, Klar A, Seaıd M, Götz T 2002 Simplified P N approximations to the equations of radiative heat transfer and applications *J. Comp. Phys.* **183**(2) 652-675

69.	Papageorgiou L, Metaxas A C, Georghiou G E 2011 Three-dimensional numerical modelling of gas discharges at atmospheric pressure incorporating photoionization phenomena *J. Phys. D: Appl. Phys.* **44**(4), 045203

70.	Sattari P, Castle G S P, Adamiak K 2011 Numerical simulation of Trichel pulses in a negative corona discharge in air *IEEE Trans. Ind. Appl.* **47**(4) 1935-1943

71.	Codina, R 1998 Comparison of some finite element methods for solving the diffusion-convection-reaction equation *Comp. meth. app. Mech. Eng.* **156**(1) 185-210

72.   Codina R 1993 A discontinuity-capturing crosswind-dissipation for the finite element solution of the convection-diffusion equation *Comp. meth. app. Mech. Eng.* **110**(3) 325-342

73.   COMSOL Multiphysics 4.4 Reference Manual, November 2013 edition

74.   Jadidian J, et al. 2012 Effects of impulse voltage polarity, peak amplitude, and rise time on streamers initiated from a needle electrode in transformer oil *IEEE Trans. Plasma Sci.* **40**(3) 909-918

75.   Sato N 1980 Discharge current induced by the motion of charged particles *J. Phys. D: Appl. Phys.* **13**(1) L3

76.   Goldman M, Goldman A and Sigmond R The corona discharge, its properties and specific uses *Pure and Appl. Chem.* **57**(9) 1353-1362

77.   Goossens O, Callebaut T, Akishev Y S, Napartovich A P, Trushkin N I and Leys C 2002 The DC glow discharge at atmospheric pressure *IEEE Trans. Plasma Sci.* **30**(1) 176-177

78.   Kulikovsky A A 2000 The role of photoionization in positive streamer dynamics. *J. Phys. D: Appl. Phys.* **33**(12) 1514

79.   Pancheshnyi S 2005 Role of electronegative gas admixtures in streamer start, propagation and branching phenomena *Plasma Sources Sci. Tech.* **14**(4) 645

80.   Dordizadeh P, Adamiak K, Castle G S P 2015 Numerical investigation of the formation of Trichel pulses in a needle-plane geometry *J. Phys. D: Appl. Phys.* **48**(41) 13

81.   COMSOL Multiphysics 5.0 Reference Manual, November 2014 edition

82.   Georghiou G E, Papadakis A P, Morrow R, Metaxas A C 2005 Numerical modelling of atmospheric pressure gas discharges leading to plasma production *J. Phys. D: Appl. Phys.* **38**(20) R303

83.   Fridman A, Kennedy L A 2004 Plasma physics and engineering *CRC press*

84.   Soloviev V, Krivtsov V 2009 Surface barrier discharge modelling for aerodynamic applications *J. Phys. D: Appl. Phys.* **42**(12) 125208

85.   Li Z, Zhang B, He J 2013 Specific characteristics of negative corona currents generated in short point-plane gap *Phys. Plasmas (1994-present)* **20**(9) 093507

86.   Li Z, Zhang B, He J, Xu Y 2014 Influence of gap spacing on the characteristics of Trichel pulse generated in point-to-plane discharge gaps *Phys. Plasmas (1994-present)* **21**(1) 012113

87.   Zhang Y, Qin Y, Zhao G, Ouyang J 2016 Time-resolved analysis and optical diagnostics of Trichel corona in atmospheric air *J. Phys. D: Appl. Phys.* **49**(24) 245206

88.   Tran T N, Golosnoy I O, Lewin P L, Georghiou G E 2011 Numerical modelling of negative discharges in air with experimental validation *J. Phys. D: Appl. Phys.* 44(1) 015203

89.   Hagelaar G, Pitchford L 2005 Solving the Boltzmann equation to obtain electron transport coefficients and rate coefficients for fluid models *Plasma Sources Sci. Tech.* **14**(4) 722

90.   Bergas J 2014 Contributions on corona onset voltage calculation for EHV and UHV substation connectors

91.   COMSOL Multiphysics 5.2 Plasma Module Manual, 2015 edition

Curriculum Vitae

Name:	Peyman Dordizadeh

Post-secondary Education and Degrees:

Iran University of Science and Technology
Tehran, Tehran, Iran
2004-2008 B.Sc.

University of Tehran
Tehran, Tehran, Iran
2008-2011 M.Sc.

Western University
London, Ontario, Canada
2012-2016 Ph.D.

Honors and Awards:

Best B.Sc. Thesis Award, Iran Univ. of Sci. and Tech.
Tehran, Tehran, Iran
September 2008

Graduate research scholarship, Western Univ., London, Ontario
May 2012

Third place best presentation award, ESA conference
University of Notre Dame, Indiana
June 2014

Related Work Experience

Electrical design engineer
Shafab Engineering Co.
Tehran, Iran
2010- 2012

Teaching Assistant
Western University
2012- 2016

Research Assistant
Western University
2012- 2016

Published Papers:

- A Reguig, A Bendaoud, P Dordizadeh, and L Dascalescu "Experimental and Numerical Study of Corona Discharge Generated by a Wire-Type Dual Electrode Located Between Parallel Grounded Strips" Electrostatics Joint Conf., June 2016, Purdue University, IN

- P Dordizadeh, K Adamiak, and GSP Castle "Numerical investigation of the formation of Trichel pulses in a needle-plane geometry" Journal of Physics D: Applied Physics 48.41 (2015): 415203

- P Gharghabi, P Dordizadeh, and K Niayesh "Impact of metal thickness and field shaper on the time-varying processes during impulse electromagnetic forming in tubular geometries" Journal of the Korean Physical Society 59.61 (2011): 3560-3566

- P Dordizadeh, P Gharghabi, and K Niayesh "Dynamic analysis of a fast-acting circuit breaker (Thompson) drive mechanism" Journal of the Korean Physical Society 59 (2011): 3547

- P Dordizadeh, K Adamiak, and GSP Castle "Study of the impact of photoionization on negative and positive needle-plane corona discharge in atmospheric air" Plasma Sources Science and Technology

- P Dordizadeh, K Adamiak, and GSP Castle "Parametric study of the characteristics of Trichel pulses in the needle-plane negative corona discharge in atmospheric air" Journal of Electrostatics